CONSTRUCTION OF AN ULTRA LOW TEMPERATURE CRYOSTAT AND TRANSVERSE ACOUSTIC SPECTROSCOPY IN SUPERFLUID ^{3}HE IN COMPRESSED AEROGELS

By

PRADEEP BHUPATHI

A DISSERTATION PRESENTED TO THE GRADUATE SCHOOL
OF THE UNIVERSITY OF FLORIDA IN PARTIAL FULFILLMENT
OF THE REQUIREMENTS FOR THE DEGREE OF
DOCTOR OF PHILOSOPHY

UNIVERSITY OF FLORIDA

2009

© 2009 Pradeep Bhupathi

To Amma and Nanna

ACKNOWLEDGMENTS

I would like to thank my advisor and mentor Yoon Lee without whose guidance and encouragement this work would not have been possible. I am grateful to him for having an immense amount of patience and trust in me. I thank him for providing me the privilege to work on the cryostat from the very beginning. He is one of the best advisors that one can ask for. I thank undergraduate students Jose Cancino and Aaron Gray who have worked on the construction of the cryostat along with me during my first years. Jose taught me the basics of AutoCAD drawing and LabView programming. The LabView program for automating the melting curve thermometer was first written by him and later modified by me and Hyunchang Choi. Aaron designed the aluminum support structure for the cryostat. There are many number of people without whose help our experiments would not have been possible. Jian-Sheng Xia from the microkelvein laboratory let me use the coil winder and the annealing furnace whenever I wanted to. Greg Labbe and John Graham from cryogenic services were always ready to provide us with a continuous supply of liquid helium for our cool downs any time of the year! Marc Link, Ed Storch and Bill Malphurs from the physics machine shop made many parts that went into building the cryostat. They were the ones who brought my drawings from paper to reality in no time! It has been fun working with them. Larry Phelps and Pete Axson from the electronics shop helped us troubleshoot our electronic equipment. They built the low noise magnet power supply for the heat switch of our cryostat.

I would like to thank Jungseek Hwang for patiently answering all my stupid questions on the optical measurements on aerogels and teaching me how to use the spectrometer. I would also like to thank Prof. David Tanner and Prof. Sergei Obukhov and my committee members Prof. Mark Meisel, Prof. Amlan Biswas, Prof. Pradeep Kumar and Prof. Michael Scott for giving me feedback on different aspects of my thesis.

Numerous friends and colleagues made my life in Gainesville a lot easier and fun. I thank my roommates Aparna and Karthik, lab mates Jose, Aaron, Hyunchang, Byoung

Hee, Miguel for various discussions on physics and otherwise and friends Naveen, Vidya, Sung Hee, Dan Pajerowski the "dude", for his entertaining jokes on life, universe and everything. Finally, I would like to thank Suhasni for putting up with me on all aspects of life and feeding me some amazing food!

And most of all, I would like to thank my parents for their support throughout my life.

TABLE OF CONTENTS

page

ACKNOWLEDGMENTS . . . 4

LIST OF TABLES . . . 8

LIST OF FIGURES . . . 9

ABSTRACT . . . 12

CHAPTER

1 INTRODUCTION . . . 14

1.1 Normal Liquid . . . 15
1.2 Superfluid Phases of ^{3}He . . . 17

2 SUPERFLUID ^{3}He IN AEROGEL . . . 22

2.1 Ginzburg-Landau Theory . . . 23
2.1.1 Homogeneous Scattering Model (HSM) . . . 24
2.1.2 Slab Model . . . 25
2.1.3 Isotropic Inhomogeneous Scattering Model (IISM) . . . 25
2.1.4 Anisotropic HSM . . . 26
2.2 Effect of Anisotropic Scattering . . . 26
2.2.1 Compressed and Stretched Aerogels . . . 29

3 CONSTRUCTION OF AN ULTRA LOW TEMPERATURE CRYOSTAT . . . 34

3.1 Cryostat Support Structures . . . 34
3.1.1 The Top Plate . . . 34
3.2 The Pumping Systems . . . 35
3.2.1 The Still Line . . . 36
3.2.2 The Pot and Dewar Line . . . 37
3.3 Gas Handling Systems . . . 37
3.3.1 ^{3}He Gas Handling . . . 37
3.3.1.1 Gas Capillaries . . . 37
3.3.2 Oxford Intelligent Gas Handling (IGH) . . . 38
3.4 Electrical Systems . . . 39
3.4.1 Homemade Coaxes . . . 39
3.4.2 Twisted Pairs . . . 40
3.5 Dewar . . . 41
3.6 The Dilution Refrigerator . . . 42
3.7 Heat Switch . . . 43
3.8 The Nuclear Stage . . . 44
3.9 Heat Exchanger . . . 45
3.10 Demagnetization and Experimental Magnet . . . 46

3.11 Thermometry . . . 47
3.11.1 Melting Curve Thermometer . . . 47
3.12 Performance of the Nuclear Stage . . . 49

4 OPTICAL BIREFRINGENCE MEASUREMENTS IN AEROGEL . . . 76

4.1 Principle . . . 76
4.2 Experimental Method . . . 77
4.3 Results and Discussion . . . 79
4.3.1 Mechanical Properties . . . 79
4.3.2 Transmittance Measurements . . . 79
4.3.3 Effective Medium Models . . . 84
4.4 Summary . . . 86

5 TRANSVERSE ACOUSTIC MEASUREMENTS IN COMPRESSED AEROGELS 101

5.1 Experiments in Compressed Aerogels . . . 101
5.2 Experimental Technique . . . 103
5.3 Acoustic Cell . . . 104
5.4 Results . . . 106

6 CONCLUSION . . . 123

APPENDIX

A TRANSPORT MEASUREMENTS IN BILAYER MANGANITE FILMS . . . 125

A.1 Introduction . . . 125
A.2 Device Fabrication and Measurement Technique . . . 126
A.3 Results . . . 127
A.4 Summary . . . 128

B OPERATION OF THE CRYOSTAT . . . 132

B.1 Assembling . . . 132
B.2 Leak Detecting Procedure . . . 135
B.3 Cooling Down . . . 138
B.4 Warming Up . . . 142

REFERENCES . . . 145

BIOGRAPHICAL SKETCH . . . 150

LIST OF TABLES

Table page

3-1 Oxford coaxial cable assignments 60

3-2 Resistance values of resistors in the bath 60

3-3 Cinch connector assignments on cryostat 62

4-1 Parameters for aerogel samples. 89

B-1 Fischer pin connector assignment 144

LIST OF FIGURES

Figure page

1-1 Phase diagram of superfluid ^{3}He in zero magnetic field 20

1-2 $P - H - T$ phase diagram of superfluid ^{3}He 20

1-3 Energy gap in the Superfluid A and B phases 21

2-1 Simulated picture of aerogel structure by Tom Haard 30

2-2 Phase diagram of superfluid ^{3}He in aerogel 30

2-3 Superfluid transition in ^{3}He/aerogel relative o the bulk 31

2-4 Phase diagram of ^{3}He in aerogel showing A-like to B-like transition 32

2-5 Cartoon of compressed and stretched aerogel cylinders 32

2-6 Theoretical phase diagram of superfluid ^{3}He in anisotropic aerogels 33

3-1 Schematic drawing of the Cryostat 53

3-2 Overview of "Thule" cryostat structure 54

3-3 The top plate of the cryostat 55

3-4 Design of the double gimbal bellows 56

3-5 ^{3}He gas handling system 57

3-6 Kelvinox gas handling system 58

3-7 Dimensions of the vapor cooled dewar 59

3-8 Picture of the Kelvinox 400 dilution refrigerator 61

3-9 Heat leak to the dilution refrigerator 62

3-10 Inner vacuum can and radiation shield 63

3-11 Indium heat switch design 64

3-12 Magnetic field of the home-made solenoid 65

3-13 The copper nuclear demagnetization stage 66

3-14 Annealed copper on stainless steel structure 67

3-15 Heat exchanger design 68

3-16 Magnet dimensions relative to the dewar 69

3-17 Magnetic field profile of the superconducting magnet 70
3-18 Melting curve thermometer design 71
3-19 Capacitance bridge circuit diagram for the MCT 72
3-20 Precooling curves on different cooldowns 73
3-21 Plot of H/T vs. T during adiabatic demagnetization 73
3-22 Chart recorder traces of MCT during the very first demagnetization 74
3-23 Magnetic field dependance of the heat leak to the CDS 75
3-24 Nuclear heat capacity of the CDS 75
4-1 Measurement scheme for optical transmittance measurements 88
4-2 Surface images of aerogel 88
4-3 Length comparisons of aerogel samples 89
4-4 Reference spectrum for optical measurements 90
4-5 Transmittance vs. wavelength of aerogel sample 1 90
4-6 Transmittance vs. wavelength of aerogel sample 2 91
4-7 Transmittance vs. wavelength of aerogel sample 3 91
4-8 Analyzer angle dependent transmittance of aerogel samples 92
4-9 Transmittance of sample 1 for 0 to 15% compression at different analyzer angles 93
4-10 Transmittance of sample 2 for 0 to 15% compression at different analyzer angles 94
4-11 Transmittance of sample 3 for 0 to 15% compression at different analyzer angles 95
4-12 Transmittance vs. wavenumber of sample 1 at 15% compression 96
4-13 Transmittance spectrum of sample 1 in the UV-visible-NIR region 96
4-14 Transmittance in the cross polarized configuration for samples 1, 2 and 3 97
4-15 Birefringence dispersion in aerogel sample 3 for various strains 98
4-16 Strain dependance of birefringence for aerogel sample 3 98
4-17 Strain dependance of birefringence for aerogel samples at fixed wavelength . . . 99
4-18 Integrated transmission as a function of strain for aerogel samples 99
4-19 Calculated birefringence of aerogel sample 1 using Maxwell-Garnet Theory . . . 100

5-1 Picture of Macor experimental cell with aerogel 110
5-2 Picture of experimental cell 111
5-3 Schematic diagram of the CW spectrometer 112
5-4 Typical resonance spectrum from the transducer 113
5-5 Acoustic response on cooling in zero field at 32 bar 113
5-6 Acoustic response on warming in zero field and 32 bar pressure 114
5-7 Acoustic response on cooling in 0.933 kG and 32 bar pressure 114
5-8 Acoustic response on warming in 0.933 kG and 32 bar pressure 115
5-9 Acoustic response on cooling in 1.5 kG and 32 bar pressure 115
5-10 Acoustic response on warming in 1.5 kG and 32 bar pressure 116
5-11 Tracking of aerogel A-B transition at 1.5 kG field and 32 bar pressure 117
5-12 Tracking of aerogel A-B transition at 1.5 kG field and 32 bar pressure 118
5-13 Acoustic response from ^{3}He in 5% compressed aerogel on cooling, 32 bar and 2 kG 119
5-14 Acoustic response from ^{3}He in 5% compressed aerogel on warming, 32 bar and 2 kG 119
5-15 Quadratic suppression of the A-B transition in magnetic fields 120
5-16 Acoustic response from ^{3}He in 10% compressed aerogel on cooling and warming, 29 bar and 0 - 3 kG fields 121
5-17 Acoustic response from ^{3}He in 10% compressed aerogel on cooling and warming, 32 bar and 0 - 3 kG fields 122
A-1 Resistance (R) vs. temperature (T) for the bilayer manganite 129
A-2 Current dependance of R vs. T of manganite structure 129
A-3 Low temperature R vs. T upturn in bilayer manganite 130
A-4 Low temperature magneto-resistance in bilayer manganite 130
A-5 Low temperature R vs. T upturn in thin film of LPCMO manganite 131
B-1 Typical calibration curve of the MCT at 1K 144

Abstract of Dissertation Presented to the Graduate School
of the University of Florida in Partial Fulfillment of the
Requirements for the Degree of Doctor of Philosophy

CONSTRUCTION OF AN ULTRA LOW TEMPERATURE CRYOSTAT AND TRANSVERSE ACOUSTIC SPECTROSCOPY IN SUPERFLUID ^{3}HE IN COMPRESSED AEROGELS

By

Pradeep Bhupathi

May 2009

Chair: Yoonseok Lee
Major: Physics

An ultra low temperature cryostat is designed and implemented in this work to perform experiments at sub-millikelvin temperatures, specifically aimed at understanding the superfluid phases of ^{3}He in various scenarios. The cryostat is a combination of a dilution refrigerator (Oxford Kelvinox 400) with a base temperature of 5.2 mK and a 48 mole copper block as the adiabatic nuclear demagnetization stage with a lowest temperature of $\approx$ 200 μK. With the various techniques implemented for limiting the ambient heat leak to the cryostat, we were able to stay below 1 mK for longer than 5 weeks. The details of design, construction and performance of the cryostat are presented.

We measured high frequency shear acoustic impedance in superfluid ^{3}He in 98% porosity aerogel at pressures of 29 bar and 32 bar in magnetic fields upto 3 kG with the aerogel cylinder compressed along the symmetry axis to generate global anisotropy. With 5% compression, there is an indication of a supercooled A-like to B-like transition in aerogel in a wider temperature width than the A phase in the bulk, while at 10% axial compression, the A-like to B-like transition is absent on cooling down to $\approx$ 300 μK in zero magnetic field and in magnetic fields up to 3 kG. This behavior is in contrast to that in ^{3}He in uncompressed aerogels, in which the supercooled A-like to B-like transitions have been identified by various experimental techniques. Our result is consistent with theoretical predictions.

To characterize the anisotropy in compressed aerogels, optical birefringence is measured in 98% porosity silica aerogel samples subjected to various degrees of uniaxial compression up to 15% strain, with wavelengths between 200 to 800 nm. Uncompressed aerogels exhibit no or a minimal degree of birefringence, indicating the isotropic nature of the material over the length scale of the wavelength. Uniaxial compression of aerogel introduces global anisotropy, which produces birefringence in the material. We observed a quasi-linear strain dependence in $\Delta n = n_e - n_o$ in compressed aerogels, where $n_{e(o)}$ is the index of refraction for the extraordinary (ordinary) ray of light that has its polarization parallel to the compression axis. Incidentally, this effect has potential applications for aerogels as tunable waveplates operating in a broad spectral range.

CHAPTER 1
INTRODUCTION

^{3}He is one of the only two known elements (the other being its stable isotope ^{4}He) that remains liquid under its own vapor pressure even at absolute zero temperature. This remarkable feature is due to its large quantum mechanical zero point motion arising from its small atomic mass (^{3}He is the second lightest element known in Nature). Owing to its small mass and spherical symmetry it has the weakest van der Waals attractive interaction resulting in a lowest liquefaction temperature of 3.2 K. The odd number of nucleons in ^{3}He nucleus give a total spin 1/2 for ^{3}He atom and hence it is a composite fermion obeying Fermi-Dirac statistics. Below 1 K (Fermi temperature), it is no longer a classical liquid and its quantum nature is manifest. Figure 1-1 shows the pressure-temperature phase diagram of liquid ^{3}He. There are several unique features in the phase diagram. First of all, there is no triple point between gas, liquid and solid phase. It remains liquid as mentioned above and solidifies only for pressures above 34 bar. There is a minimum in the solid-liquid coexistence curve (melting curve) of ^{3}He occurring at 29.31 bar and 315.24 mK, and at the lowest temperatures it undergoes transitions into multiple superfluid phases. The minimum in the melting curve of ^{3}He is due to the fact that at low temperatures (<0.3 K), the entropy of the liquid falls below the entropy of the paramagnetic solid ($R \ln 2$), thereby causing a sign change according to the Clausius-Clapeyron equation. This special nature of the melting curve provides a unique mechanism for a cooling technique known as Pomeranchuk cooling. The strong temperature dependence of the melting curve also serves as a reliable temperature scale in the ultra-low temperature regime.

Liquid ^{3}He at low temperatures is also the cleanest system in Nature that does not possess any background crystal structure or impurities. Near millikelvin temperatures, it undergoes transitions into two different superfluids exhibiting unconventional pairing and exotic broken symmetries. They are arguably the most intriguing phases of matter that

have been extensively studied and thoroughly understood in their pure form [1, 2]. Being the cleanest system, superfluid ^{3}He is an ideal model system for studying the influence of disorder in a systematic manner. It also serves as a paradigm for understanding other classes of interacting fermion systems in condensed matter physics such as the high temperature superconductors and heavy fermion systems. Furthermore, superfluid ^{3}He has analogies in different branches of physics such as particle physics and cosmology [3]. In this chapter, we briefly describe the normal and superfluid properties of liquid ^{3}He.

1.1 Normal Liquid

The properties of normal liquid ^{3}He below 100 mK are well described by the Landau's theory of Fermi liquids [4]. For a brief introduction pertinent to liquid ^{3}He, see Leggett's review article [1]. Landau's theory is equivalent to the theory of a free Fermi gas but with two important differences. The first is the concept of a quasi-particle with an effective mass m^* that enters the single particle energy spectrum, $\epsilon(\mathbf{k}) = \hbar^2 k^2/2m^*$. The second important difference is the introduction of an effective interaction between quasi-particles. A quasi-particle can be visualized as a bare ^{3}He atom screened by a cloud of neighboring atoms and thereby having an effective mass greater than the bare mass, m, of the ^{3}He atom. Quasi-particles have definite momentum ($\mathbf{k}$) and spin (σ) and obey Fermi-Dirac statistics. A quasi-particle excited above the ground state will have a total energy equal to $\epsilon(\mathbf{k})$ plus a contribution arising from the deviation in the occupancy of energy states $\delta n(\mathbf{k}, \sigma)$ from its ground state value and can be written as:

$$\tilde{\epsilon}(\mathbf{k}, \sigma) = \epsilon(\mathbf{k}) + \sum_{k'} f(\mathbf{k}, \mathbf{k}')\delta n(\mathbf{k}') \tag{1–1}$$

where $f(\mathbf{k}, \mathbf{k}')$ is a molecular field type interaction function which can be decomposed into spin-symmetric and spin-antisymmetric parts f_l^s, f_l^a, respectively, where l denotes the angular momentum. Considering the invariance of the system under spatial rotations, the interaction energy functions depend only on the angle (θ) between the momenta, k and k' and can be expanded in terms of the Legendre polynomials as $F_l^s P_l \cos\theta$ and $F_l^a P_l \cos\theta$.

F_l^s and F_l^a are normalized to the density of states at the Fermi surface and hence are dimensionless parameters called as the Landau Fermi liquid parameters. The Landau parameters determine various thermodynamic properties of the Fermi liquid. For example, the ratio of the quasi-particle mass to the bare mass of ^{3}He given by,

$$\frac{m*}{m} = 1 + \frac{F_1^s}{3} \tag{1–2}$$

enters the specific heat at constant volume (C_v) and magnetic susceptibility χ,

$$C_v = \frac{m^* k_F}{3\hbar^2} k_B^2 T, \quad \chi = \frac{\chi_o}{1 + F_o^a} \tag{1–3}$$

where χ_o is the Pauli susceptibility of an ideal Fermi gas with mass m^*. Thus, the thermodynamic properties of a Fermi liquid: specific heat proportional to T and spin susceptibility independent of temperature are qualitatively same as for a non-interacting Fermi gas, only renormalized through the Fermi liquid parameters. The transport properties on the other hand require consideration of the collisions between the quasi-particles with a relaxation time $\tau \propto 1/T^2$. For instance, properties such as sound velocity, thermal conductivity, viscosity and spin diffusion are determined by solving the Boltzmann transport equation. One of the remarkable features of the Fermi liquid theory is its prediction of new types of collective modes in the sound propagation [5]. At high temperatures, hydrodynamic sound (or first sound) propagates by means of scattering processes in the liquid with the constraint $\omega\tau \ll 1$. At low temperatures, the condition $\omega\tau \ll 1$ is not satisfied and ordinary sound ceases to exist. However, in this collisionless limit ($\omega\tau \gg 1$), there exist propagation of zero sound modes that are essentially oscillations of the Fermi surface in response to the external perturbation. The restoring force for the propagating mode is provided by the molecular field generated by the quasi-particle excitations. There are two possible modes of sound that can exist, the longitudinal zero sound and transverse zero sound, both of which are experimentally

verified in the normal liquid [6, 7]. It turns out that these modes can appear even in the superfluid phase by coupling to the order parameter collective modes [8–10].

1.2 Superfluid Phases of ^{3}He

Due to the hard repulsive core in the interatomic potential, the ^{3}He atoms form Cooper-pairs in a state of non-zero relative angular momentum. It is well known that the superfluid phases of ^{3}He are the BCS condensates of *p-wave* ($l = 1$) spin-triplet ($S = 1$) Cooper pairs [1, 2]. This is in stark contrast to the Cooper pairing in conventional superconductors where pairs with opposite spins ($S = 0$) form a spin-singlet *s-wave* state. Unlike the electron Cooper-pairs in a conventional superconductor, which are structureless and spherically symmetric, quasiparticles of ^{3}He atoms form Cooper-pairs with internal degrees of freedom associated with the projections in orbital ($m_l = -1, 0, +1$) and spin space ($m_s = -1, 0, +1$). There are three distinct stable superfluid phases in bulk (pure) ^{3}He, namely the A and B phases and the A_1 phase in a non-zero magnetic field. The B phase corresponds to the theoretical Balian-Werthamer (BW) state [11] and is the most stable state at low pressures. It occupies most of the region in the pressure-temperature ($P - T$) phase diagram as shown in Figure 1-1. The wave function of this phase is a superposition of all three spin-triplet states:

$$|B\rangle = \Psi_{1,-1}(\mathbf{r})|\uparrow\uparrow\rangle + \Psi_{1,1}(\mathbf{r})|\downarrow\downarrow\rangle + \Psi_{1,0}(\mathbf{r})|\uparrow\downarrow + \downarrow\uparrow\rangle \tag{1–4}$$

where $\Psi_{l,m_s}(\mathbf{r})$ is the orbital wave function. It has an isotropic energy gap and resembles ordinary superconductors in many ways.

On the other hand, the A phase corresponds to the Anderson-Brinkman-Morel (ABM) state [12] and is a superposition with equal amplitudes for the oppositely polarized spin-triplet states. Hence it is also called the equal spin pairing (ESP) state:

$$|A\rangle = \frac{1}{\sqrt{2}}\Psi_{1,1}(\mathbf{r})(|\uparrow\uparrow\rangle + |\downarrow\downarrow\rangle) \tag{1–5}$$

In contrast to the B phase, the A phase has essentially the same magnetic susceptibility as that of the normal liquid indicating that the spin substate with $S_z = 0$ is absent in the A phase. In this phase, the energy gap is anisotropic. It depends on the direction in **k**-space on the Fermi sphere and is given by:

$$\Delta_{\hat{k}}(T) = \Delta_o(T)[1 - (\hat{k} \cdot \hat{l})^2]^{1/2} \tag{1–6}$$

A schematic of the energy gap for the A and B phases is shown in Figure 1-3. The A phase energy gap has two nodes on the Fermi sphere along $\pm\hat{l}$. Because of this, it is also called the axial state. This phase is stabilized at high pressures ($P > 21$ bar) owing to the strong coupling effects like the spin fluctuation feedback effect [2] [13]. A third superfluid phase, A_1-phase, $|A_1\rangle = \Psi_{1,1}(\mathbf{r})|\uparrow\uparrow\rangle$ is a fully spin polarized state and is only stable in the presence of an external magnetic field, although a minute presence of minority $|\downarrow\downarrow\rangle$ spin pairs has been discovered by Yamaguchi *et al.* [14]. The phase diagram in non-zero magnetic fields is shown in Figure 1-2. Transition from normal liquid into A phase or B phase is a second order transition, while transition between A and B phases is a first order transition. Application of a magnetic field destroys the polycritical point (PCP) by opening up a new phase, the A_1-phase between the normal and the A phase. In the presence of impurity like aerogel, many of the features on the phase diagram are altered, which is discussed in the following chapter.

Above the superfluid transition temperature, normal liquid ^{3}He can be described as an isotropic and homogeneous Fermi liquid possessing complete symmetry given by the symmetry group

$$G = SO(3)_L \times SO(3)_S \times U(1)_\phi \times P \times T \tag{1–7}$$

where L, S and ϕ represent the orbital space, spin space and gauge, respectively. G signifies that the free energy of the system in the normal state is invariant under separate rotations in spin space, in orbital space and under gauge transformation. In general, the superfluid transition is associated with broken gauge symmetry $U(1)$. In ^{3}He, in

addition to the broken gauge symmetry, a combination of several continuous symmetries are simultaneously broken. For example, in the B phase, the relative spin-orbit rotation symmetry is spontaneously broken while in the A phase, the relative gauge-orbit symmetry is broken. A complete description of superfluid ^{3}He is given by an order parameter written as a complex 3×3 matrix, $A_{\mu j}$ where $\mu = 1, 2, 3$ and $j = 1, 2, 3$ are the complex components in spin and orbital space, respectively. In principle, it is possible for many different superfluid phases to be realized due to the internal degrees of freedom associated with the spin and orbital space.

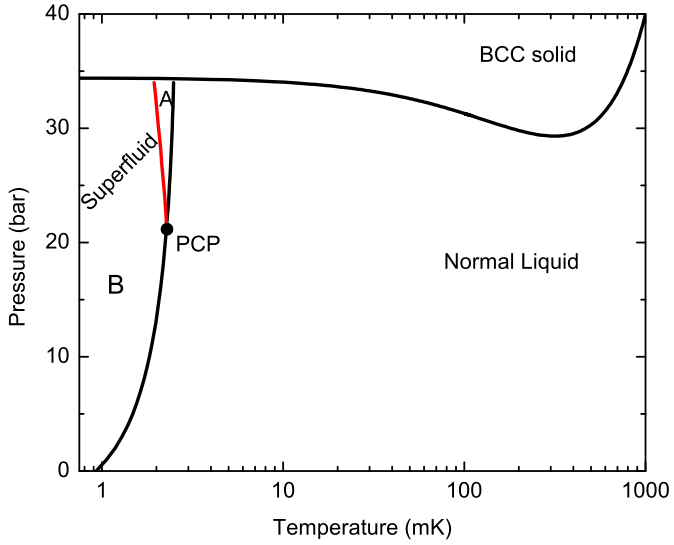

Figure 1-1. Phase diagram of superfluid ^{3}He in zero magnetic field. Note that the temperature axis is in logarithmic scale.

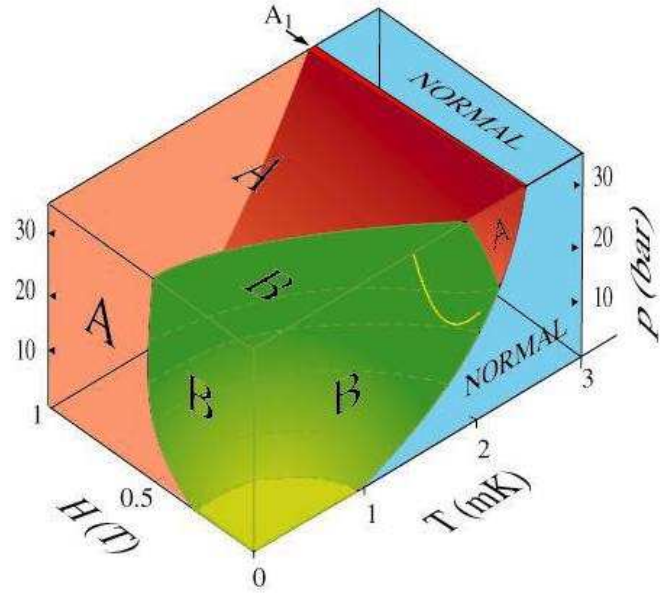

Figure 1-2. $P - H - T$ phase diagram of superfluid ^{3}He [15].

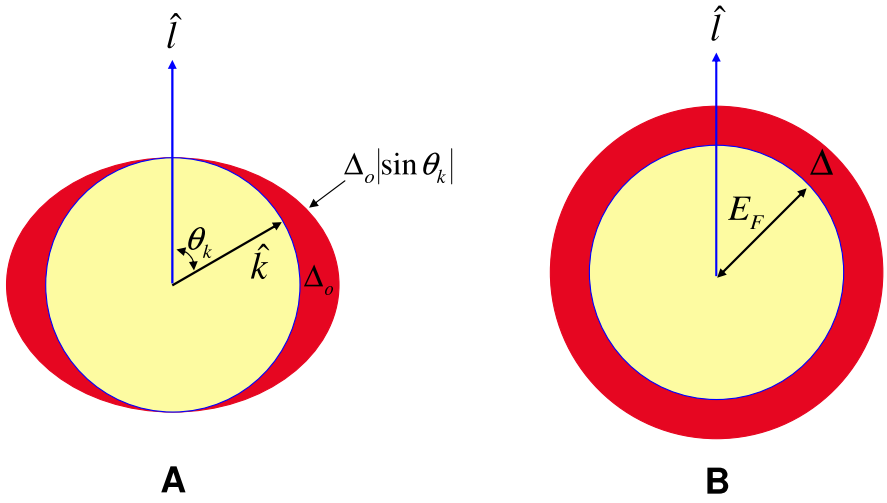

Figure 1-3. Schematic drawing of the energy gap Δ. A) The A phase. B) The B phase. Δ_o is the gap along the equator. E_F is the Fermi energy. The gap vanishes along the nodes ($\hat{l}$ vector) in the A phase while the B phase energy gap is isotropic.

CHAPTER 2
SUPERFLUID ^{3}HE IN AEROGEL

Superfluid ^{3}He introduced into a matrix of high porosity silica aerogel has been the subject of extensive study for the past 10 years. The unique structure of high porosity aerogel provides quenched disorder to otherwise practically disorder free system, which allows for a systematic investigation on the effects of disorder in a *p-wave* spin-triplet superfluid.

Silica aerogels are extremely porous, low density materials which can reach porosities of 98% or more. They consist of dilute network of thin SiO_2 strands with a diameter of $\delta = 3 - 5$ nm. The aerogel correlation length, which is the typical distance between silica strands or clusters is $\xi_a \approx 30 - 100$ nm. Figure 2-1 shows a 3D projection of porous aerogel structure simulated by Tom Haard [16]. Up to the length scale ξ_a, the aerogel structure forms a fractal dimension and beyond ξ_a it is found to be homogenous [17, 18]. The mean free path, ℓ, in a nominally 98% aerogel ranges between $150 - 200$ nm. The mean free path of ^{3}He quasi-particles varies as $1/T^2$, and since this term diverges at low temperatures, the quasi-particle scattering is dominated by the the aerogel in this limit. In the superfluid phase, the relevant length scale is the coherence length defined by $\xi_o = \frac{\hbar v_F}{2\pi k_B T_c}$, where T_c is the superfluid transition temperature in bulk ^{3}He and v_F is the Fermi velocity. The magnitude of ξ_o varies with pressure from 72 nm - 15 nm in the pressure range of $0 - 34$ bar, is much larger than the aerogel strand diameter ($\xi_o \gg \delta$), but is comparable to ℓ especially at lower pressures. Therefore, properties of the superfluid are significantly influenced by the aerogel acting as a dilute impurity in liquid ^{3}He with the aerogel strands as effective scattering centers.

Superfluidity in aerogel was first observed by the Cornell group [19] in torsional oscillator measurements and almost simultaneously by the Northwestern group [20] employing nuclear magnetic resonance (NMR) methods. Since then, numerous experiments were done in ^{3}He/aerogel system. The phase diagram in 98% aerogel is shown in

Figure 2-2 reproduced from [21]. In the usual case of *s-wave* superconductors, non-magnetic impurities do not change the transition temperature (Anderson Theorem) whereas in the case of *p-wave* pairing, all types of impurities cause a suppression of superfluidity. Specifically, in superfluid ^{3}He, the quasiparticle scattering from aerogel strands causes destructive interference of the pairing amplitude leading to a suppression of superfluidity that depends on the ratio ξ_o/ℓ, the pair breaking parameter. As seen in Figure 2-2, the aerogel superfluid transition, T_{ca}, is found to be below the bulk T_c value for all pressures. One conspicuous feature in the phase diagram is the appearance of a zero temperature critical pressure (P_c) around 6 bar below which no superfluid transition has been observed down to ≈ 200 μK [22].

2.1 Ginzburg-Landau Theory

Many of the qualitative features of the superfluid/aerogel system can be explained using the Ginzburg-Landau (GL) phenomenological theory. The free energy of the superfluid state can be expanded in powers of its order parameter ($A_{\mu j}$) for temperatures close to the transition temperature where the order parameter is small. The GL free energy functional of the order parameter, F_s is written as [2, 23, 24]

$$\begin{aligned} F_s = F_n + \alpha A^*_{\mu j} A_{\mu j} + \beta_1 |A_{\mu j} A_{\mu j}|^2 + \beta_2 (A_{\mu j} A^*_{\mu j})^2 \\ + \beta_2 A^*_{\mu j} A^*_{\nu j} A_{\nu i} A_{\nu i} + \beta_4 A^*_{\mu j} A_{\nu j} A^*_{\nu i} A_{\mu i} + \beta_5 A^*_{\mu j} A_{\nu j} A_{\nu i} A^*_{\mu i} \end{aligned} \tag{2–1}$$

where F_n is the free energy of the normal liquid, and μ represents the spin components and j represents the orbital components of the order parameter. Minimizing the free energy with respect to the β_i parameters, the free energies corresponding to the specific order parameters of the superfluid phases are found [23]. For $T > T_c$, α is positive in the normal state ($A_{\mu i} = 0$), for $T < T_c$, α is negative in the superfluid state and T_c is determined by the condition, $\alpha(T_c) = 0$. In the superfluid state, one has several possible solutions (minima) depending on the specific values of the β_i parameters. For instance, in pure superfluid ^{3}He, in the weak coupling limit, the B phase (BW state) is found to be

more stable [11]. But at high pressure, the β_i's differ from their weak coupling values due to strong coupling effects like spin fluctuations that promote the stability of the A phase over the B phase above the PCP. Here, we briefly describe a series of theoretical models that have been developed by Thuneberg *et al.* [23] and Sauls [21]. The general assumption for validity of these quasiclassical models is $\lambda_F \ll \xi_o$. The size of the impurity could be larger than λ_F, provided the volume fraction of the impurity is small. Further, the normal Fermi liquid properties such as the density, effective mass, quasiparticle interactions are assumed to be unchanged, only the superfluid properties are affected.

2.1.1 Homogeneous Scattering Model (HSM)

This model assumes that the elastic scattering of ^{3}He quasi-particles by the aerogel is isotropic and homogenous, meaning that the probability of scattering is the same irrespective of the location and direction. If the distribution of scattering centers in aerogel is $n(r)$, then under the assumptions of HSM, $n(r) = n$ is a constant density of impurities. The mean free path for scattering is given by the parameter $l_{tr} = (n\sigma_{tr})^{-1}$, where σ_{tr} is the transport scattering cross-section. The approximations used here are the same as the ones used for studying the effects of impurities in conventional superconductors [25, 26]. The suppression of T_c is found to have the same form as for the magnetic impurities in *s-wave* superconductors. The coefficient α in Equation 2–1 that determines T_c is given by [23],

$$\alpha = \frac{N(0)}{3}\left[\ln\frac{T_{ca}}{T_c} + \sum_{n=1}^{\infty}\left(\frac{1}{n-\frac{1}{2}} - \frac{1}{n-\frac{1}{2}+x}\right)\right] \tag{2–2}$$

where $2N(0)$ is the density of states at the Fermi surface and $x = \hbar v_F/4\pi T l_{tr}$. The transition temperature is plotted as a function of the ratio ξ_o/L in Figure 2-3 along with the experimental data. L is a characteristic length chosen such that the experimental measurements with different aerogel samples coincide at $\xi_o/L = 1$. The L values used to scale the different data are $L = 36$ nm [17], 25 nm [20, 27] and 24 nm [22]. The suppression of T_c at small coherence lengths varies quadratically as seen from experiments,

but the HSM model dependence is linear. At large coherence lengths, the observed suppression is much stronger than the model. Theoretically, HSM predicts the correct tendency for T_c, the order parameter amplitude $\triangle$, and the superfluid density ρ_s, but fails to give correct quantitative results.

2.1.2 Slab Model

This model confines ^{3}He between two parallel scattering planes separated by a distance D. The scattering is assumed to be diffusive. The dashed line in Figure 2-3 shows the calculated T_c. This model brings out the quadratic suppression of T_c at small ξ_o and proves to be better than HSM. However, this is not considered a good model because of its strong anisotropy. Especially, the anisotropy of this model is in contradiction with the experimentally observed NMR frequency shifts [20, 27]. The slab model with its strong anisotropic scattering can stabilize the A phase.

2.1.3 Isotropic Inhomogeneous Scattering Model (IISM)

IISM considers a periodic lattice of spherical scattering distributions with a radius R in order to consider the voids in the distribution of scatterers. The density of scatterers distributed within a sphere (unit cell), $n(r)$ has a polynomial form and depends only on the radial coordinate (r) as $n(r) = c[(r/R)^j - j(r/R)^{j+2}/(j+2)]$. So, the model is completely isotropic. As seen in Figure 2-3, compared to the HSM and slab models, IISM is in much better agreement with the experimental values of T_c especially for higher values of the radius $R = 5.6L$ and $j = 8$ implying a higher void-like and inhomogeneous regions.

Sauls and Sharma [21] determined a new pair breaking parameter by including the effect of aerogel correlations in this model. They assumed a random distribution of voids or low density regions in a relatively higher density region. The voids are distributed on a typical length scale of the aerogel correlation length ξ_a with a quasiparticle mean free path, ℓ. Since the pair correlation length ξ_o varies with pressure, there are two mechanisms affecting the superfluid transition temperature in aerogel (T_{ca}), that can be realized at two different limits of the length scales involved. Near the dense regions, T_{ca} scales as

$\delta T_{ca}/T_c \propto -(\xi_o/\xi_a)^2$, where T_c is the superfluid transition temperature in the bulk. When $\xi_o \gg \xi_a$, which happens at low pressures, the aerogel is homogeneous on the scale of the pair size. Then, T_{ca} depends on the homogenous scattering events defined by the quasiparticle mean free path ℓ. T_{ca} then scales as $\delta T_{ca}/T_c \propto -(\xi_o/\ell)$. Including both of these correlation effects, the effective pairbreaking parameter is given as $\tilde{x} = x/(1+\zeta_a^2/x)$ where $\zeta_a = \xi_a/\ell$. Based on this parameter, they calculate the pressure dependence of T_{ca} at all pressures and find good agreement with the experimental observations as shown in Figure 2-2 for fixed values of $\xi_a = 50.2$ nm and $\ell = 140$ nm .

2.1.4 Anisotropic HSM

The randomly oriented strands in aerogel are locally anisotropic which requires corrections for anisotropy to be included in the GL theory [23, 28, 29]. The aerogel can be considered as a randomly oriented distribution of rod-like strands of length ξ_a that possess a specific direction denoted by the unit vector $\hat{a}$. This modifies the quadratic (α) term in GL free energy Equation 2–1 to a tensorial form as $\alpha_{jk}A^*_{\mu j}A_{\mu k}$. The random field generated by the aerogel strands ($\hat{\mathbf{a}}$) couples to the the orbital vector $\hat{l}$ of the order parameter. The free energy contribution due to the anisotropy is represented as

$$f_a = -\alpha_{jk}a_j A^*_{\mu j}A_{\mu k}a_k \tag{2–3}$$

The free energy calculations yield that the $\hat{l} \perp \hat{a}$ configuration is favored [30]. It is found that with the inclusion of local anisotropic scattering from aerogel strands, GL free energy functional is similar to the HSM, but with different coefficients which affects the relative stability of the superfluid phases. In the following section we discuss on how the anisotropy plays an important role on the A-B transition in aerogel while focussing on the experimental observations.

2.2 Effect of Anisotropic Scattering

The isotropic scattering models satisfactorily explain the second order superfluid transition but the first order A-like to B-like transition in aerogel has raised various

questions. A number of experiments have been performed in aerogel probing the A-B transition as in the bulk [19, 20, 22, 31–34]. The results however seem to be rather contradictory in some instances. In all the experiments, supercooled A-B transition was observed at all magnetic fields including zero field, but the equilibrium A-B transition was not observed in zero field until recently [35, 36]. In particular, Gervais *et al.* [31] using an acoustic impedance method, observed supercooled A-B transition but found no A-B transition on warming in zero magnetic field. However, our group using the same acoustic cavity of Gervais found the A-B transition on warming at two different pressures. Figure 2-4 shows the zero field phase diagram of ^{3}He in aerogel (in blue) together with that of the bulk (in grey). It also displays the bulk A-B transition in a field of 1.1 kG. The two solid circles are the equilibrium A-B transition points in aerogel although there is a possibility of superwarming. These measurements also demonstrated that the A and B phases in aerogel coexist in a temperature width of about 100 μK. The A-B coexistence was also confirmed in the NMR experiments of Barker *et al.* [37].

From Figure 2-4, the slope of the A-B transition line in pure ^{3}He in the presence of a finite field is negative for $P > P_c$ and positive for $P < P_c$, where P_c is the polycritical pressure. From the two data points of Vicente *et al.* [35], the slope of the A-B transition line in aerogel is clearly positive which could mean that the phase diagram in the presence of aerogel is shifted up and there is a finite A-like phase even below the PCP at zero field. It was argued by us that the anisotropic nature of scattering form the aerogel could be responsible for the stability of the A-like phase below the PCP in zero magnetic field. Assuming that the aerogel generates anisotropy on the length scale of coherence length ξ_o, the additional free energy term given by Equation 2–3 would give rise to the A-B transition even in zero field for $P < P_c$. So, the inhomogeneity of the local anisotropy over length scales larger than ξ_o would result in the coexistence of the A and B phases. Vicente *et al.* [35], estimated that a fraction of 1% anisotropy is enough to produce the observed A phase width. The free energy contribution from the applied magnetic field B in bulk ^{3}He

has a form similar to the anisotropy (f_a) term given in Equation 2–3:

$$f_z = g_z B_\mu A_{\mu j} A^*_{\nu j} B_\nu \tag{2–4}$$

In this case the magnetic field couples to the spin component of the order parameter. Analogously, in the f_a term, the random field generated by the aerogel strands couples to the order parameter through the orbital channel. The f_z term (Equation 2–4) also gives rise to the quadratic suppression of the A-B transition temperature (T_{AB}) in the bulk, given by,

$$1 - \frac{T_{AB}}{T_C} = g_a(\frac{B}{B_o})^2 + \vartheta(\frac{B}{B_o})^4 \tag{2–5}$$

where g_a is the strong coupling parameter [38] that depends on the coefficients of the fourth order invariants of the free energy functional in the GL theory [2]. g_a (in bulk) shows strong divergence near PCP [39]. However, in the presence of aerogel this parameter was not found to diverge, below the melting pressure [31]. This somewhat contradicts the observation of a supercooled A-B transition at zero field. As stated by Gervais *et al.* [31], this could mean that the PCP occurs above the melting pressure which is experimentally inaccessible. A similar phenomenon has been observed in ^{3}He-^{4}He mixtures in high porosity aerogel [40], where a coexistence region of the two superfluids develops with no polycritical point in the phase diagram.

Although current experiments suggest the existence of the B-like phase in aerogel to be stable, there are questions of stability on the A-like phase. One cannot always be sure that the phases in pure ^{3}He correspond to the phases in the aerogel. In fact, disorder can stabilize new phases that are not realized in the bulk. For instance, based on the Imry-Ma effect [41], it has been argued by Volovik [42, 43] that the local random anisotropy of the strands interacts with the anisotropic order parameter, especially the orbital vector ($\hat{l}$) that could stabilize the A-like phase (Imry-Ma state) with a short range orientational order or a random texture of $\hat{l}$. The length scale of this short range order is estimated to

be $\approx 1\mu$m. On the contrary, a brand new class of ESP state called the robust phase has been proposed by Fomin [44] as a likely candidate for the A-like phase.

2.2.1 Compressed and Stretched Aerogels

We proposed that the effect of anisotropic scattering can be systematically investigated by introducing global anisotropy in addition to the local anisotropy simply by applying uniaxial stress to the aerogel [35]. Aoyama and Ikeda [45] independently performed rigorous theoretical calculations incorporating global anisotropic scattering for compressed as well as stretched aerogels. The cartoon shown in Figure 2-5 depicts the different orientations of the orbital component of the order parameter ($\hat{l}$) when the aerogel cylinder is compressed and stretched. The blue lines can be visualized as aerogel strands and the red arrow indicates the orbital $\hat{l}$ vector coupled to the aerogel strand having different orientations for compressed and stretched aerogels. Figure 2-6 shows the theoretical calculations of Aoyama and Ikeda for the phase diagram of superfluid ^{3}He in compressed and stretched aerogels. Their calculation confirms our argument on the effect of anisotropy. As seen from Figure 2-6(a) and (b), the PCP is pushed up beyond the melting pressure and the width of the A-like phase is broadened and appears at all pressures in both uniaxially compressed and stretched aerogels. Additionally in the case of stretched aerogel, 2-6(b) shows a completely new phase: the 1D-like polar phase developing between the normal liquid and the A-like phase. Recently, Volovik [43] also considers the effects of global anisotropy and finds that squeezing or stretching the aerogel destroys the Larkin-Imry-Ma effect leading to a global orientation of the order parameter.

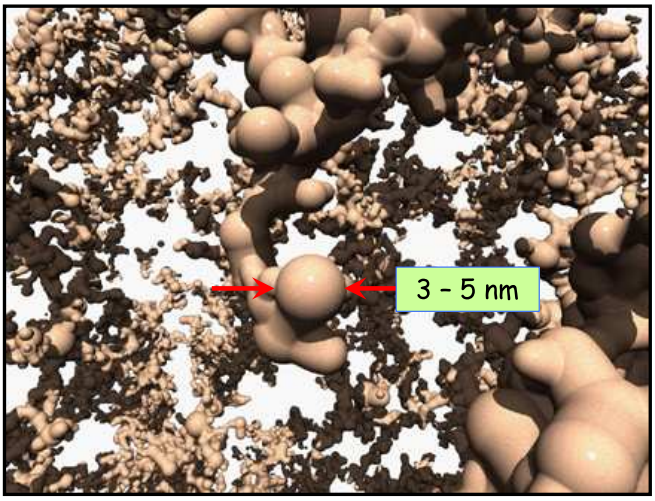

Figure 2-1. Simulated picture of aerogel structure by Tom Haard [16]. The typical diameter of the SiO_2 beads is 3-5 nm.

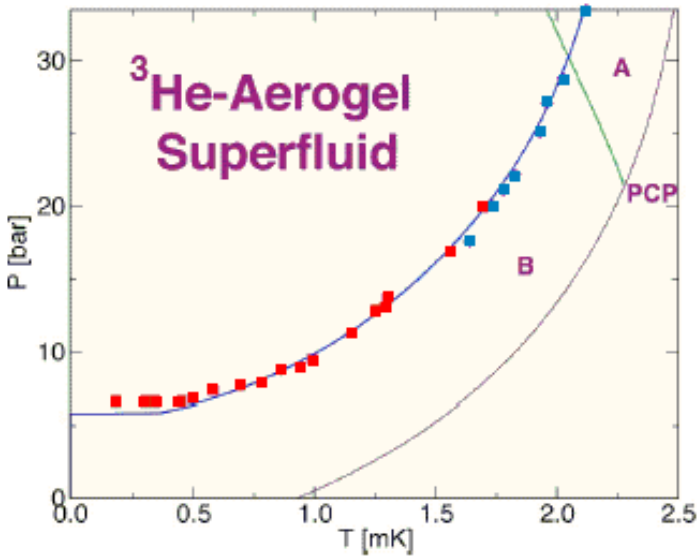

Figure 2-2. Superfluid transition in aerogel. Blue dots are data from Gervais *et al.* [31] and red dots are data from Sprague *et al.* [20]. Blue line is the theoretical curve from [21]. Phase boundaries for pure ^{3}He are also shown. [Figure reproduced with permission form J. A. Sauls and Priya sharma, Phys. Rev. B **68**, 224502 (2003). Copyright (2003) by the American Physical Society.]

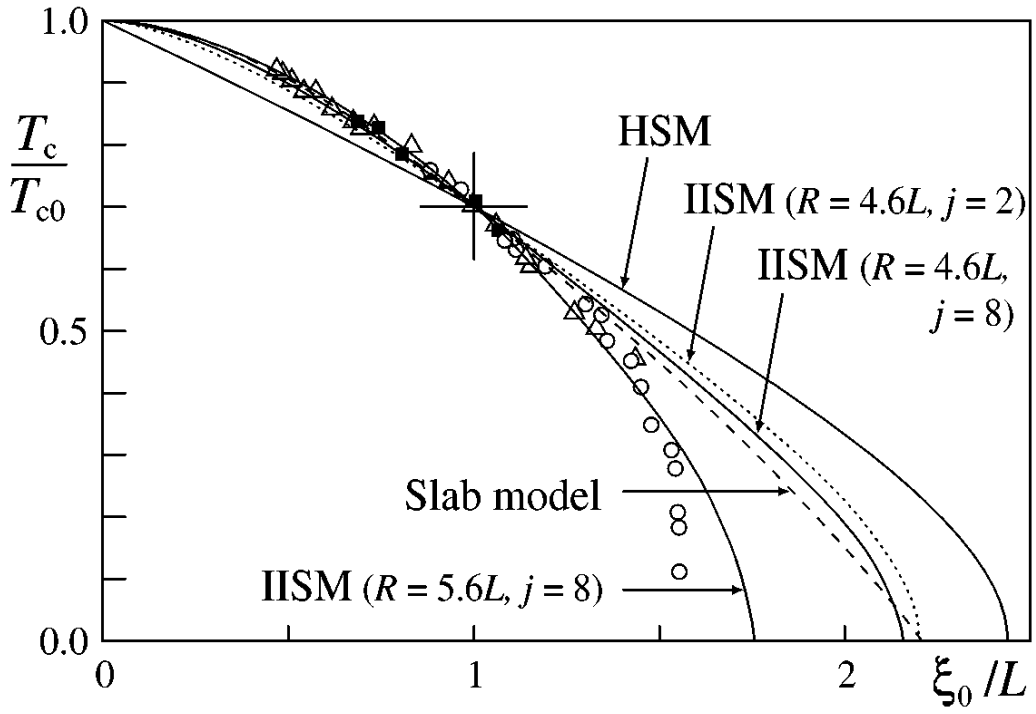

Figure 2-3. Superfluid transition temperature in ^{3}He/aerogel relative to the bulk. The x-axis is the coherence length over length L chosen (see text) so that the different data sets coincide at the cross. The lines correspond to the HSM model, the slab, and the IISM models with different scattering parameters. [Figure reproduced with permission form E. V. Thuneberg *et al.* Phys. Rev. Lett **80**, 2861 (1998). Copyright (1998) by the American Physical Society.]

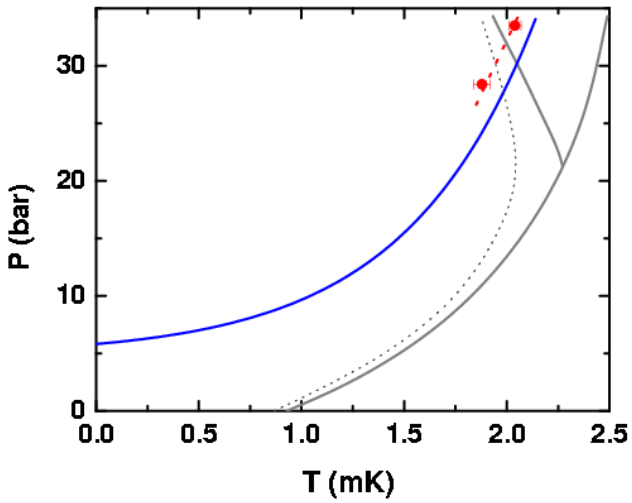

Figure 2-4. Phase diagram of bulk superfluid ^{3}He is shown in grey lines. Dotted grey line is bulk A-B transition line in a finite field of 1.1 kG. Superfluid transition in aerogel is shown in blue while the A-like to B-like transition in aerogel is shown in red. Red points show the equilibrium A-B transition at two pressures. [Reproduced with permission from Vicente *et al.* Phys. Rev. B **72**, 094519 (2005). Copyright (2005) by the American Physical Society.]

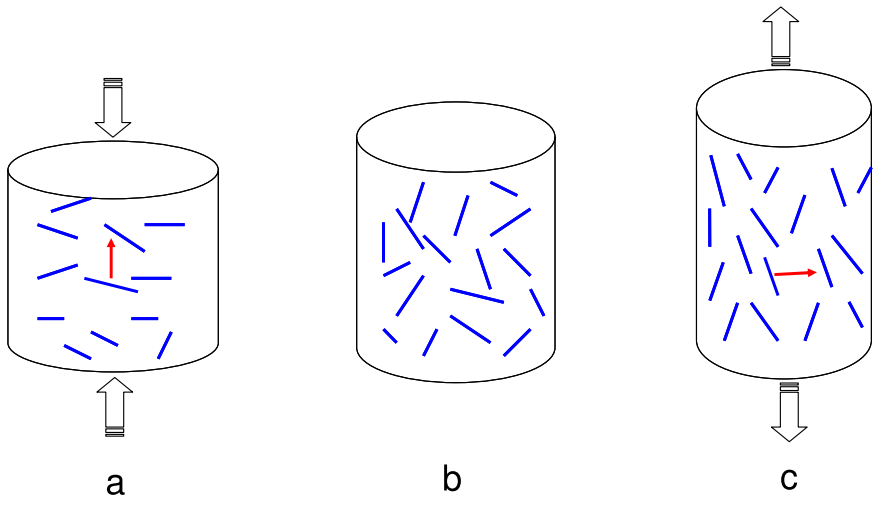

Figure 2-5. Cartoon of aerogels compressed and stretched along the cylinder axis. a) Compressed aerogel b) Uncompressed aerogel c) Stretched aerogel. The blue lines depict the aerogel strands and the red arrow shows the direction of the orbital component of the order parameter relative to the compression axis.

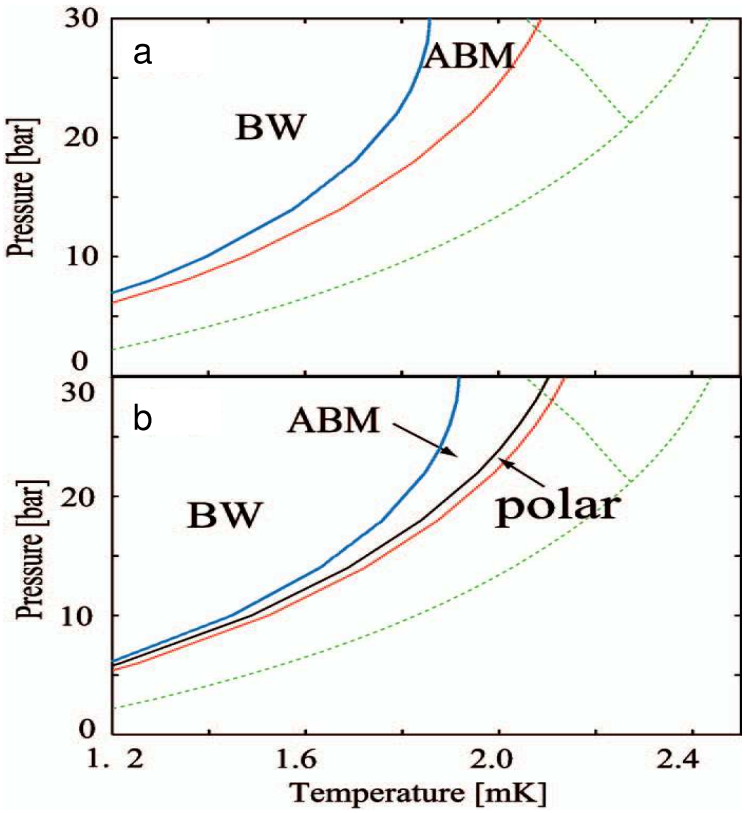

Figure 2-6. Theoretical predictions of the phase diagram of superfluid ^{3}He in anisotropic aerogels. a) ^{3}He in compressed aerogel (b) Stretched aerogel. [Reproduced with permission from K. Aoyama and R. Ikeda, Phys. Rev. B **73**, 060504(R) (2006). Copyright (2006) by the American Physical Society.]

CHAPTER 3
CONSTRUCTION OF AN ULTRA LOW TEMPERATURE CRYOSTAT

The cryostat is named "Thule", synonymous with "the coldest region of the habitable world" or "extreme limit of travel and discovery." Thule is housed in the physics building room B131 and has been constructed over a period of 3 years. It is a combination of Kelvinox 400 dilution refrigerator from Oxford Instruments and a copper nuclear demagnetization stage (CDS) capable of performing experiments at sub-millikelvin temperatures. In this chapter, we begin by describing the design and construction of the various parts of the cryostat starting from the outer structures and progressing toward the inner parts of the cryostat and discuss the performance of the cryostat in the end.

3.1 Cryostat Support Structures

Environmental vibrations are one of the crucial factors affecting the cryostat's performance in reaching low temperature and maintaining that temperature for an extended period of time as well as in providing low noise environment for various measurements. Ambient vibrations can easily couple to the cryostat through various pumping lines and support structures. Any motion transmitted from the outer to the inner metallic parts of the cryostat in a strong magnetic field can generate eddy current heating. It is imperative that vibration isolation techniques be implemented to minimize the vibrations wherever possible. Figures 3-1 and 3-2 show the design of the cryostat and its outer structures, respectively. The cryostat is suspended from the center of an aluminum top plate which is mounted on a four legged columnar aluminum structure with air cushions on its four corners. The aluminum structure is bolted down on a concrete pit isolated from the building floor. When the fridge is not running, the pit also houses the dewar and the superconducting magnet system.

3.1.1 The Top Plate

The top plate is a $0.75^{"}$ thick aluminum with dimensions $49^{"} \times 55^{"}$. The center of the plate has a $10^{"}$ diameter cut-out through which the insert protrudes. A drawing of

the plate is shown in Figure 3-3. The top and bottom surfaces of the plate are smoothed to a diameter of 16" around the insert hole for o-ring seals with the insert and the dewar, respectively. So far, the o-ring seal of the insert flange on the top plate has been changed once, as it had developed a leak. Six lead bricks, each weighing about 20 lb are bolted to the bottom of the plate to reduce its vibration amplitude. The plate sits on 4 gimbal piston pneumatic isolators manufactured by TMC (Micro-g #14-132-00), mounted on the aluminum structure. The isolators allow the top plate along with the insert and dewar to float on the pistons pressurized with air or nitrogen gas. Care should be taken while floating the cryostat so that the plate is level in the horizontal plane. This can be achieved with the help of a circular bull's eye level attached on top of the plate.

3.2 The Pumping Systems

There are three pumps that run the dilution fridge, a helium sealed rotary vane pump (Trivac B, Leybold), a roots blower pump (EH500, Edwards) and a ^{4}He rotary pump (RV12, Edwards). Apart from these, we also have a utility pump which is used for cleaning the liquid nitrogen traps and for other miscellaneous purposes. All the pumps are situated in the service corridor behind the lab and the pumping lines pass through the corridor concrete wall and various vibration isolation stages before being connected to the cryostat. The main pumping line (still), the ^{3}He return line, the bath pumping line and the 1K pot pumping line are all connected through the back of the intelligent gas handling cabinet (IGH) supplied by Oxford, and can be controlled from the IGH front panel. The roots pump is mainly for boosting the circulation rate of ^{3}He and is used in series with the Trivac B. The ^{4}He rotary pump is used for pumping the bath and the 1K pot. The recommended oils for the ^{3}He rotary and the booster pump are Alcatel 111 and Edwards ultra grade 20, respectively. To date, these two pumps never required any servicing or oil change as can be expected for a closed cycle circulation system maintaining high purity. The oil for the ^{4}He (1K pot) pump, ultra grade 19 has been changed a few times and one has to check for the oil level and change it if necessary before each cooldown. In addition

to the above mentioned pumps, we have a mobile pumping station equipped with a turbo pump (BOC Edwards, EXT255H) and a rotary backing pump (RV3), that is used to pump the Dewar jacket or the inner vacuum can (IVC). The turbo pump is extensively used in conjunction with the leak detector during all the leak detecting procedures.

3.2.1 The Still Line

The pumps generate a substantial amount of vibration that has to be prevented from coupling to the cryostat. The still pumping line is a stainless steel pipe, 4" in diameter and consists of three stages of vibration isolation between the roots blower and the cryostat. It has two T-shaped bellows in mutually orthogonal planes and a specially designed double gimbal bellows inserted right in front of the opening to the cryostat. This structure is designed to have a resonance frequency below 2 Hz and is shown in Figure 3-4. Considering only the largest restoring force, $T = \pi r^2(P_i - P_o)$, arising due to the difference in the pressure inside (P_i) and outside (P_o) the bellows with a radius r, the resonance frequency is given by [46, 47], $\omega = (\epsilon T/4R^2 m)^{1/2}$ where m is the mass of the structure ≈ 10 kg. The U-shaped support of the double gimbal bellows rotates about the gimbal pivots at the base of the bellows by a small angle θ. $\epsilon \approx 2"$ is the distance between the pivots of the gimbal and the point where the bellows start to flex and $R \approx 18"$ is the distance between the base of the bellows and the point where the supporting string is attached to the elbow (see Figure 3-4).

The still line protrudes into the lab by about 5 feet from the corridor wall and is supported vertically by nylon slings and steel cables from the ceiling. The slings are coupled to steel cables with turnbuckles so that the length and tension can be adjusted. This might be necessary while floating the cryostat, since the double gimbal bellows also rises slightly during the floating procedure. The stainless steel flexible pumping line at the back of the ^{3}He rotary and from the roots blower pump passes through a cylindrical container filled with lead shots. The cylinder sits vertically on three spring studs bolted to the ground allowing further reduction in vibrations transmitted from the pumps.

3.2.2 The Pot and Dewar Line

The 1K pot pumping line and bath pumping lines from the pump are routed through the IGH cabinet to the cryostat. From the IGH, stainless steel bellows lines are converted to PVC tubing (Schedule 80) and finally to flexible metal bellows before being connected to the cryostat. Because of the different acoustic properties of steel and plastic, vibrations transmitted from the pump are damped or reflected away from the cryostat. The plastic also allows for electrical isolation from the cryostat. These lines are supported by Unistrut structures bolted to the ceiling.

3.3 Gas Handling Systems

3.3.1 ^{3}He Gas Handling

The ^{3}He gas handling system (GHS) is a high purity and high pressure ^{3}He station used for pressurizing and condensing liquid ^{3}He, our sample. The panel is mounted to the wall next to the IGH cabinet. It has three storage tanks in which high purity isotopic grade ^{3}He gas (99.9999%, Isotec) is stored. The GHS is equipped with a liquid nitrogen cold trap and a charcoal dipstick used to pressurize the sample cell and the melting curve thermometers. The pressure can be monitored through a Heise bourdon gauge and a high precision quartz pressure transducer (Quartzonix model 970, Pressure Systems, Inc.) with electronic readout through RS-232. A picture of the gas handling system is shown in Figure 3-5. The liquid nitrogen trap has developed leaks and resulted in some loss of ^{3}He. It is now replaced with a newly designed trap that has a volume $\approx 5\ cm^3$. The total volume of the ^{3}He gas lines in the panel excluding the storage tanks and the cold traps is $\approx 4.5\ cm^3$. The ^{3}He pressure in the two storage tanks together is 35 psi with volumes of 4 liter and 5.12 liter as of 04/15/09.

3.3.1.1 Gas Capillaries

All gas capillaries run through the vacuum space to minimize the influence from the LHe bath level and care was taken to reduce thermal touches with the inner wall of the vacuum port. There are three fill-lines installed on the cryostat, starting with 0.0625"

O.D. stainless steel tubes from the gas handling system (GHS): one for the melting curve thermometer that splits into two capillaries at the top of the cryostat (for the two MCTs) and the remaining two for the experimental cells which are isolated from the GHS by high pressure valves. The stainless steel tubes are hard-soldered to a KF25 brass flange that connects to one of the ports on top of the cryostat. Right after the brass flange in the vacuum side, the stainless steel tubes are converted to 0.03" O.D. Cu-Ni capillaries. They are clubbed together and passed through a teflon tube. A stainless steel metal disk with a threaded rod attached at its center is welded to a KF25 o-ring at the entrance of the port and several evenly spaced discs along its length guided the capillaries down to the 4K flange. At the 4 K flange, about 6" of Cu-Ni capillaries are wrapped around and soft-soldered to a copper post for heat sinking. At the 1K plate, they are converted to thinner diameter (0.016") Cu-Ni capillaries and heat-sunk using a copper post and silver epoxy (Epotek H20E). The four capillaries extend down to the nuclear stage with heat sinks at the cold plate, the mixing chamber and the top plate of the copper nuclear stage. Recently, one of the ^{3}He capillaries on the top of the cryostat has been converted to a ^{4}He capillary for measurements in a liquid ^{4}He cell mounted on top of the nuclear stage.

3.3.2 Oxford Intelligent Gas Handling (IGH)

The Kelvinox intelligent gas handling system (IGH) supplied by Oxford is used to circulate and condense the ^{3}He/^{4}He mixture into the dilution refrigerator. A schematic of the IGH is shown in Figure 3-6. The valves on this system can be operated manually or remotely via a computer using the LabView software provided by Oxford. All the pressure gauges on the IGH cabinet are read in units of mbar. Gauges labeled P1 and P2 are pirani gauges for pressure range between 0-50 mbar, while gauges named G1, G2, G3 are gauges for pressures above 50 mbar. Valve V4 on the IGH was found to leak through even when closed and attempts to replace it have failed due to stripped screws that need to be removed in order to change the valve. Since then it has never been used. The one-way safety valves inside the IGH open up at a differential pressure of 700 mbar. A crossover

line to the still pumping line shown as red line in Figure 3-6, emerging from the back of the IGH has been installed to facilitate easy access to the mixing chamber during leak checking procedures. Apart from handling of the mixture, the IGH-Femtopower panel in the same cabinet monitors the temperature and controls the heat applied to the different parts of the dilution: the still, sorb and the mixing chamber.

3.4 Electrical Systems

The following electrical connectors emerge form the top of the cryostat: (1) two circular 19-pin magnet station connectors labeled as 2T and 8T, (2) Twelve hermetically sealed coaxial connectors (factory installed) and (3) two 24-pin Fischer connectors for diagnostic and experimental use (factory installed). Apart from these, we run home made coaxes and twisted pairs through the vacuum space. The twisted wires are used for LHe level monitor, heat switch power supply, magnet voltage sensing and persistent heaters and other diagnostic resistors and heaters. The wire mapping between the two connectors and their assignment is shown in Table 3-3. The wires from the 19-pin magnet station connectors are connected to the demagnetization magnet power supply through an intermediate measurement box (labeled as IMB) on the instrument rack.

3.4.1 Homemade Coaxes

The Oxford installed coaxes on the top of the cryostat extend down only to the 1K plate where they terminate on two L-shaped copper supports with coaxial connectors. Later, one of the L-supports was removed and a copper encloser was designed with the solder connections inside the block for better shielding. Twelve home-made coaxial lines extend down to the nuclear stage from this connector block. Formvar insulated NbTi superconducting wires ($\varnothing 0.0042"$) from Supercon, Inc. were passed through $\varnothing 0.016"$ Cu-Ni capillary tubes to form semi-rigid coaxial lines for low frequency measurements. They are typically about 5 feet long and are heat-sunk the same way as the fill-lines using silver epoxy and copper posts anchored at the 1K, the cold plate, the mixing chamber and the nuclear stage. Two of the coaxes were short to ground after thermal cycling and

remain disconnected presently. A new set of commercial coaxes (Cooner) with Cu-Ni plated NbTi inner conductor and stainless steel outer conductor were run from the 1K pot to the top plate of the nuclear stage. Below this, they are attached to semi-rigid copper coaxes (UT-47C, Micro-coax) extending along the length of the nuclear stage. They are glued to the copper nuclear stage along their length using conductive silver paste (Pelco 187, Ted pella Inc). Table 3-1 summarizes the assignment for the 12 Oxford coaxial cables.

For high frequency ultrasonic sound measurements, three 50 ohm coaxial lines run from the top of the cryostat into the vacuum space in three different stages. In the first stage, rigid coaxes with Cu-Ni outer conductor and silver plated Be-Cu inner conductor are connected to hermetically sealed SMA terminators inside a KF50 brass can on the top plate of the cryostat. They are thermally anchored to a copper plate on the 4K flange. Microminiature coaxial connectors (MMCX) from Microstock, Inc. are connected to this end and mated to a right angled male MMCX connectors (16MMCX 50-1-4C). The second stage extends form the 1K plate to the top plate of the nuclear stage. This stage consists of Cooner coaxes heat sunk along the dilution unit. The third stage employs thin copper coaxes ($\varnothing 0.047''$) with silver plated Cu inner conductor, thermalized to the nuclear stage with silver paste. They are carefully soft soldered to the superconducting coaxes at one end and shielded with copper tape and the other ends at the bottom were terminated with female MMCX connectors (21MMCX 50-2-1C) in the experimental region.

3.4.2 Twisted Pairs

Two pairs of twisted wires run from the room temperature to the experimental region through the vacuum space for transport measurements. They run together with the fill-lines with a KF25 tee on top of the cryostat. A miniature (4-pin) hermetic electronic connector was soft soldered into the KF25 flange on the vacuum port. At room temperature, the pairs are twisted copper wires with in-line EMI filters (Tusonix Inc., TUS4251-004). The filters, mounted inside a copper shielded can with a 4-pin hermetic connector mates to the vacuum port connector. The twisted pairs and the gas

capillaries have been isolated from each other and the vacuum port wall by stainless steel spacers as described in section 3.3.1.1. The copper wires have been heat sunk at the 4K flange around a copper post using GE varnish. At the 1K plate, the copper wires were soft soldered to NbTi superconducting wires and heat sunk. The superconducting wires were also twisted in pairs and run all the way to the bottom of the nuclear stage with heat sinks at the still plate, the cold plate, the mixing chamber and the nuclear stage. A shielded twisted pair cable bridges the cryostat to the home-made distribution box where the individual wires from the twisted pairs turn into coaxial lines for shielding. Recently two more twisted pairs of superconducting wire were added from the 1K pot to the top of the nuclear stage for future use.

3.5 Dewar

The liquid helium dewar was purchased from Kadel Engineering. It is a vapor shielded dewar with a 10" diameter fiberglass neck. The dimensions of the dewar are shown in Figure 3-7. It makes an o-ring seal (14.5" I.D and 0.25" thick) with the bottom part of the top plate. The belly part of the dewar has a 64.7 liter capacity. The dewar is maneuvered by counterweight. The vacuum in the dewar jacket can be checked and maintained by pumping from a bellows sealed valve attached to the side of the dewar. The LHe level in the bath space is measured using an American Magnetics level meter. It has an active length of 55.5" and runs from just above the last radiation baffle to the bottom of the dewar. It is clamped with a ring-nut at the magnet support ring and affixed at various places down the magnet structure, so that it lies just an inch above the bottom of the dewar. The boil-off rates with and without the magnet running are 0.8 liter/hour and 0.6 liter/hour (with leads lifted) respectively. In normal operation, one full transfer lasts 2.5 days. The bath has three diagnostic resistors placed at the top of the IVC (R1), at the Magnet support ring (R2) in the middle and one at the bottom of the dewar (R3). A 25 W heater is attached at the bottom of the magnet for boiling off LHe during warm-up. The nominal resistance values at RT, 77K and 4K are provided in the Table 3-2.

3.6 The Dilution Refrigerator

Kelvinox 400 dilution refrigerator, manufactured by Oxford instruments is the heart of Thule providing continuous refrigeration at mK stage. Two stainless steel support rods were added in between the 4K and the 1K plate and between the cold plate and the mixing chamber plate to provide additional mechanical strength. A picture of the fridge is shown in Figure 3-8. In the test run, when the fridge was first installed, the cooling power was measured $\simeq 350\mu W$ at 100 mK with 40 mW applied heat to the still. The minimum temperature was 6.78 mK as measured by a ^{60}Co nuclear orientation thermometer provided by Oxford. After the initial commission run, the copper nuclear demagnetization stage and a melting curve thermometer (MCT) were installed and the lowest temperature recorded with the full load was 5.2 mK determined by the MCT. Cooling power measurements were performed at its base temperature. Figure 3-9 shows the plot of the power applied ($\dot{Q}$) to the mixing chamber vs. the square of its steady state temperature (T_m^2). The linear dependence [48], $\dot{Q} \propto 84\dot{n}_3 T_m^2$ gives us a ^{3}He circulation rate ($\dot{n}_3$) of 187 μmoles/s and an ambient heat leak of 0.46 μW at a still power of 4 mW.

The dimensions of the inner vaccum can (IVC) and the copper radiation shield supplied by Oxford are shown in Figure 3-10. The shield is attached at the cold plate of the dilution refrigerator and has a removable bottom for a visual inspection during the centering of the copper bundle and checking for any touches from inside the shield. The centering, if needed, is done by adjusting the M3 nuts at the still plate. The IVC is made of stainless steel and is provided with a removable indium sealed cap at the bottom. It has copper sheath covering about 1/3 of its length from the top for thermalization to the bath since the bath level drops below the 4 K flange. In fact, the temperature of the 4K flange can actually go up to 8-10 K when the LHe level goes below it. This was first noticed when the heat switch magnet wire (NbTi) soft soldered to copper wire and heat sunk at the 4K flange turned normal and the problem was only resolved by moving the joint to the 1K pot. For this reason, any superconducting joints have to be heat sunk at the 1K pot.

3.7 Heat Switch

A superconducting indium (In) heat switch was designed and installed. A 3/8" diameter pellet cut-out from a 0.034" thick high purity indium sheet has been indium soldered on to the gold plated copper fingers connecting the mixing chamber plate and the top plate of the nuclear stage. Both the copper fingers were annealed before gold plating to prevent oxidation of the surface. Figure 3-11 shows the design of the switch. The nuclear stage was mechanically supported by four Vespel rods (SP22, Dupont) attached to the bottom of the mixing chamber. The thermal coupling and decoupling was achieved by driving the In metal into normal or superconducting state by switching (on/off) a critical magnetic field of 280 G generated by a home-made superconducting solenoid. The indium strip at the center of the solenoid was oriented so that the heat flow was perpendicular to the magnetic field in order to avoid a thermal short through the trapped magnetic flux lines while switching the field. The solenoid coil was wound with a 0.0042" diameter insulated NbTi superconducting wire (type SW-18) with CuNi cladding purchased from Supercon, Inc. The coil consists of 14 layers, each 0.8" long (190 turns/layer) on a bakelite magnet former with dimensions 0.5" I.D and 0.56" O.D. Each layer was coated with a thin layer of GE varnish glue and dried before winding the next layer. The superconducting leads from the coil extend continuously all the way up to the 1K pot. The wire was heat sunk at every plate of the dilution unit from mixing chamber to the 1K plate by winding the wire around copper posts and glued with GE varnish.

The magnet is surrounded by a Nb shield (0.75" I.D and 0.81" O.D) to confine and homogenize the field within and to protect it from the fringe field of the demagnetization magnet. The shield and the magnet are thermally anchored to the mixing chamber by a copper encloser glued to the shield using silver paste. The central field of a solenoid inside a concentric cylindrical superconducting shield is given by [48, 49],

$$B_s = \frac{B_o}{1 + \frac{A_c}{A_s - A_c}} \tag{3–1}$$

where B_o is the magnetic field without the shield and $A_s(A_c)$ is the cross-sectional area of the shield (coil). Using the dimensions of the Nb shield and the solenoid in Equation 3–1 should give about 44% reduction in the the field with the shield. The magnetic field generated by the solenoid with and without the superconducting shield has been characterized by a hall probe (Lake Shore Cryotronics Inc., model HGCA 3020) at 4.2 K, up to a current of 1.5 A. Figure 3-12 shows the field generated as function of the applied current. The shield reduced the field-to-current ratio of the solenoid by $\approx$ 50%. Under normal operation the magnet is energized by a current of $\approx 0.75\ A$ with a home-made low noise magnet power supply. The power supply equipped with a battery backup for about an hour was built by the electronics shop of the physics department. It is designed to provide a current output of 1 A. The voltage and current levels can be set by potentiometers which, if exceeded, will instantly ramp down the current supply. At least 2 min of elapsed time is recommended for equilibration of current at the final set value.

3.8 The Nuclear Stage

A high purity (OFHC) solid copper rod, 2" in diameter and 17.54" long was machined as shown in Figure 3-13 to form the nuclear demagnetization stage. A separate 3.5" diameter and 0.375" thick copper plate was electron beam welded to the longer section to form the top plate of the stage providing additional experimental space. A superconducting magnet from American Magnetics Inc., produces a maximum field of 8 Tesla at the center of the CDS. The high field region of the copper has slits machined along its symmetry axis to reduce eddy current heating. The amount of copper in the field gradient regions was also kept to a minimum. The CDS has a total of 48 moles of copper. An important step performed for improving the purity of the copper and thereby substantially improving its thermal conductivity at low temperatures was annealing. The copper was annealed in a vertical vacuum oven supported by a stainless steel structure specifically designed for this purpose. Prior to annealing the copper, the stainless steel

support structure was heat treated at 990°C for 1.5 hrs in the partial pressures of 92% helium and 8% hydrogen. The goal was to produce a gray or greenish colored oxide layer on the steel that was necessary to protect the copper from sticking to the structure during its annealing. The copper was annealed at 900^oC for about 60 hrs in high vacuum. A picture of the annealed copper along with the grayed steel structure is shown in the Figure 3-14. Before the heat treatment, the oxidation on copper was removed by Citranox and later rinsed thoroughly in deionized water solution. Following the heat treatment, to prevent oxidation and improve thermal contact with the experimental regions and the heat exchanger to the liquid ^{3}He, the top and bottom flanges of the CDS were gold plated to a few microns thick. The residual resistance ratio was not measured.

3.9 Heat Exchanger

Two different heat exchangers have been designed for cooling the liquid ^{3}He sample. The two designs differed in their contact method with the nuclear demagnetization stage. In the first design, a clamp type grip was implemented instead of a conventional bolt joint. A 3" long silver rod (⌀0.375") of 99.99% purity and a 0.25" thick silver plate (⌀1.25") were welded together. A total of 32 body holes (⌀0.033") were drilled through the silver plate at different bolt circles and 0.032" diameter silver wires were punched into these holes. This piece was annealed at 800°C in a tube furnace (Thermolyne type 21100) for 12 hours. Afterwards, 700 $\mathring{A}$ Japanese silver powder was packed onto the silver plate at 45% packing fraction using a Carver laboratory press (in Prof. Meisel's lab) at 200 atm pressure. The powder was packed in 6 layers to a height of 0.35". A number of 0.036" holes were drilled on the packed silver surface to a depth of 0.2" to improve the contact between the silver and the surrounding liquid. The estimated surface area was $\approx 50\ m^2$ based on the amount of silver powder packed and considering ≈ 2 m^2/g surface area as determined by [48, 50] for the same silver powder. A phosphor bronze cell body enclosed the packed silver heat exchanger plate and were epoxied together with stycast 2850FT for a leak tight seal. A separate copper flange 2" O.D, 0.25" thick with a 1" long, 0.575"

O.D, cylindrical section at its center were machined from one piece. A 3/8" body hole was drilled at the center of this piece and slits were milled along the cylindrical axis of the bottom section. This produced a collet-like structure that could be radially squeezed. The piece was annealed, gold plated and bolted to the bottom of the CDS. The heat exchanger silver rod along with the cell body was inserted into the center hole of the copper collet and tightly clamped with a phosphor bronze clamp that firmly gripped the silver rod by pressing copper against it. This design shown in Figure 3-15(b) was implemented for its ease of use in demounting the cell along with the heat exchanger. In the initial experiments with this exchanger, thermal hysteresis on cooling and warming with a temperature difference of $\approx 300\mu$K was observed and attributed to the insufficient contact made by the clamp. Later, an improved exchanger was designed. This is depicted in Figure 3-15(a). Two silver plates of appropriate diameters were welded directly to the two ends of a 3/8" silver rod, eliminating the radial clamp in the previous design. Silver powder was pressed at one end to form the top part of the experimental cell enclosing the ^{3}He volume and to the other end a new melting curve thermometer was attached. The whole assembly with the experimental cell including the thermometer was bolted to the bottom of the CDS. Silver powder was packed as discussed above and provided a surface area $\approx 43\ m^2$. Experiments with this exchanger eliminated the drastic thermal gradients. This is discussed in more detail in chapter 6. For future experiments, only the bottom part of the cell with an indium seal needed to be designed.

3.10 Demagnetization and Experimental Magnet

The superconducting magnet system (American Magnetics Inc.) is composed of an 8 tesla magnet for demagnetization and a 2 tesla magnet for the experimental region, including compensation magnets. The compensation magnets provide low field region above the nuclear stage and minimize coupling between the demagnetization magnet and the experimental magnet. Figure 3-16 shows the important dimensions of the magnet and Figure 3-17 shows the assembled drawing of the insert and CDS with the demagnetization

and experimental field profiles. The field-current ratio for the 8 tesla and 2 tesla magnets are 1026.9 G/A and 311 G/A, respectively. A Model 420 programmer in conjunction with a magnet power supply (4Q5100PS) controls the current in the magnet.

3.11 Thermometry

A ^{3}He melting curve thermometer is used as the primary thermometer for all low temperature measurements. Apart from this, the fridge is equipped with resistance thermometers at different locations on the dilution unit. The mixing chamber and the 1K pot have ruthenium oxide resistance sensors as thermometers while the sorb has an Allen Bradley resistor. All the resistance thermometers are monitored through IGH.

3.11.1 Melting Curve Thermometer

There are two melting curve thermometers (MCTs) of a similar design, one on top of the nuclear stage (Figure 3-18(b)) and the other directly mounted on the cell heat exchanger (Figure 3-18(a)) located in the field compensated region between the demagnetization stage and the experimental space. They are Stray-Adams type cylindrical capacitive strain gauges [51, 52]. The changes in the melting pressure of the ^{3}He volume are detected by the changes in the capacitance between a movable electrode attached to a flexible diaphragm and a fixed parallel electrode. The flexible cylindrical diaphragms of the MCTs were made out of coin silver with thicknesses 0.0025" (MCT (a)) and 0.0032"(MCT (b)) and epoxied with Stycast 2850FT to the rest of the body formed out of silver. The diaphragm thickness has been chosen such that at the highest applied pressure the maximum stress is about a factor of 5 below the yield stress. The bottom part of the MCT (a) has been annealed and the outside of its base in thermal contact with the main exchanger is gold plated. MCTs (a) and (b) have silver heat exchangers with surface areas $\approx 1.7\ m^2$ and $\approx 2\ m^2$, respectively and consist of 8 silver posts anchored to the base to ensure good thermal contact between the silver sinter and the base. The ^{3}He open volumes for the MCT's (a) and (b) are 0.11 cm^3 and 0.2 cm^3 respectively. A capacitance bridge technique has been implemented as the detection method for the unknown capacitance of

MCT (a) on the cell by comparing it with a reference capacitor, whereas the capacitance of MCT (b) is measured using an Andeen-Hagerling commercial bridge with built-in reference. For the homemade bridge, a silver mica capacitor (with a capacitance of 30 pF) was chosen as the reference and has been mounted within a copper encloser on the 1K plate of the cryostat where we have high stability in temperature. Figure 3-19 shows the schematic of the bridge circuit. The bridge is excited with a 1 kHz, $1V_{p-p}$ signal from a function generator (Wavetek model 182A) which has been isolated from the ground by a Gertsch (1:1) transformer (ST-200AM). In this three terminal measurement, the off-balance voltage is detected by an SR530 lock-in amplifier from a common coaxial line wired to one leg of the reference capacitor and one of the MCT capacitor plates. The bridge balance has been completely automated through PCI-GPIB, interfaced with the precision ratio transformer (Tegam model 73) and the lock-in amplifier. Automation has two advantages: first, the capacitance bridge self-balances without the intervention of an operator and the temperature is measured in real time with the calibration built into the program. Second, since every measurement is performed at or near the balance point, errors arising from the possible non-linearity of the circuit and gain drift in amplifiers is minimized. The algorithm consists of the following steps:

1. Initialize the ratio transformer and the lock-in for balance and set a threshold voltage window, $\pm V_{th}(\ 10^{-6}\ V)$ for a fixed sensitivity ($50\ \mu V$) and time constant $\tau_c (= 10\ s)$ of the lock-in and record the initial ratio change δD required to balance the bridge.

2. If the initial voltage of the lock-in, $V_o \gtrless \pm V_{th}$ for the current ratio D_o, then set a ratio $D_i = D_o \mp \delta D$. Else, go to step 4.

3. Wait 3 s, while averaging the lock-in voltage (5 values), V_{avg} at $\tau_c = 3\ s$. Calculate the slope, $S = \frac{\delta D}{\delta V} = \frac{\delta D}{V_{avg} - V_o}$. Create an averaged array for $S = S_{avg}$ including previous consecutive measurements.

4. Set the new ratio $D_n = D_i - (S_{avg} \times V_{avg})$ at a proper settling time (3 s) and $\tau_c = 1$ s.

5. Calculate the final ratio $D_f = D_n - S_{avg} \times V_c$, where V_c is the current lock-in voltage.

6. Convert D_f into pressure using the calibration curve of the MCT and get the present temperature value based on the Greywall [53] or Florida [54] temperature scales.

For the completion of the above steps accurately, the program requires at least 20-30 s to acquire a single data point. The calibration of the MCT is performed at 1K. The pressure is measured at the room temperature from a high precision absolute pressure gauge (Quartzonix pressure standard model 970) from Pressure Systems, Inc. The MCT is exercised by slowly pressurizing and depressurizing ($\approx$ 0.5 psi/s) between 400 to 500 psi at least 4-5 times. Afterwards, 35 to 40 data points (about 20 on pressurization and 20 on depressurization) are taken in that pressure range while giving about 5 to 10 minutes time for the MCT to equilibrate at each pressure before recording the ratio at the null condition. A functional relationship between the pressure and the ratio is acquired by a 2^{nd} order polynomial fit to the pressure vs. ratio data plot. There is of course a pressure difference between the room temperature pressure gauge and the low temperature MCT because of the weight of the gas columns in the connecting fill-lines. This hydro static pressure head correction is estimated to be $\approx$ 1.4 kpa (0.2 psi) for the MCT located at the bottom of the nuclear stage. In calculating this pressure, the height of the gas and its density at the different temperatures (295 K, 4.2 K and 1.2 K) is considered (see for example, [55]). In any case, the final temperature down to 0.93 mK is determined by the Greywall [53] scale after correcting the pressure offset in the calibration with the Neel transition point. The temperatures below 0.93 mk and down to 0.5 mK are determined using the scale given by Ni [54] *et al.*

3.12 Performance of the Nuclear Stage

The first demagnetization on copper was performed with just the melting curve thermometer attached to it, which also enabled us to observe the superfluid transitions in liquid ^{3}He along the melting pressure. The copper was magnetized to a 7 tesla field (@10 mA/s) and allowed to precool in the cooling power of the dilution refrigerator by closing the indium heat switch. Due to the heat of magnetization, the nuclear stage warmed from

5.2 mK to about 43 mK. Figure 3-20 compares typical precooling curves for different lengths of time in different magnetic fields and with and without the experimental cell. After 4 days of precooling in a field of 7 tesla, the fridge cooled to 10 mK (shown in solid circles). The longest precool performed so far, for a period of 7 days as shown in empty circles in the Figure cooled the copper stage down to about 8 mK. The data in triangles and solid black line represent the precooling time with the heat exchanger and a plastic experimental cell attached to the bottom of the nuclear stage in fields of 7 tesla and the maximum attainable 8 tesla respectively. The experimental cell contained 29 bar pressure of liquid ^{3}He and transverse acoustic impedance measurements were being performed by exciting a quartz transducer. The cell did not impose unwanted heat to the dilution cooling power and the precooling times are all comparable. The (precooling) time t required for the nuclear stage to reach a final temperature T, depends on the cooling power of the dilution fridge, the thermal conductance of the indium heat switch between the dilution and the CDS, and the field profile of the demagnetization magnet given by [56]:

$$t = (\frac{1}{a} + \frac{2}{k})\frac{NH^2}{T_o^2}(\frac{1}{2T_o}\ln\frac{T+T_o}{T-T_o} - \frac{1}{T}) \tag{3–2}$$

where a and $T_o = \sqrt{\frac{b}{a}}$ were the constants determined from the cooling power measurements of the dilution refrigerator:

$$\dot{Q} = aT_m^2 - b \tag{3–3}$$

k was the prefactor in the temperature dependant thermal conductance, $\kappa = kT$ and NH^2 was the field dependant factor occurring in the heat capacity of the nuclear stage (equation 3–5). The solid red line in the Figure 3-20 was the fit to the pre-cooling data using the measured values of a, b and N in equation 3–2. The only fitting parameter was the conductance constant k. a and b were determined from 3–3, while N was determined from the heat leak measurements discussed in the next section. The experimental data were in excellent agreement with the theoretical equation. With the parameter extracted

from the fit, thermal conductance of the indium heat switch turns out to be $\approx$ 19.3 T mW/K^2. After precooling, the heat switch was turned off and the magnetic field reduced at a slow rate. As the field was removed adiabatically, the temperature lowered to maintain constant entropy. This is shown in Figure 3-21. The inset shows the field versus temperature plot. We had a constant H/T ratio of about 700 T/K. Demagnetization progressed at a fast rate of 142 G/min for a period of about 6 hours in the beginning and paused for an hour to allow the CDS to reach equilibrium with the thermometer. Afterwards, field was reduced at a slower rate of 80 G/min for about 4 hours and the superfluid transitions were observed in the MCT as displayed in the chart recorder trace in Figure 3-22. The solid ordering (Neel transition) temperature of 0.93 mK was reached in demagnetizing field of 6 kG. Temperature was measured down to 500 μK. The lowest temperature reached was estimated to be $\approx$ 200 μK, assuming constant entropy reduction.

Heat leak measurements were conducted on the copper cooling stage after demagnetization to a low temperature ($<$ 1 mK). Since the nuclear stage is thermally isolated, any change in its temperature would be due to the ambient heat leak ($\dot{Q}$). In order to determine this heat leak, we employed a differential heat leak method. A known amount of power ($\dot{Q}_{app}$) was applied by a heater connected to the nuclear stage for a certain interval of time (typically for 6 hours) which was much larger than the thermal relaxation time and the temperature of the stage was continuously monitored with time. The slope of T vs. t was related to the heat capacity of the nuclear stage C_{NS} by,

$$\dot{Q} + \dot{Q}_{app} = C_{NS}\frac{dT}{dt} \tag{3–4}$$

where C_{NS} was dependent on the demagnetization field H as,

$$C_{NS} = N(\frac{H}{T})^2 \tag{3–5}$$

The constant $N = n\frac{\lambda_n}{\mu_o}$ with n being the number of moles of copper and λ_n, the nuclear curie constant. For copper [48], $\frac{\lambda_n}{\mu_o} = 3.22\ \mu JK/T^2mol$. The temperature of the nuclear

stage as a function of time was measured by the melting curve thermometer. Assuming a constant heat capacity at a given magnetic field and using the measured slopes $\frac{dT}{dt}$ for different applied powers, the heat leak ($\dot{Q}$) and heat capacity prefactor N were calculated by solving equation 3–4. These measurements were performed at various magnetic fields and a magnetic field dependance of the heat leak was observed as shown in Figure 3-23. The approximately linear dependance on the square of the magnetic field implies eddy current heating. Extrapolating to zero field, we found a minimum heat leak of 4.8 nW. Figure 3-24 shows the calculated N value as a function of the heat leak at different magnetic fields. The constant N, averaged for all the measurements was 0.09 JmK/T^2. The effective number of moles of copper was 28.

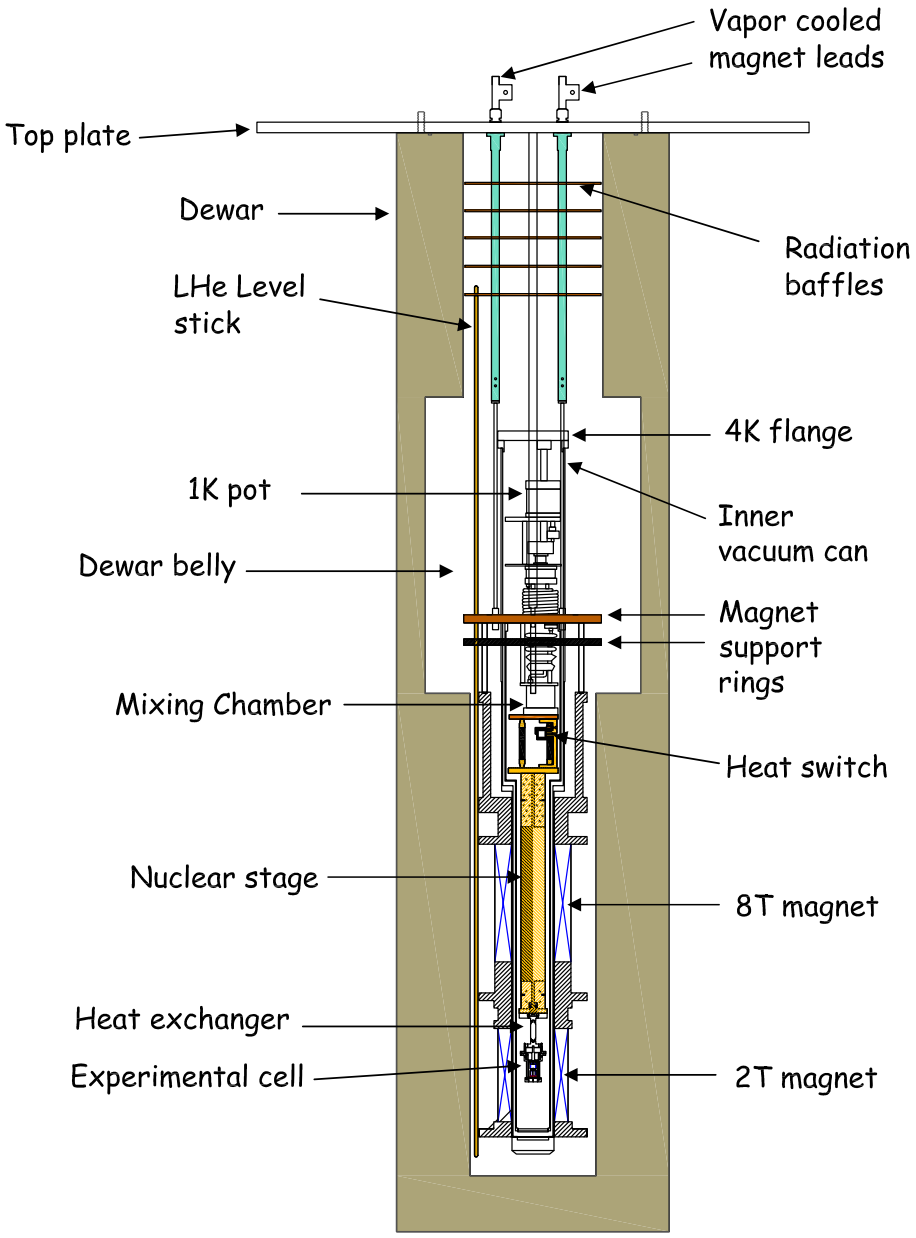

Figure 3-1. A Drawing of the cryostat assembled with all its inner components.

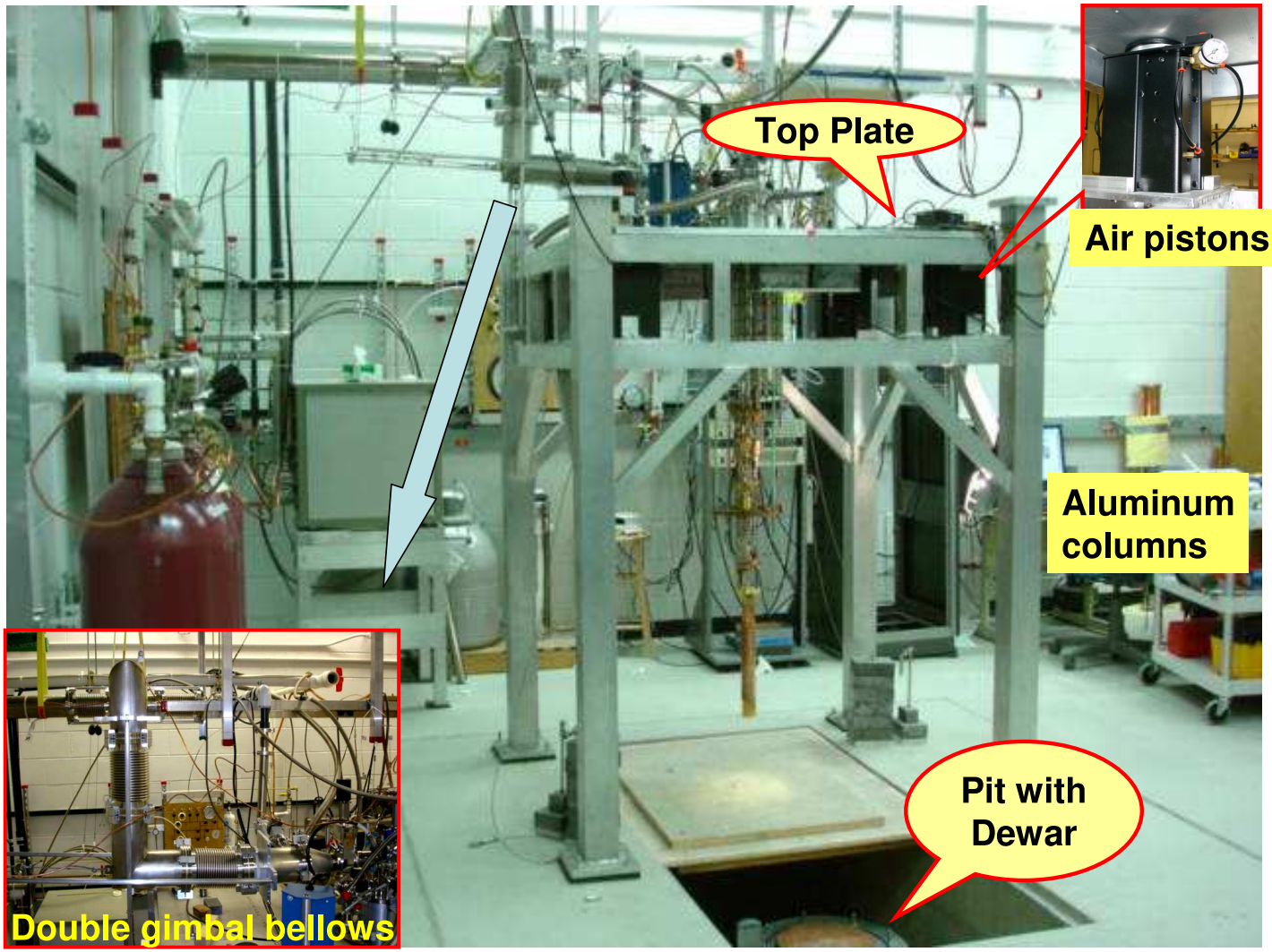

Figure 3-2. Overview of "Thule" cryostat structure.

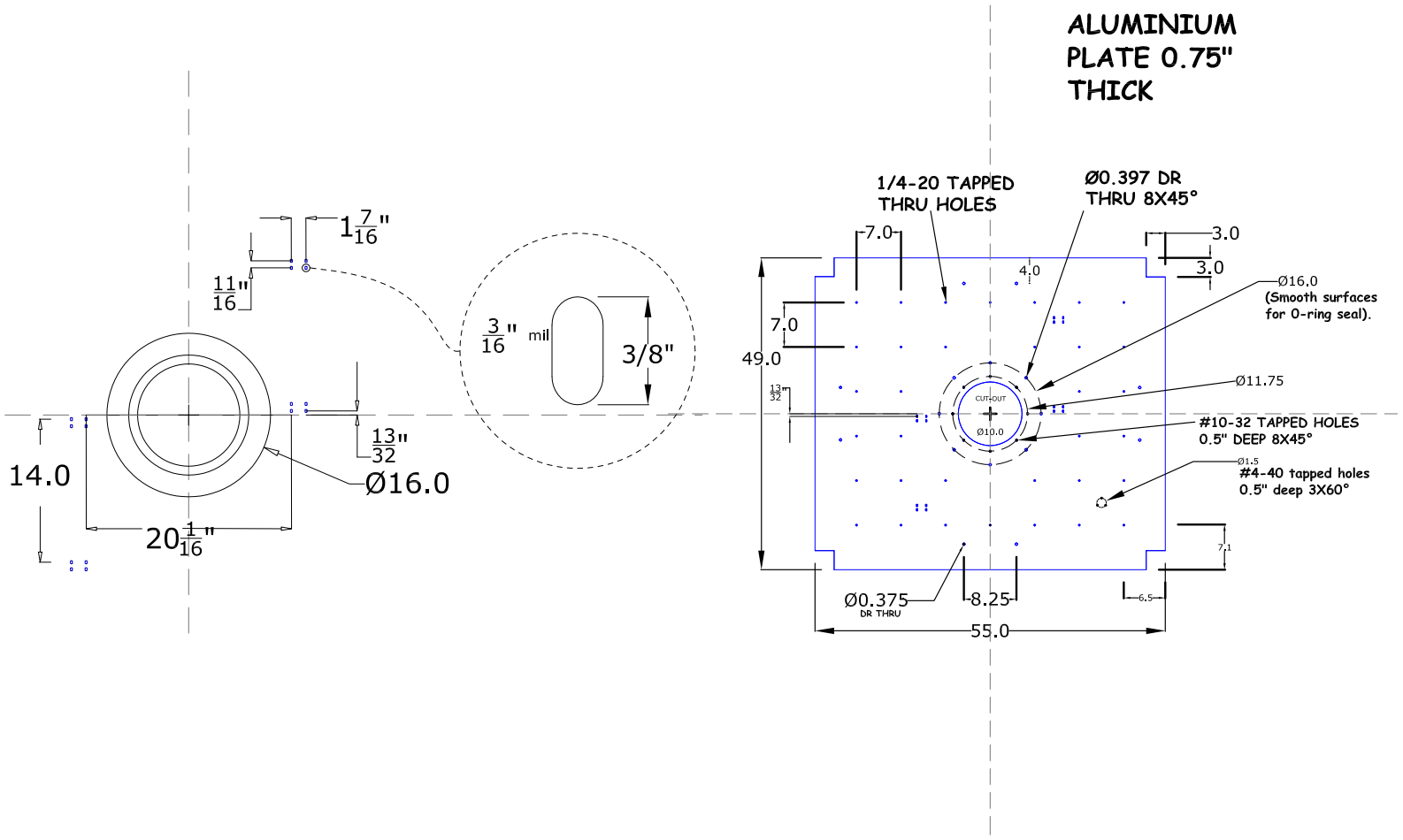

Figure 3-3. The aluminum plate viewed from the top. The blow up on the left shows the dimension of the pulleys relative to the center.

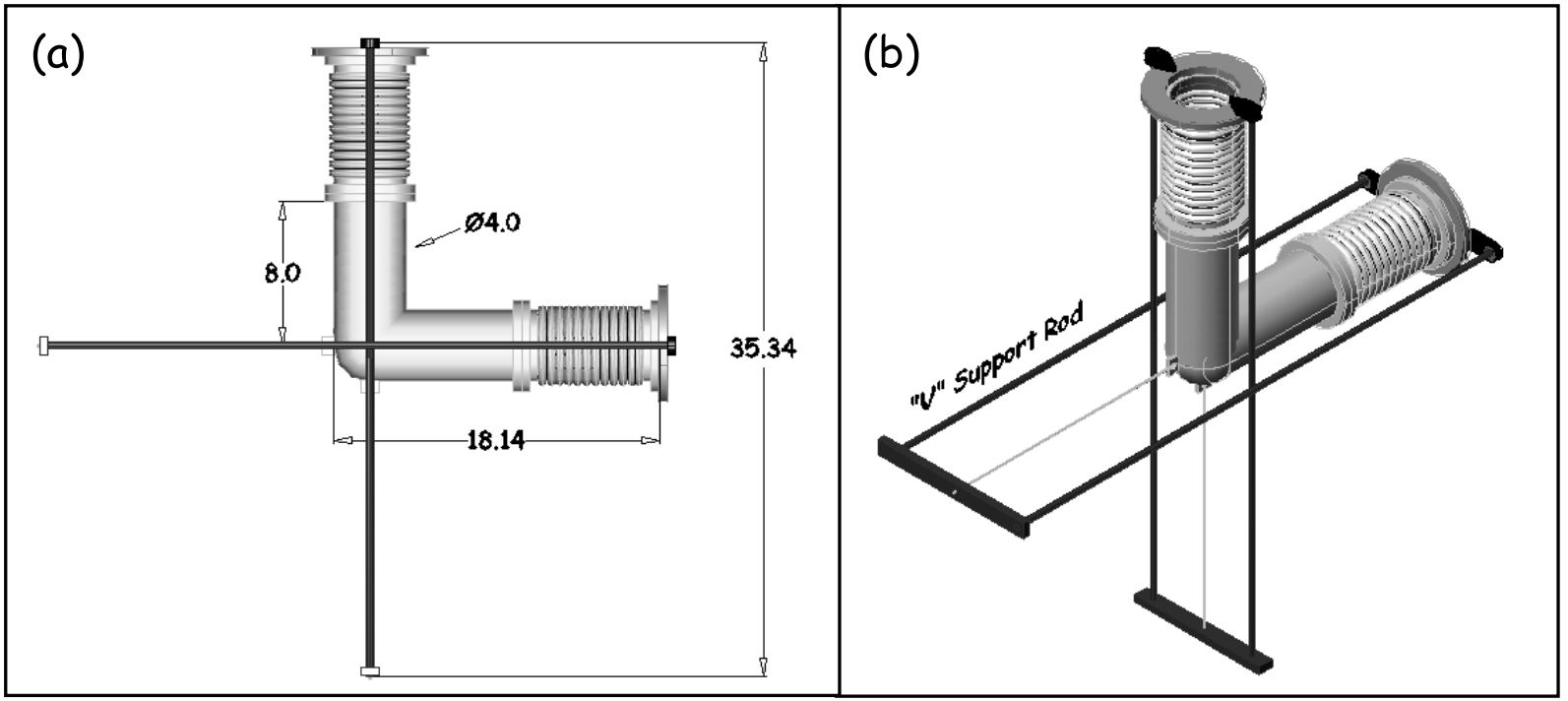

Figure 3-4. Design of the double gimbal bellows structure. (a) Front view showing important dimensions and (b) 3D view showing a clearer view of the 'U'-support rods.

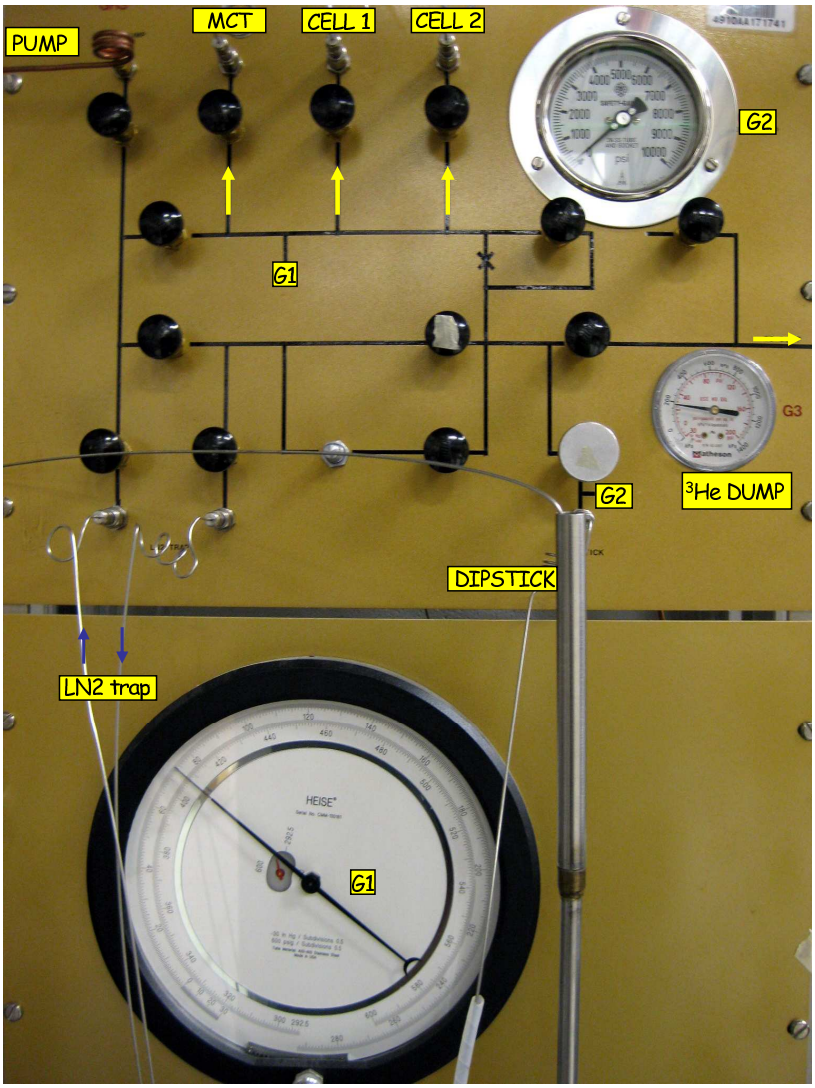

Figure 3-5. ^{3}He high pressure gas handling system. Pressure is monitored at G1 with a Heise bourdon gauge. A high accuracy quartz pressure transducer gauge is also connected at G1 from behind the panel.

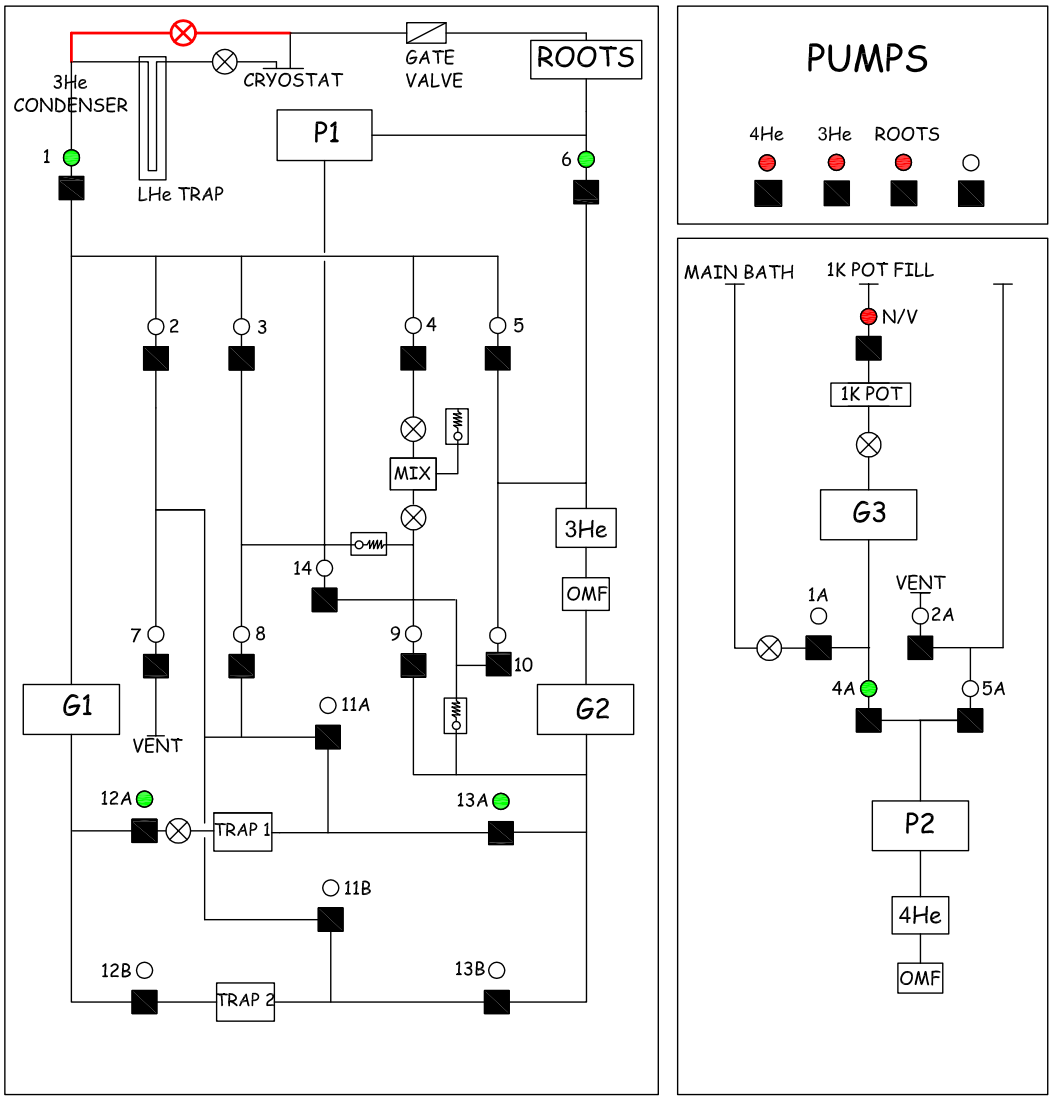

Figure 3-6. Dilution refrigerator intelligent gas handling system (IGH) provided by Oxford. P1, P2, P3 are low pressure pirani gauges. G1, G2 and G3 are high pressure (>50 mbar) gauges. The 1K pot needle valve, valve 6 and valve 12 are solenoid valves that open incrementally from 0 to 100%. Manually installed valves are marked by a cross. The red line and red cross indicate the by-pass line and valve, respectively.

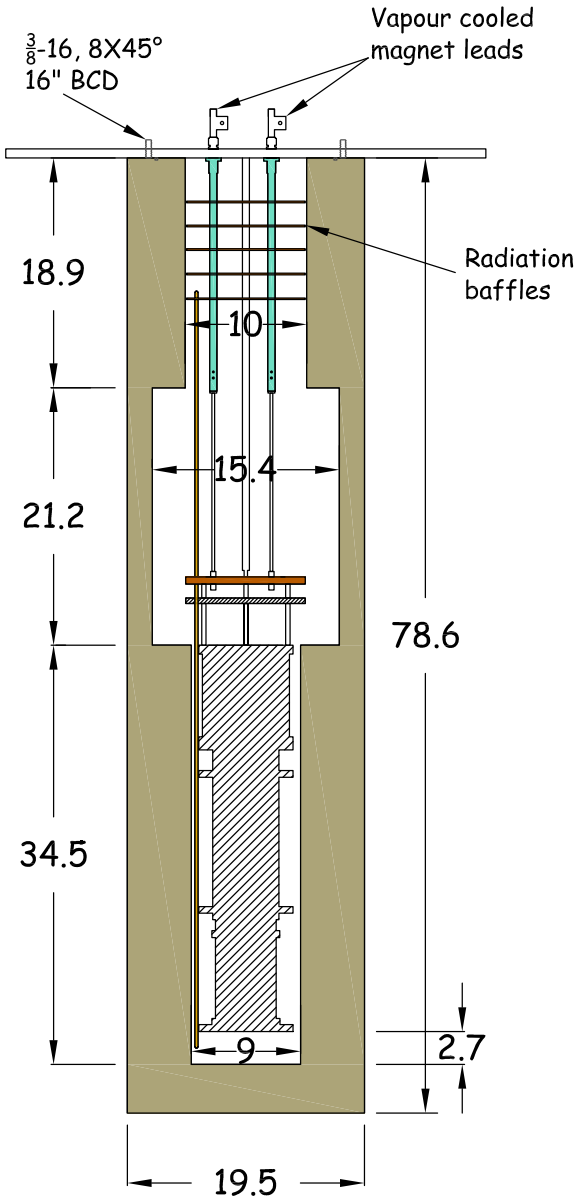

Figure 3-7. Dimensions of the vapor cooled dewar.

Table 3-1. Oxford coaxes labeled from 1 to 12 on the top plate of the cryostat.

Label no.	Assigned to
1	common line for MCT (a) on the cell and reference capacitor on 1K plate
2	experimental spare at the bottom of the CDS with MMCX female connector
3	experimental spare at the bottom of the CDS without a connector
4	MCT (b) on top plate of the CDS
5	experimental spare at the bottom of the CDS without a connector
6	experimental spare as #6 on the CDS top plate with MMCX female connector
7	MCT (b) on the top plate of CDS
8	connected to the reference capacitor on the 1K plate
9	experimental spare as #7 on the CDS top plate with MMCX female connector
10	experimental spare at the bottom of the CDS without a connector
11	MCT (a) on the experimental cell
12	experimental spare as #4 on the CDS top plate with MMCX female connector

Table 3-2. Resistance values of resistors in the bath.

Label	300K (Ω)	77K (Ω)	4K (kΩ)
R1	638	933	22.55
R2	710	1010	22.67
R3	785	1095	23.61

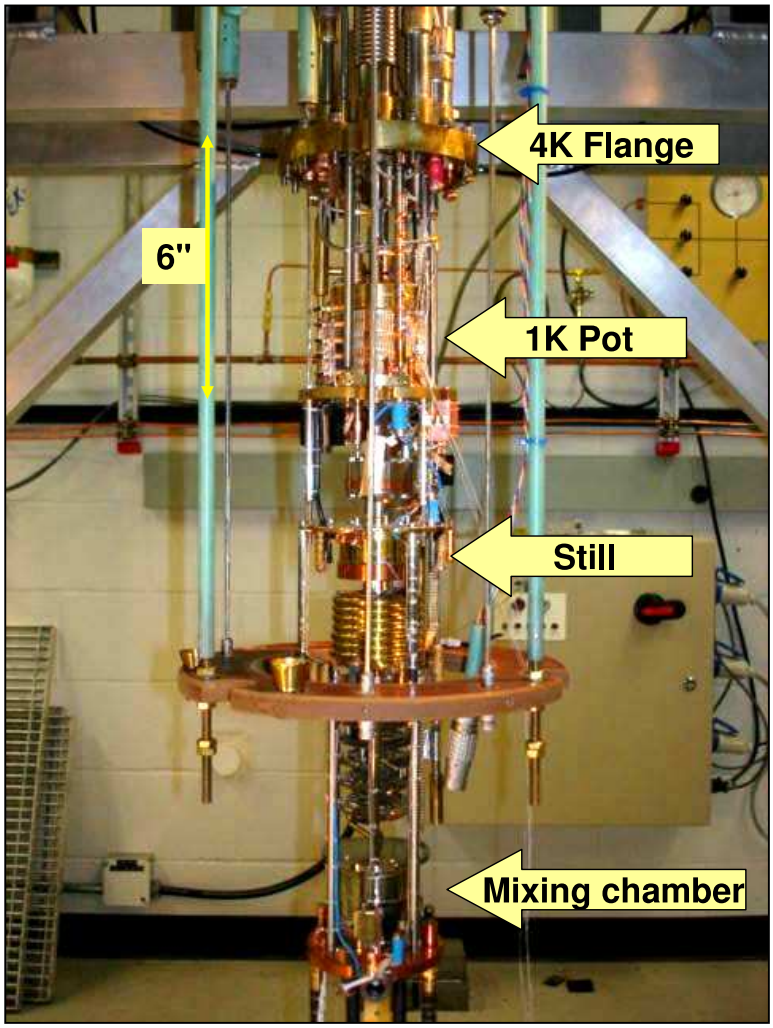

Figure 3-8. Picture of the Kelvinox 400 dilution refrigerator.

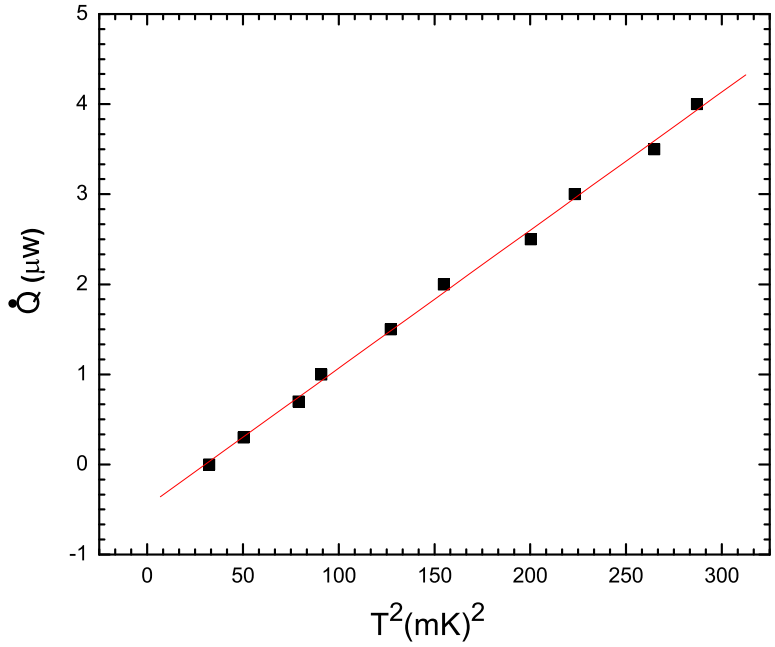

Figure 3-9. Measured heat leak vs. the square of the mixing chamber temperature of the dilution fridge. Red line is a linear fit to the data

Table 3-3. Electrical wiring assignment for the Belden cable between the cryostat (Letter pins) and the measurement box (pin no.) on the rack.

Letter Pin	Pin (no.)	Cryo 8T connector	Cryo 2T connector
A	1	LHe level meter(I+)	LHe level meter(I+)
B	2	LHe level meter(I-)	LHe level meter(I-)
C	3	LHe level meter(V-)	LHe level meter(V-)
D	4	LHe level meter(V+)	LHe level meter(V+)
E	5	Bath resistor R1	Spare
F	6	Bath resistor R1	Spare
G	7	Bath resistor R2	Nuclear stage heater (+)
H	8	Bath resistor R2	Nuclear stage heater (-)
J	9	Persistent switch heater	Persistent switch heater
K	10	Persistent switch heater	Persistent switch heater
L	11	Magnet voltage tap	Magnet voltage tap
M	12	Magnet voltage tap	Magnet voltage tap
N	13	Bath resistor R3	Heat switch solenoid (+)
P	14	Bath resistor R3	Heat switch solenoid (-)
R	15	Bath heater	Spare
S	16	Bath heater	Spare

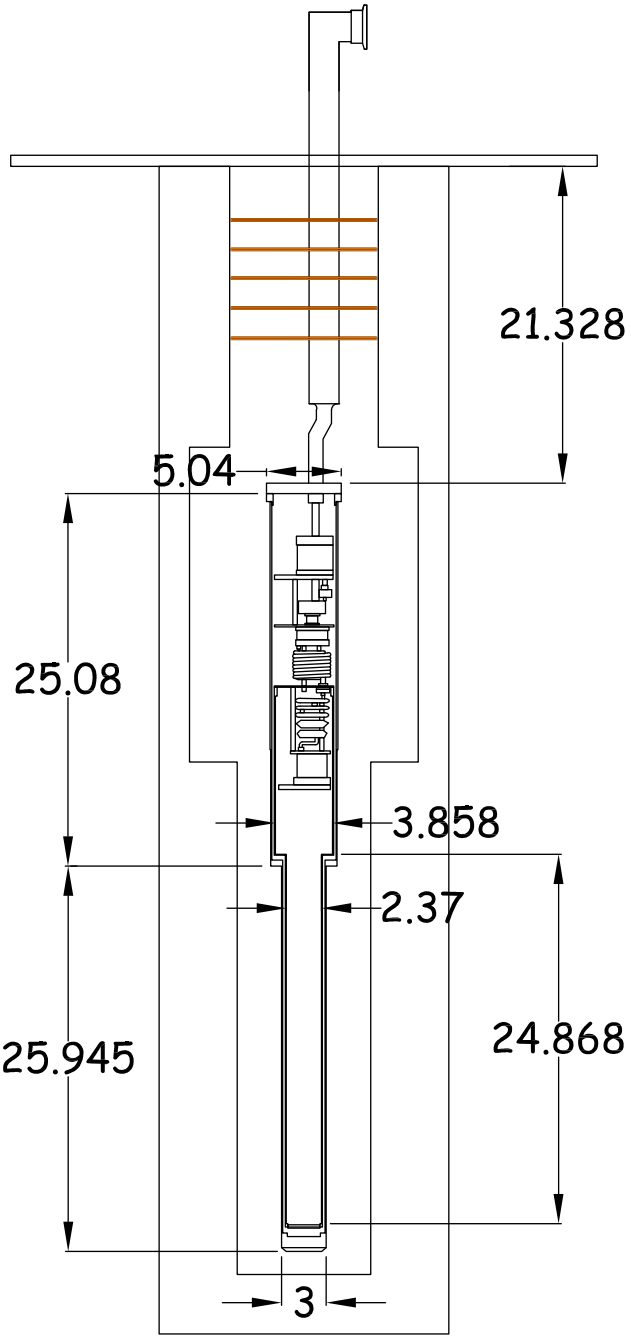

Figure 3-10. Dimensions of the vacuum can and the radiation shield assembled with the insert. Dotted line shows the dewar outline.

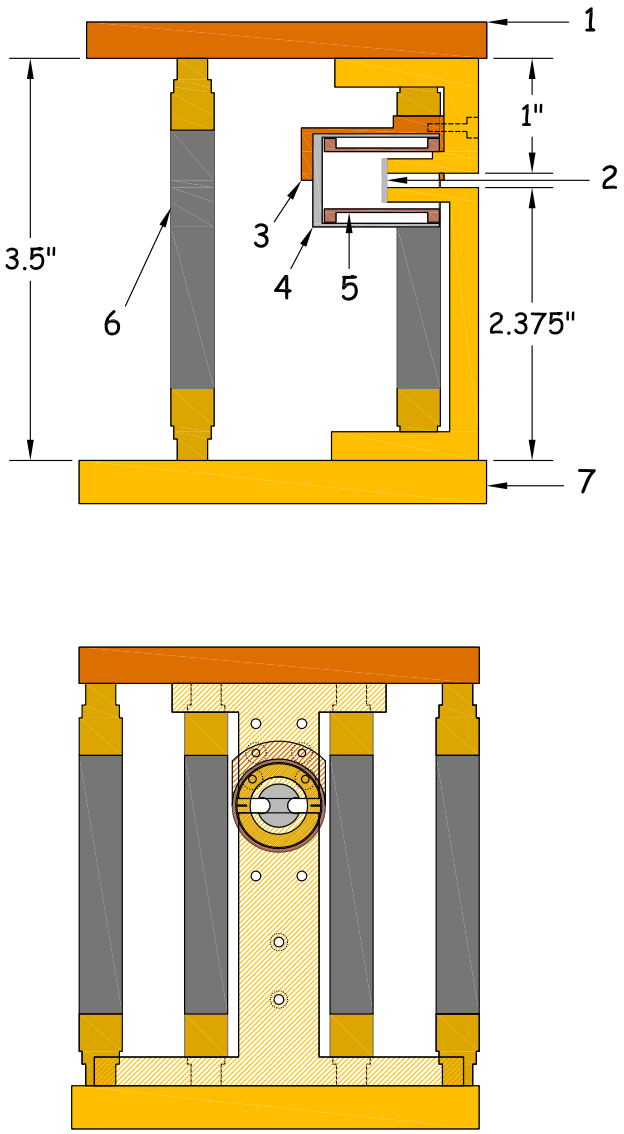

Figure 3-11. Heat switch design. Side view in top figure: 1) mixing chamber plate, 2) Indium strip 3) Copper heat sink 4) Nb shield 5) Solenoid coil 6) Vespel support rod 7) Top plate of the nuclear stage. The bottom drawing shows the front view of the switch

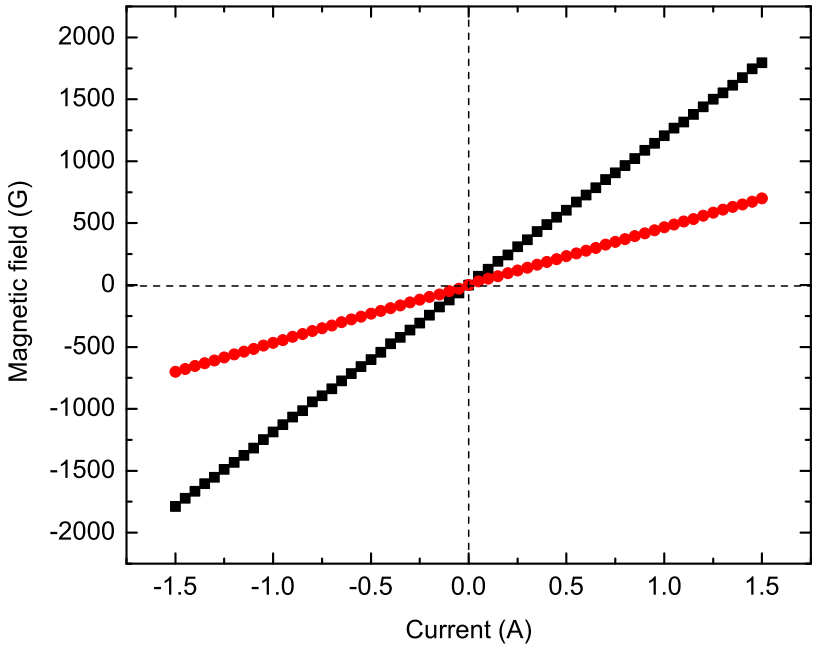

Figure 3-12. Magnetic field generated by the home made coil as a function of the applied current at 4.2 K. The red circles are with the Nb shield and the black squares are with the shield removed.

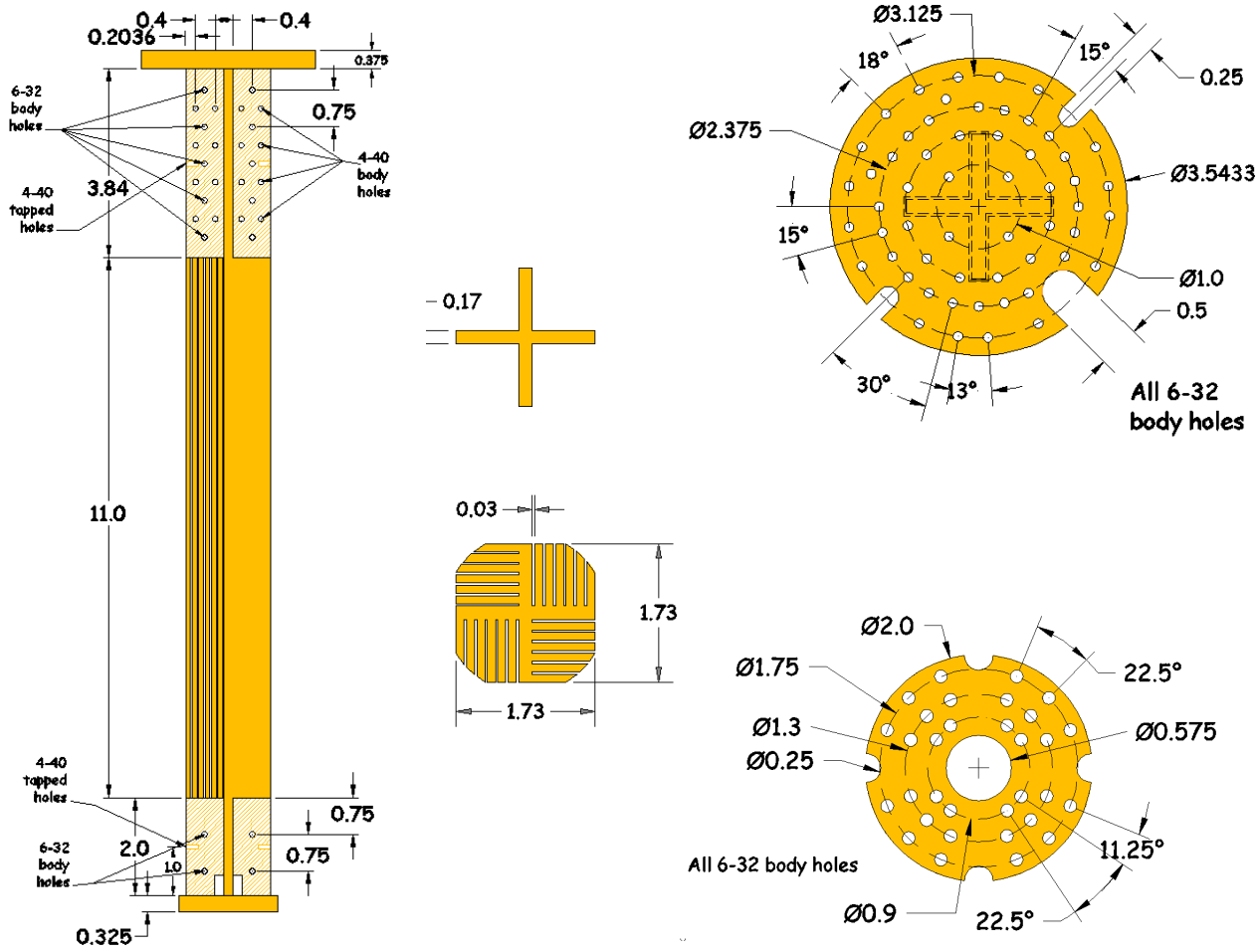

Figure 3-13. Dimension of the Copper demagnetization stage (CDS). The figures on the right hand side show the top views of the CDS at various cross-sections along the axis of the stage.

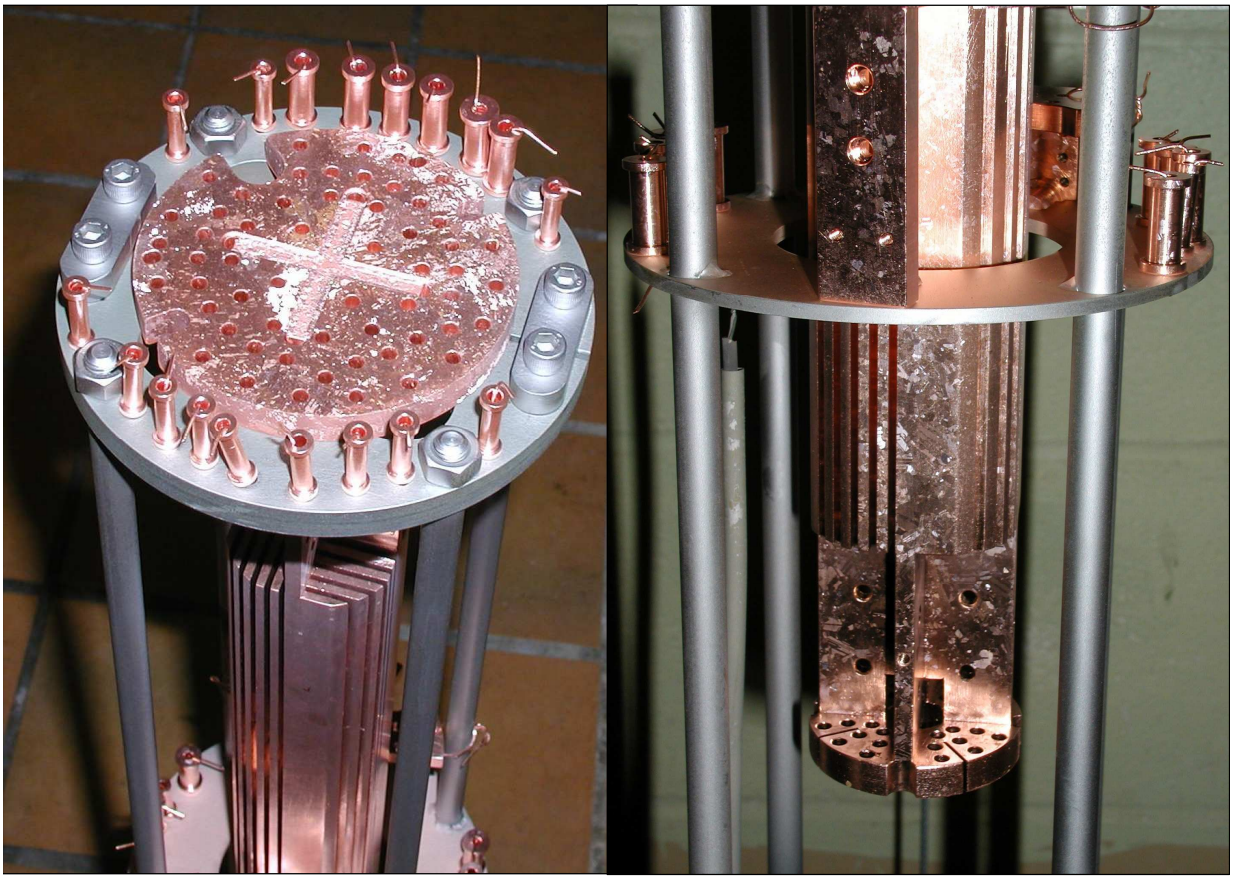

Figure 3-14. The annealed copper nuclear stage supported from the grayed stainless steel structure. On the left is the top view and on the right is the bottom view.

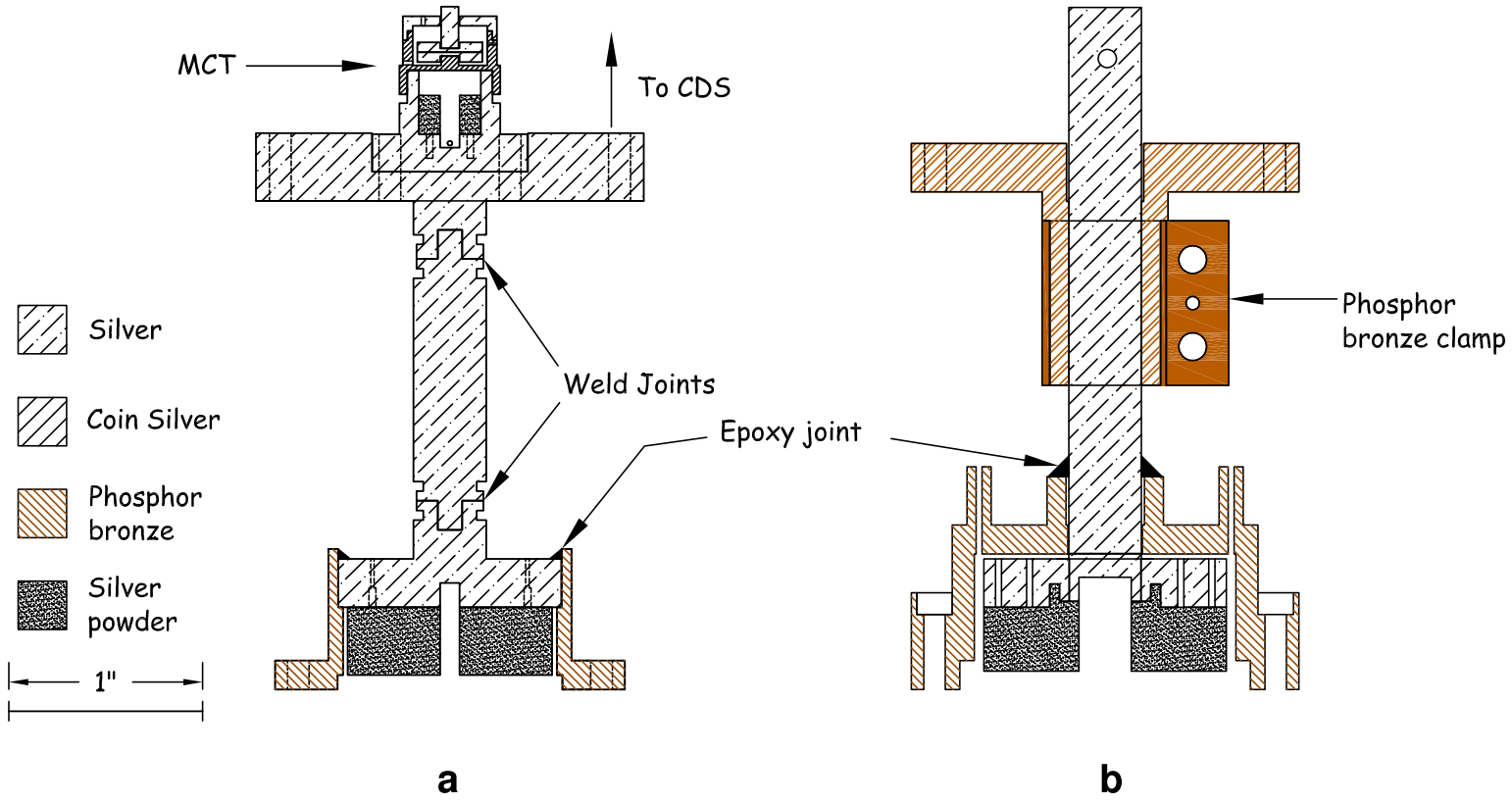

Figure 3-15. Two designs of the heat exchangers used to cool the liquid ^{3}He. a) The newer exchanger has a melting curve thermometer attached to it at the top and excludes the phosphor bronze clamp used in b) a previous heat exchanger.

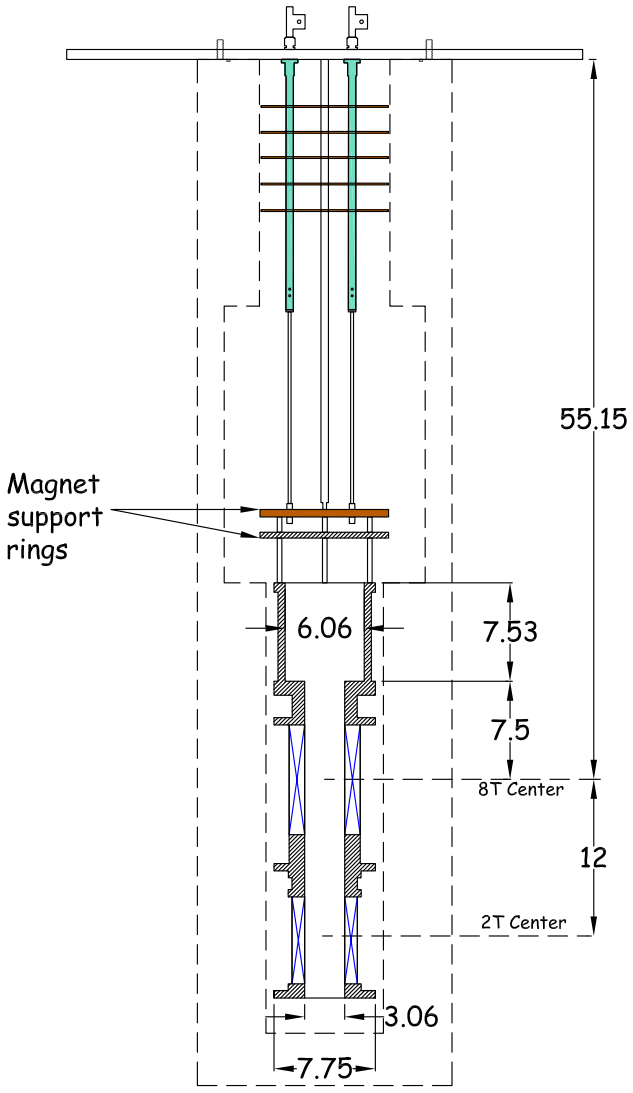

Figure 3-16. Magnet dimensions relative to the dewar.

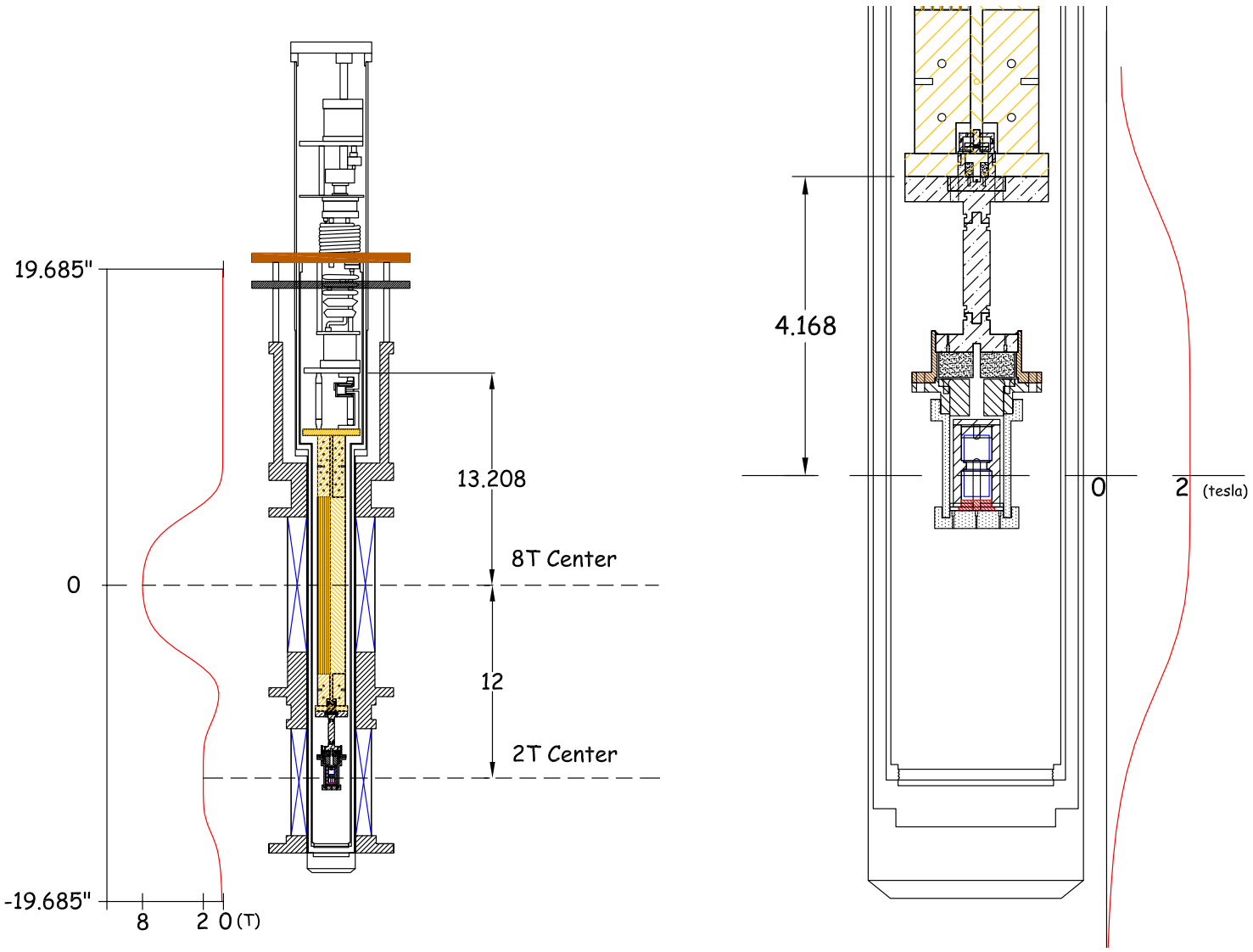

Figure 3-17. Magnetic field profile of the demagnetization magnet on the left and the experimental magnet on the right.

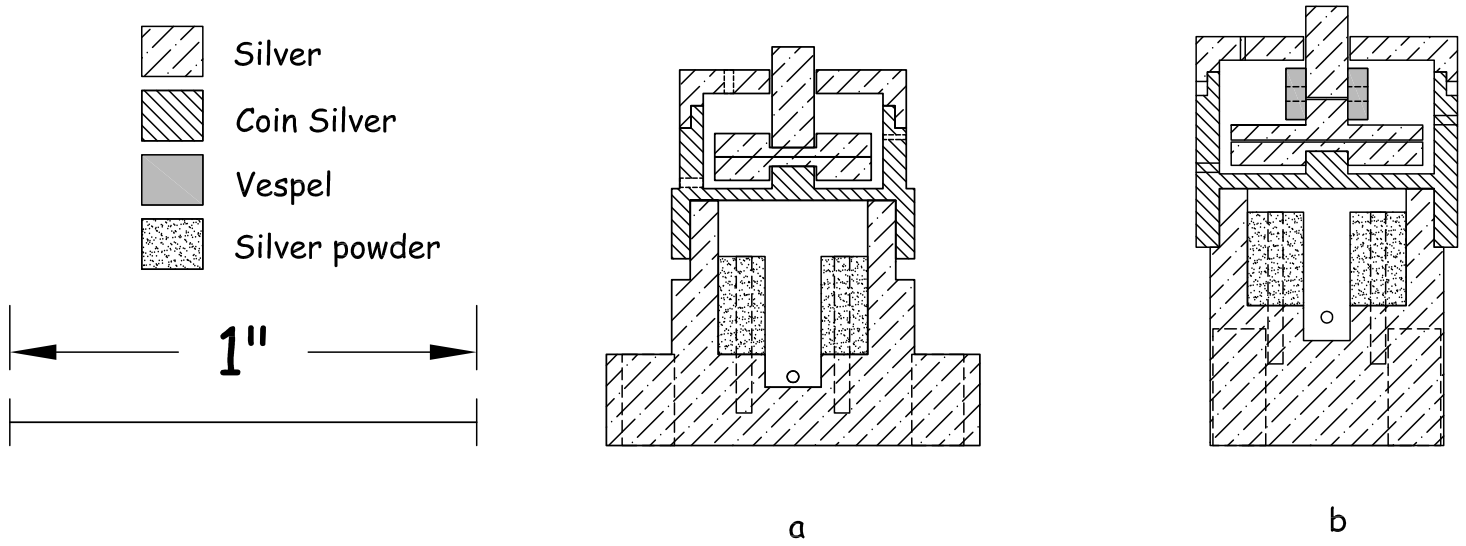

Figure 3-18. Design of the two melting curve thermometers. The new MPT, a) is attached to the experimental cell at the bottom of the nuclear stage and the older MPT, b) is mounted on the top plate of the copper nuclear stage.

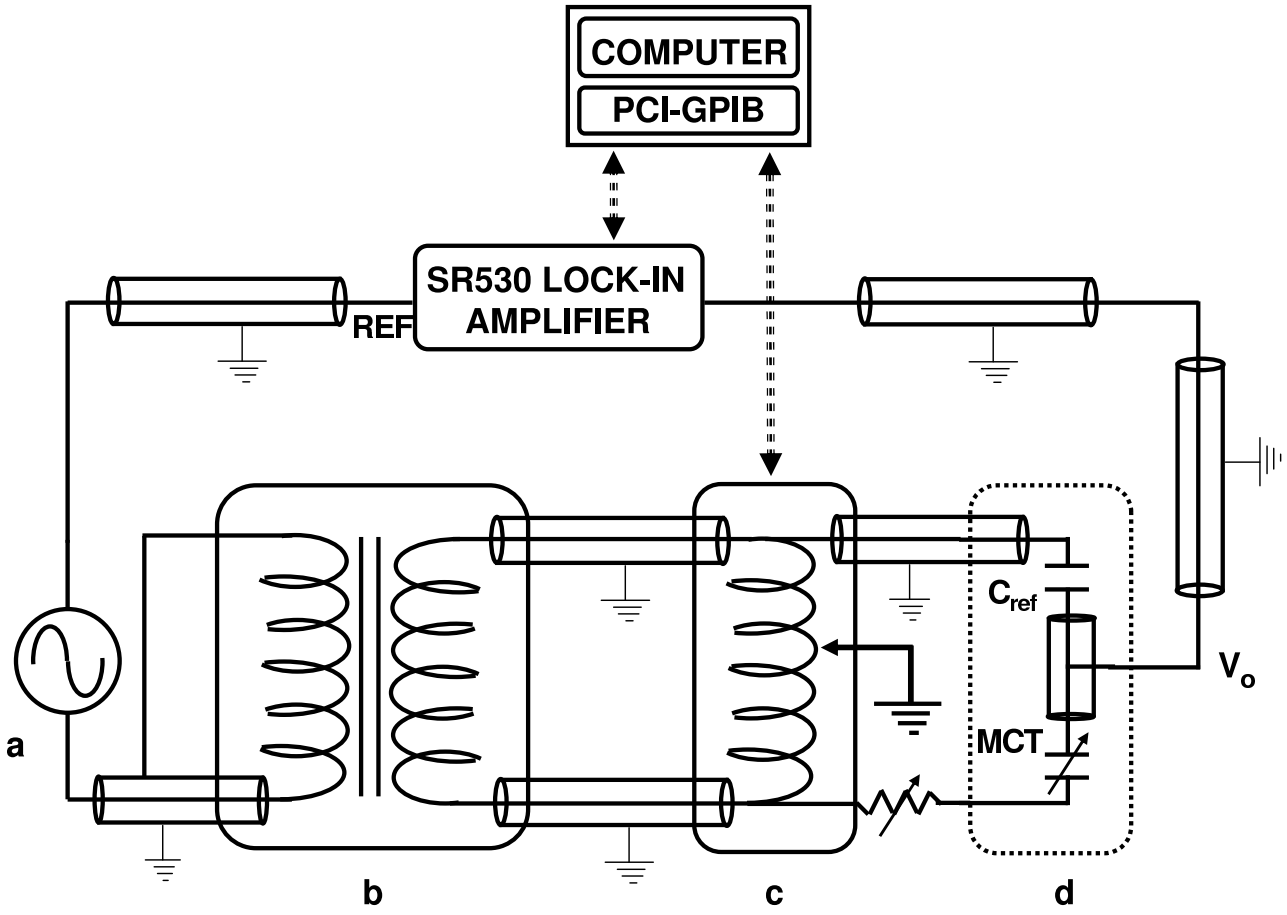

Figure 3-19. Capacitance bridge circuit diagram for the MCT. a) Signal generator, b) Isolation transformer, c) Ratio transformer d) Reference capacitor and MPT capacitor. Dotted line indicates the parts located inside the cryostat and double ended arrows show the GPIB interface to the computer.

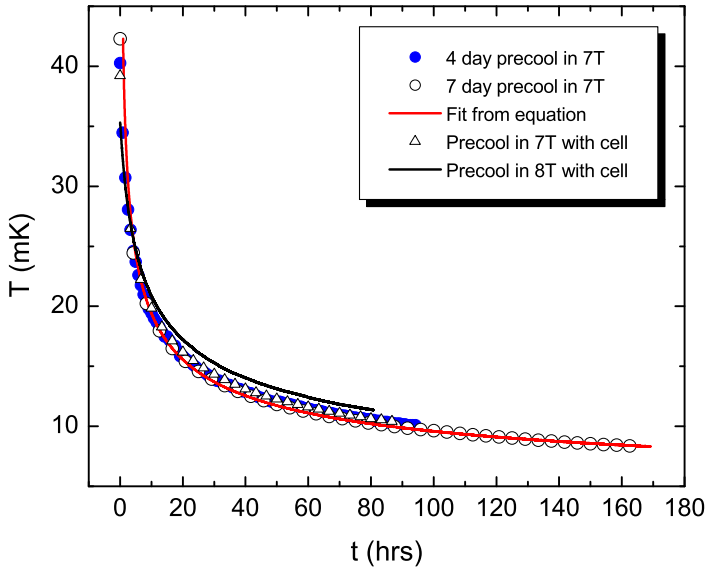

Figure 3-20. Precooling curves on different cooldowns. Precooling time without a ^{3}He experimental cell (solid and empty circles) and with an experimental cell (triangles) in a field of 7 tesla. Black line is a precool in 8 tesla while the red line is a fit to the data according to equation 3–2.

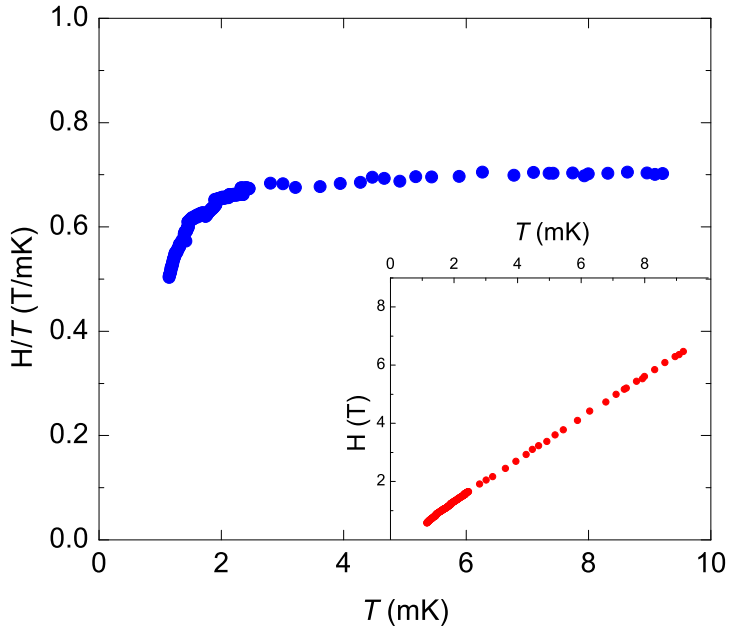

Figure 3-21. Plot of H/T vs. T during adiabatic demagnetization. Inset shows the linear plot of H vs. T.

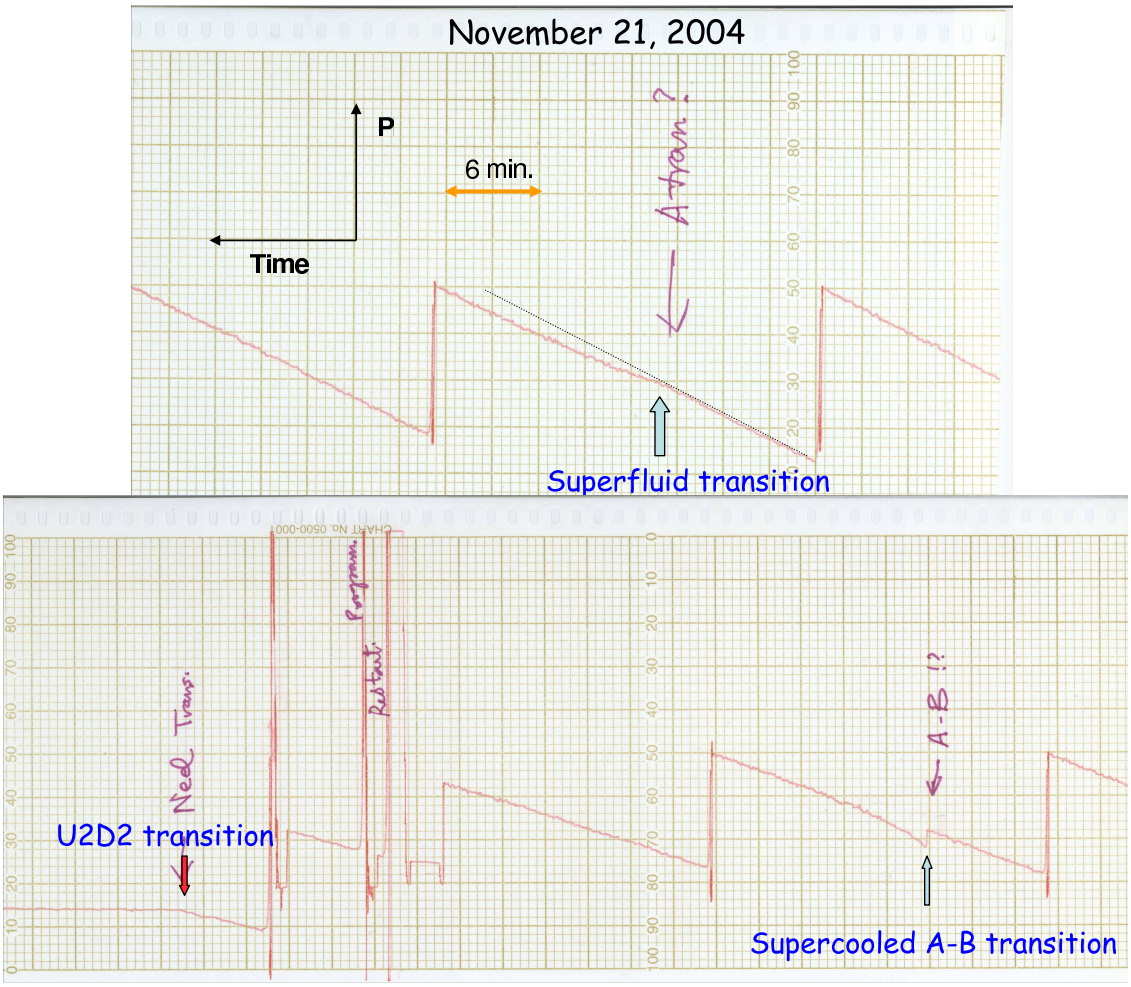

Figure 3-22. Chart recorder traces of MCT during the very first demagnetization. The y axis denotes the MCT pressure and the x-axis is the time increasing from the right to the left. The top trace show the superfluid transition and the bottom trace shows the supercooled A-B transition and the solid ordering transition along the melting curve.

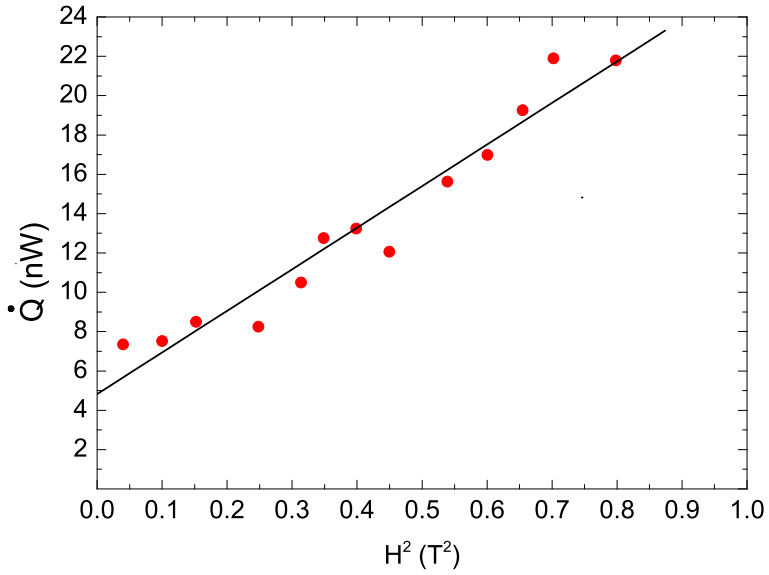

Figure 3-23. Magnetic field dependance of the heat leak to the CDS.

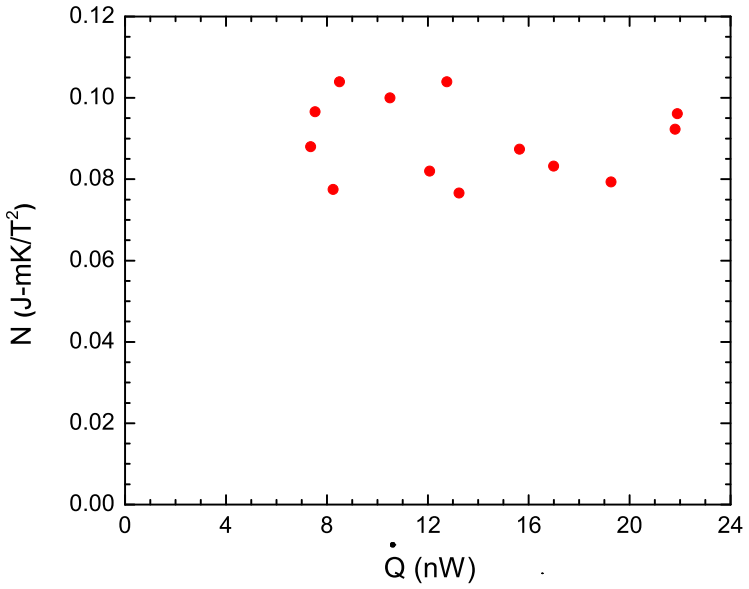

Figure 3-24. Nuclear heat capacity of the CDS derived form the heat leak measurements. N is the constant prefactor of the heat capacity of the nuclear stage in equation 3–5. It has a constant value of 0.09 J-mK/T^2 averaged over 13 measurements of heat leak measured at different magnetic fields.

CHAPTER 4
OPTICAL BIREFRINGENCE MEASUREMENTS IN AEROGEL

Before delving into the experiments on the superfluid phases of ^{3}He in anisotropic aerogel, we require a quantitative understanding of the anisotropy that can be generated from the uniaxial compression of aerogels. Optical birefringence which is a consequence of the anisotropy present in a medium has been observed in compressed aerogels [18], but detailed measurements are lacking. This chapter is a result of our optical measurements on compressed aerogels and has been reported in a separate publication [57]. The main focus is on the determination of the birefringence by measuring the transmittance of the compressed aerogels placed between two linear polarizers. The measurements were performed on aerogel samples of 98% porosity, provided by Norbert Mulders.

4.1 Principle

Examination of materials between crossed polarizers is a standard method of separating anisotropic materials from those that are isotropic. No light is transmitted through a polarizer (P) and an analyzer (A) oriented at right angles to each other with an isotropic material placed in between them. Whereas, a uniaxially anisotropic material exhibits optical birefringence and when placed between crossed P and A will have a non-zero transmittance. The light propagating through the uniaxially anisotropic medium is split into two rays with orthogonal polarizations, called as the ordinary ray (OR) and the extraordinary ray (ER). The ER and OR traverse at different velocities, parallel and perpendicular to the optic axis respectively. If the incident light is normal to the optic axis (or the compression axis), then the emerging ER and OR have a phase difference given by

$$\delta = \frac{2\pi d \Delta n}{\lambda} \tag{4–1}$$

where d is the thickness of the sample (pathlength) and λ is the wavelength of light. Δn is the birefringence of the sample defined as $n_e - n_o$, where n_e and n_o are the indices of refraction corresponding to the ER and OR respectively. Since we are dealing with the

axial compression of the aerogel, we have to account for the increase in the thickness in the transverse direction by incorporating the Poisson ratio. If d_o is the thickness and L is the length of the uncompressed aerogel, then for small deformations ΔL, the thickness of the compressed aerogel is $d = d_o(1 + \nu \Delta L/L)$, where $\nu = 0.2$ is the Poisson ratio of the 98 % porosity aerogel [58]. Figure 4-1 shows a schematic of the experimental set-up. If a beam of intensity I_o is incident on a sample placed between two linear polarizers, the transmitted intensities for crossed ($I_\perp$) and parallel ($I_\parallel$) orientations of the analyzer relative to the polarizer are given by [59],

$$I_\perp = I_o \sin^2 2\phi \sin^2 \frac{\delta}{2} \tag{4–2}$$

$$I_\parallel = I_o \sin^2 2\phi \cos^2 \frac{\delta}{2} \tag{4–3}$$

where we have neglected the absorption coefficients associated with the OR and ER directions. δ is the phase difference and ϕ is the angle between the polarization direction of the incident beam and the compression axis. In our measurements, ϕ is fixed at -45^o to the compression axis, therefore the $\sin^2 2\phi$ term is unity. Equations 4–2 and 4–3 can be solved to get the phase difference as

$$|\delta| = \begin{cases} k\pi + 2\tan^{-1}\sqrt{\frac{I_\perp}{I_\parallel}} & k = 0, 2, 4, \ldots \\ (k+1)\pi - 2\tan^{-1}\sqrt{\frac{I_\perp}{I_\parallel}} & k = 1, 3, 5, \ldots \end{cases} \tag{4–4}$$

By measuring the intensities $I_\perp$ and $I_\parallel$, we can accurately evaluate the phase difference δ and hence Δn by using Equation 4–1. Note that the above solutions only give the magnitude of Δn but not the sign. The sign has to be inferred by other considerations discussed in section 4.3.3.

4.2 Experimental Method

We adopted a technique similar to the one developed to investigate the birefringence in liquid crystals [60] and polymers [61]. Three aerogel samples with 98% porosity were used in this study, referred from here as sample 1, 2 or 3. The measurements were

performed using a Zeiss MPM800 microspectrophotometer (in Prof. Tanner's lab), equipped with a Xe lamp as the light source and a photomultiplier tube as the detector. A platform was designed for mounting the aerogel between the polarizer and analyzer of the microscope so that the light propagation direction is perpendicular to the axis of compression. The aerogel samples synthesized were cylindrical in shape. They were cut at two parallel planes using a high speed motor kit (Foredom product #1070) with a diamond disk (Pfingst Company, Inc. #H333C450) providing a flat surface to eliminate any tilt angle of the beam at the surface of aerogel. We must note here that the incident light rays had some non-parallelism when converging onto the aerogel sample due to the condensing lens (10×) used to focus the beam (see Figure 4-1). The cut and grown surfaces of aerogel were imaged using white light and a picture of those images is shown in Figure 4-2(a),(b). At the scale observed, the pictures suggest that the as grown surface of the aerogel (b) is much smoother than the machine cut aerogel (a). This could be of importance to the transverse acoustic impedance measurements of superfluid ^{3}He in aerogel where the mechanical contact between the aerogel and the transducer surfaces is crucial in observing the superfluid transition features. We have made an attempt to image the surface of the aerogel using AFM in Prof. Rinzler's group with the help of , but it proved difficult as the 98% porosity aerogel is mostly air and the AFM tip was getting stuck on the aerogel strands. The thickness (d_o) and length dimensions (L) of the cut-aerogels are shown in Table 4-1. The polarized light beam $\approx 0.5 \times 0.3$ mm, was focussed on the sample and the output light was viewed through a 10× objective lens located before the analyzer. The aerogel was compressed along the direction of the cylindrical axis. The compression was varied from $0 - 15\%$ using a micrometer vise with a non-rotating spindle. For each compression and decompression, the wavelength was scanned from $200 - 800$ nm in 4 nm increments and the output intensity of light was measured for various angles (θ) of the analyzer relative to the polarizer transmission axis

fixed at $-45°$ to the aerogel compression axis. The whole measurement process for a single sample took about 4 hrs.

4.3 Results and Discussion

4.3.1 Mechanical Properties

The compressive strain on aerogels has certain mechanical effects. Firstly, compression can lead to a reduction in the elastic modulus observed previously [58, 62] in high porosity aerogels. Secondly, shrinkage or damage can result in aerogels in other scenarios, for example, during the supercritical drying stages of the gel [18, 63, 64] or during fluid adsorption [65]. In our measurements, we observed a substantial amount of shrinkage in length of the aerogel undergoing four cycles of compression and decompression. Figure 4-3 depicts the length of the aerogel before being compressed by 15% for four consecutive cycles for the three samples. The shrinkage, maximum for the first cycle, is reduced for higher number of cycles. After four cycles, we see a substantial amount of cumulative shrinkage in length by 9%, 7.5% and 6.7% for samples 1, 2 and 3, respectively. However, no shrinkage was observed for the sample cycled up to 5%, which is in agreement with the elastic measurements of Gross [62] *et al.*, who performed three or more cycles of compression on their aerogel samples. But unlike us, they compressed only by a few percent and observed that most of their samples recovered 99.5% or better of their original length, although it has to be noted that their sample preparation method was different from ours.

4.3.2 Transmittance Measurements

Transmittance (T) is determined by the ratio I_a/I_o where, I_a is the intensity measured with the aerogel and I_o is the intensity measured without the aerogel and the two polarizers aligned parallel to each other. Figure 4-4 displays the intensity spectra measured without the sample in the spectrometer for various configurations of the set-up: a) without any polarizers, b) without the analyzer but with the polarizer c) parallel polarizers and d) crossed polarizers. Scaling out the measured intensities I_a with I_o

ensures exclusion of the background features form the optics. Since the size of the aerogel strands (3 nm) $\ll \lambda$, the wavelength of visible light, scattering of light from aerogel is weak and has been well accounted for in the literature [66] by Rayleigh scattering phenomenon. The Rayleigh scattering cross-section for a single scatterer is $\sigma \propto 1/\lambda^4$. When we have a collection of such particles in a random network, the scattering intensity passing through a material with number density ρ and thickness d is $\propto \exp(-\rho\sigma d)$ (Beer's Law). This needs to be considered in the expression for the intensity of light transmitted given in equations 4–2 and 4–3. The modified equation for transmittance in the cross-polarized set-up, $T_\perp$ is given by:

$$T_\perp = T_o \exp \frac{-r^3 d}{\lambda^4} \sin^2 \frac{\pi d \Delta n}{\lambda} \tag{4–5}$$

where the exponential term is the contribution from Rayleigh scattering, characterized by a dimension r. T_o is a wavelength independent loss related to the absorption or scattering from the surface [66, 67]. Figure 4-5 shows a plot of the transmittance of sample 1 in the crossed polarized configuration $T_\perp$ as a function of the wavelength on its fourth cycle of compression from 0 - 15%. Traces on decompression are shown in open symbols. Effect of Rayleigh scattering is exemplified by the increasing envelope of the transmittance between 300 - 800 nm and has been observed previously in similar porosity aerogels [68]. The data from 200 - 300 nm is noisy and meaningless because of absorption from glassy material in the optics, and therefore can be ignored. In the uncompressed state, we observe a small, non-zero transmittance in the cross polarized configuration over the wavelength range measured. This could be due to built-in anisotropy in the sample from the synthesis and/or damage from previous compression cycles as noted in section 4.3.1. In sample 1, as the compression is increased, $T_\perp$ first decreases and then starts to increase after 2% compression. A small amount of strain ($\approx$ 2%) seems to compensate this built-in anisotropy. Beyond 8%, $T_\perp$ starts to oscillate with maxima and minima progressing to longer wavelengths with increasing strain. The oscillations, as expected from equation 4–2,

are due to the fact that there is a phase shift of π or more involved depending on whether $I_\perp/I_\parallel$ corresponds to a maxima (odd k) or minima (even k) in the argument of the sine function (equation 4–4). The transmittance spectrum for compression-decompression cycles shows hysteresis. As seen in Figure 4-5, $T_\perp$ for 7% compression is not reproducible on 7% decompression, but is more similar to the 5% compressed trace. The hysteresis disappears when shrinkage ($\approx$ 2%) is considered in evaluating strain for this particular compression. This does not seem to work for other compression ratios and it is not yet clear why this was so, partly because data on decompression was taken only for a few strain ratios. Similar $T_\perp$ spectra are obtained for samples 2 and 3, shown in figures 4-6 and 4-7.

The panel in Figure 4-8 displays the transmittance at $\theta = 0°, 45°$ and 90° angles of the analyzer for samples 1, 2 and 3 from top to bottom, respectively. The panels on the left (a, c, e) show the transmission for the uncompressed state while the ones on the right (b, d, f) show the transmission at a maximum compression of 15%. We observe that the 15% strained samples show waveplate behavior. In the uncompressed aerogel, the linearly polarized light propagating in the medium preserves its polarization. However, when compressed by 15%, the linearly polarized light is transformed into circularly polarized light at specific wavelengths. This is demonstrated from the oscillatory behavior (in (b),(d),(f)) where the transmittance is independent of θ at specific wavelengths (node points). The condition for the first order quarter waveplate is $\lambda_{1/4} = 4d\Delta n$ while that for the half waveplate is $\lambda_{1/2} = 2d\Delta n$. For instance, sample 1 at 15% compression behaves as a quarter wave plate at wavelengths of 310 nm, 380 nm, 500 nm and 800 nm and as a half-wave plate at 350 nm and 625 nm. The node points are periodic in wave number with a period $\approx$ 6500 cm^{-1} and is depicted for sample 1 in Figure 4-12.

The birefringence entering $T_\perp$, in Equation 4–5 can vary with the wavelength and can be determined in two ways. One way is by fitting the transmission data using Equation 4–5, choosing a proper model for $\Delta n(\lambda)$. When the spectral range has no resonance

frequencies, the dispersion in the refractive index can be modeled by a simplified form of Sellmeier dispersion equation or Cauchy formula [59, 69] given by

$$\Delta n = B + \frac{C}{\lambda^2} \tag{4–6}$$

The spectrum of transmittance for our aerogel sample 1 in the UV-visible and near infrared (NIR) wavelengths taken using unpolarized light is displayed in Figure 4-13. The resonance peaks in the wavelengths between 1200 and 2000 nm and the peak above 2000 nm have been observed before [68] and are attributed to the presence of adsorbed water and a combination of O-H and Si-O fundamentals, respectively. Since all our transmittance measurements were performed between 200 - 800 nm, where there are no resonances, the Cauchy form of the dispersion can be applied [59]. The Sellmeier type of equations have been used widely to fit the birefringence dispersion in glasses and other liquid crystalline materials [61, 70, 71]. Using Equation 4–5 with 4–6, our transmittance data from the cross polarized set up was fit by a non-linear least squares fitting method, with T_o, r, B and C as the fitting parameters. We used the reported Poisson ratio [58, 65] value of 0.2 for aerogel in calculating the thickness, d at a given compression. The fit is shown in solid lines in Figure 4-14(a) along with the measured transmittance (in symbols) for the three samples. The actual values of parameters for the fit are listed in Table 4-1. Using the parameters (B, C) obtained from this fit, the dispersion in birefringence calculated from the Cauchy formula is shown as solid lines in Figure 4-14(b).

Another method of determining Δn (Equation 4–1), is by direct evaluation of the phase retardation, $|\delta|$ using the measured ratios $I_\perp/I_\parallel$ in Equation 4–4. Note that $|\delta|$ is not uniquely determined. So when using Equation 4–4 to evaluate $|\Delta n|$, we have to specify the proper order of k for a given wavelength. Each value of k gives a different order of birefringence. The Δn determined for different orders of $k = 1, 2, 3$ are shown in Figure 4-14(b) in symbols. k was chosen so as to give a smooth curve for $\Delta n(\lambda)$ and to have first order at the longest wavelengths and for smaller strains. The $\Delta n(\lambda)$ extracted

in the two different methods are in excellent agreement with each other as shown in Figure 4-14(b) for all three samples at 15% compression. At 15% compression we expect the maximum amount of the birefringence. Adopting the same fitting procedure, we find very good agreement with the measured $\Delta n(\lambda)$ at other compressions. This is shown for sample 3 in Figure 4-15 for compressions between 2% to 13% over the whole wavelength range. Figure 4-16 displays the measured and fitted Δn values at a fixed wavelength of 632 nm. As seen clearly, the agreement at all compressions is excellent. Δn at a fixed value of λ (= 632 nm) as a function of the strain is displayed for all three samples in Figure 4-17(a). In calculating the strain, the shrinkage of the aerogel was taken into account. Δn exhibits an almost linear dependence on the compression rate. The plot in Figure 4-17(b) shows Δn for various cycles of compression for sample 3. Repeated cycles of compression-decompression seems to enhance the birefringence or anisotropy in aerogel. Note that in all the plots of Δn, only the absolute value of Δn is shown. Its sign as determined later turns out to be negative.

Figure 4-18 illustrates the total transmittance of the three samples integrated over the whole wavelength range as a function of applied strain. The transmittance for samples 2 and 3 rises initially and beyond 10% starts to drop. Sample 1 behaves little differently with a more pronounced oscillatory behavior. Figure 4-18(b) plots the wavelength dependent maximum in the transmittance in sample 2. Again this confirms the tunable wave plate character of aerogel where the maximum in the transmittance is dependent on compression and wavelength. The results shown in Figures 4-18(a) and (b) are in contrast to the birefringence observations of Pollanen *et al.* [18], where the intensity of light transmitted from a 98% porous aerogel placed between crossed polarizers did not show any maximum as function of applied strain up to 18.6%. However, it can be reconciled that in their experiments, diffuse white light was shined on cylindrically shaped samples and the output intensity from the entire sample was measured. In that case one

is effectively measuring the average intensity of light traversing different path lengths throughout the cylindrical sample.

4.3.3 Effective Medium Models

The optical properties of aerogel can be modeled by the well known effective medium approximation (EMA) theories: Maxwell-Garnett theory (MGT) and the Bruggeman effective medium approximation [72, 73]. The EMA theories are generally applied to determine the effective dielectric constant of a disordered composite medium by essentially considering the medium as a random mixture of many constituents or grains. The grains are characterized by a specific volume fraction (f), dielectric function (ε), shape and size. The main difference between the MGT and the Bruggeman EMA theory is the way in which the medium surrounding the grain is treated. In MGT, the constituents have clear distinction, that is the medium surrounding the grain is treated as one of the constituents of the mixture, whereas in the Bruggeman EMA the surrounding medium is assumed to possess the effective properties of the inhomogeneous medium. Bruggeman EMA is a symmetrical model, because the constituents are all treated the same way, that is, it assumes each individual grain to be embedded in an *effective* medium having the average properties of the medium. Even though the EMA theories are seemingly different, it turns out that for small concentrations ($f \ll 1$) the MGT and the Bruggeman EMA give identical results [73].

The effective medium approximations can be applied to our system, since the wavelength of incident light used to probe the aerogel is much larger than the size of the aerogel strands. In the Bruggemann EMA the aerogel can be considered as randomly oriented 3 - 5 nm diameter SiO_2 needles, 10 - 100 nm in length. The effective dielectric constant is obtained as a solution to the Bruggeman EMA equation [73] given by,

$$f_a \frac{\epsilon_a - \epsilon_{EMA}}{g\epsilon_a + (1-g)\epsilon_{EMA}} + (1-f_a)\frac{\epsilon_b - \epsilon_{EMA}}{g\epsilon_b + (1-g)\epsilon_{EMA}} = 0 \qquad (4\text{–}7)$$

where f_a is the volume fraction occupied by material a and ϵ_a, ϵ_b, and ϵ_{EMA} are respectively the dielectric constants of materials a, b, and the effective medium. The g is a depolarizing factor, related to the shape of the material [74, 75]. It depends on the orientation of the applied electric field. For two extreme cases, when the electric field is parallel or perpendicular to the needle, they are given by $g_{\parallel} = 0$ and $g_{\perp} = 1/2$. Here, we take a to be SiO_2, with $f_a = 0.02$ and $\epsilon_a = 2.34$; material b to be air with $\epsilon_b = 1$. We evaluate ϵ_{EMA} for two extreme cases of the electric field being in parallel and perpendicular directions to the SiO_2 needles. Then, Equation 4–7 gives upper and lower limits for $n = \sqrt{\epsilon_{EMA}}$ of $1.0081 < n < 1.0133$. In this model, uniaxial compression would orient the needles preferentially in the plane perpendicular to the compression direction. This gives us an estimation of the maximum Δn when the needles are perfectly aligned perpendicular to the compression direction, $\Delta n \equiv n_e - n_o \approx -5.2 \times 10^{-3}$. Note that the maximum birefringence observed in sample 1 at 15% compression is $|\Delta n| \approx 7 \times 10^{-5}$.

In applying the MGT approximation, we consider the SiO_2 strands as ellipsoids instead of needles. In MGT, the effective dielectric function of the composite medium is calculated by averaging the dielectric permeabilities of its constituents namely air and SiO_2 grains with their respective volume fractions. In the case of compressed aerogels, the dielectric function is a tensor due to the anisotropy generated and the depolarization effects become important. We model the system in MGT as a collection of SiO_2 ellipsoids embedded in air with the respective dielectric permeabilities, ϵ_a and ϵ_b. The procedure discussed here has been successfully applied before in understanding the form birefringence of porous semiconductors and dielectrics [76, 77]. The MGT dielectric function for oriented ellipsoids is given by [73]

$$\epsilon_{\perp,\parallel}^{eff} = \epsilon_b + \epsilon_b \frac{f(\varepsilon_a - \epsilon_b)}{g_{\perp,\parallel}(1 - f_a)(\epsilon_a - \epsilon_b) + \epsilon_b} \tag{4–8}$$

where ϵ_a, f_a as defined above are the dielectric function and volume fraction (=0.02) of SiO_2, respectively and $\epsilon_b = 1$. Note that there are no absorption bands from aerogel in

the measured wavelength range, so that the refractive index can be simply calculated as $n \approx \sqrt{\varepsilon}$. We can include the spectral dispersion of the refractive index of SiO_2 in the above equation, as a three term Sellmeier form given by Malitson [70].

$$n_a^2(\lambda) = 1 + \sum_i \frac{A_i \lambda^2}{\lambda^2 - \lambda_i^2} \tag{4–9}$$

where for $i = 1, 2, 3$, A_i and λ_i are the constant fit parameter values determined from the experimentally measured values of the refractive index of SiO_2 (see Ref. [70]). The values of the depolarization factors [74], $g_\parallel$ and $g_\perp$ depend on the ratios of the polar to the equatorial axes of the ellipsoid. Tabulated values of g can be found in the literature [75]. For example, a plane has $g_\parallel = 1, g_\perp = 0$, infinite cylinder has $g_\parallel = 0, g_\perp = 0.5$ (which is the case considered in Bruggeman EMA before) and a sphere has $g_\parallel = g_\perp = 0.333$. If the ellipsoid is a spheroid where two of the principal values of g are equal, we have the condition $g_\parallel + 2g_\perp = 1$. Using $g_\parallel$ as the fitting parameter, the birefringence $n_e - n_o = \sqrt{\varepsilon_\perp} - \sqrt{\varepsilon_\parallel}$ is calculated using Equation 4–8. This is compared against our measured values of birefringence in Figure 4-19 (disregarding the sign, only absolute values are plotted). The bottom trace of the Figure 4-19 shows the birefringence of sample 1 at 2% compression and the top trace at 15% compression. The best fits to our experimental data yield values of $g_\parallel = 0.3403$ for 15% compressed aerogel and 0.3336 for 2% compressed aerogel indicating that at 2% compression, the spherically modeled aerogel particles when compressed by 15%, deviate towards a spheroid by about 2%.

4.4 Summary

Aerogels of 98% porosity under uniaxial strain reveal large birefringence linearly proportional to the compressive strains up to 15% studied. A mechanical strain beyond 5% on the aerogel shows hysteresis in transmittance data that can be correlated to the non-recovery of the aerogel to its uncompressed length. Compressed aerogels show potential as tunable wave plates and have certain advantages compared to the conventional wave plates: low order waveplates, broadband nature, additional tuning

parameters such as the porosity, thickness and strain. The birefringence and its dispersion is in excellent agreement with the Sellmeier oscillator model. The EMA theories applied to our system give a negative sign to the birefringence values. The birefringence calculated in the MGT theory agrees well with the experimental data.

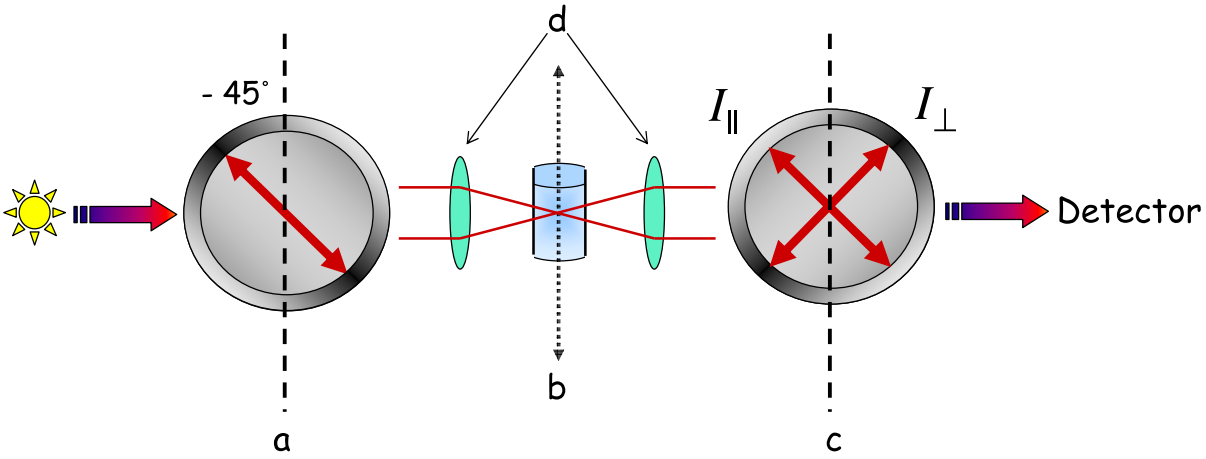

Figure 4-1. Experimental schematic of the transmission measurements. (a) Polarizer (b) axis of compression on aerogel (c) analyzer and (d) converging lens.

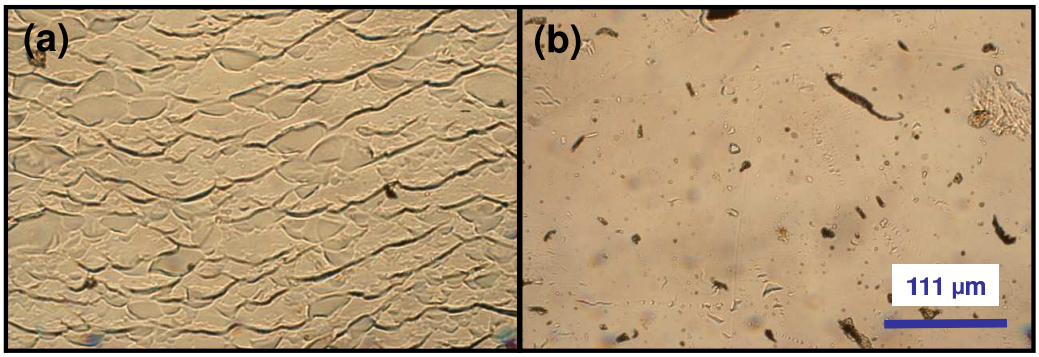

Figure 4-2. Surface images of aerogel using white light for a) cut surface and b) as-grown surface.

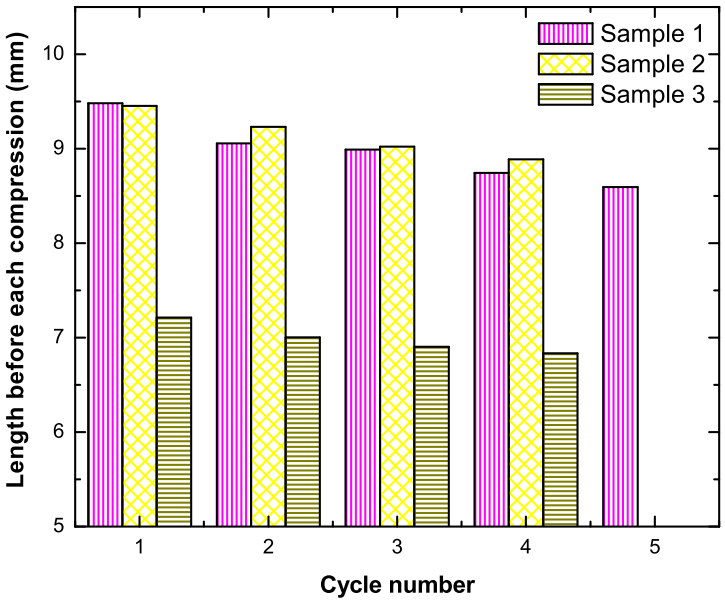

Figure 4-3. Length comparisons of samples 1, 2 and 3 before each compression for different cycles.

Table 4-1. Parameters for aerogel samples.

Sample	d_0(mm)	L(mm)	T_o	r(nm)	B	C(nm^2)
#1	8.78	9.48	90	12.3	6.63E-5	0.760
#2	7.70	9.65	80	13.7	3.63E-5	0.531
#3	4.80	7.21	80	13.5	5.53E-5	0.854

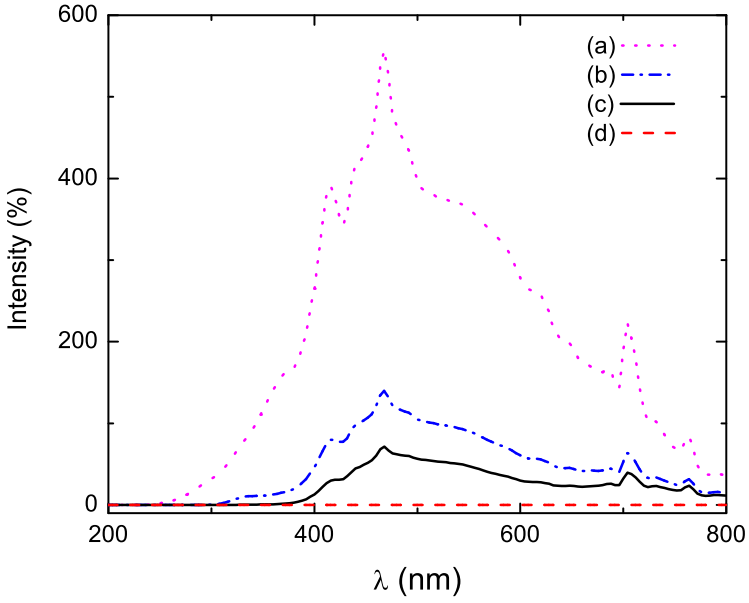

Figure 4-4. Measured intensities from the spectrometer without the sample (in free space) with (a) no polarizers, (b) no analyzer but a polarizer before the sample, (c) parallel polarizers and d) crossed polarizers.

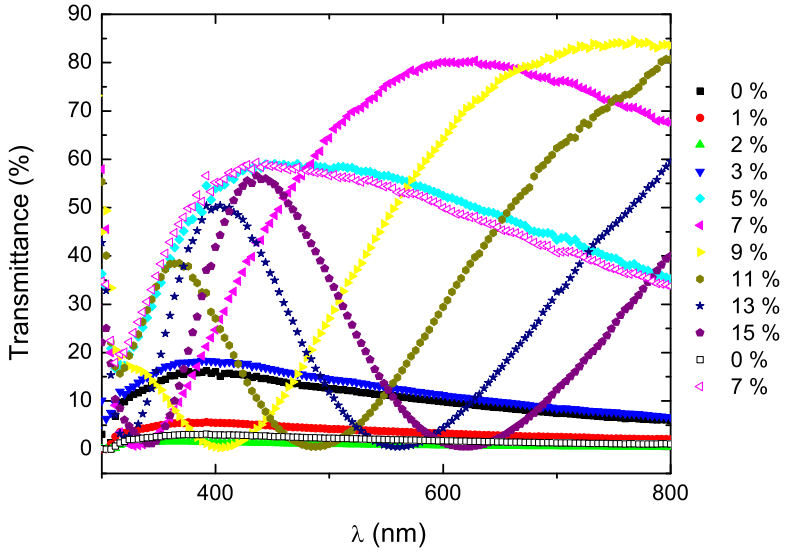

Figure 4-5. Transmittance vs. wavelength of sample 1 (cycle 4) for various compressions (closed symbols). Open symbols represent transmittance measured on decompression

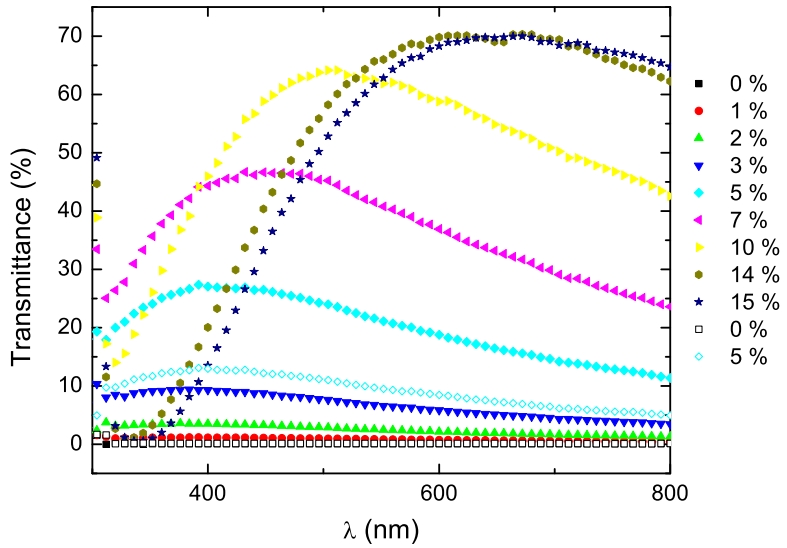

Figure 4-6. Transmittance vs. wavelength of sample 2 (cycle 4) on compression from $0 - 15\%$ (closed symbols). Open symbols represent transmittance on decompression for 0% and 5%.

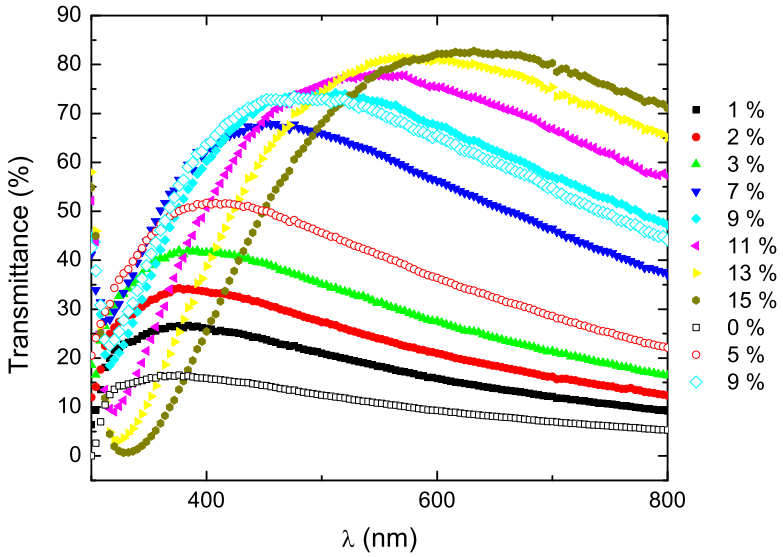

Figure 4-7. Transmittance vs. wavelength of sample 3 (cycle 4) for $0 - 15\%$ on compression (closed symbols) and 0%, 5% and 9% on decompression (Open symbols).

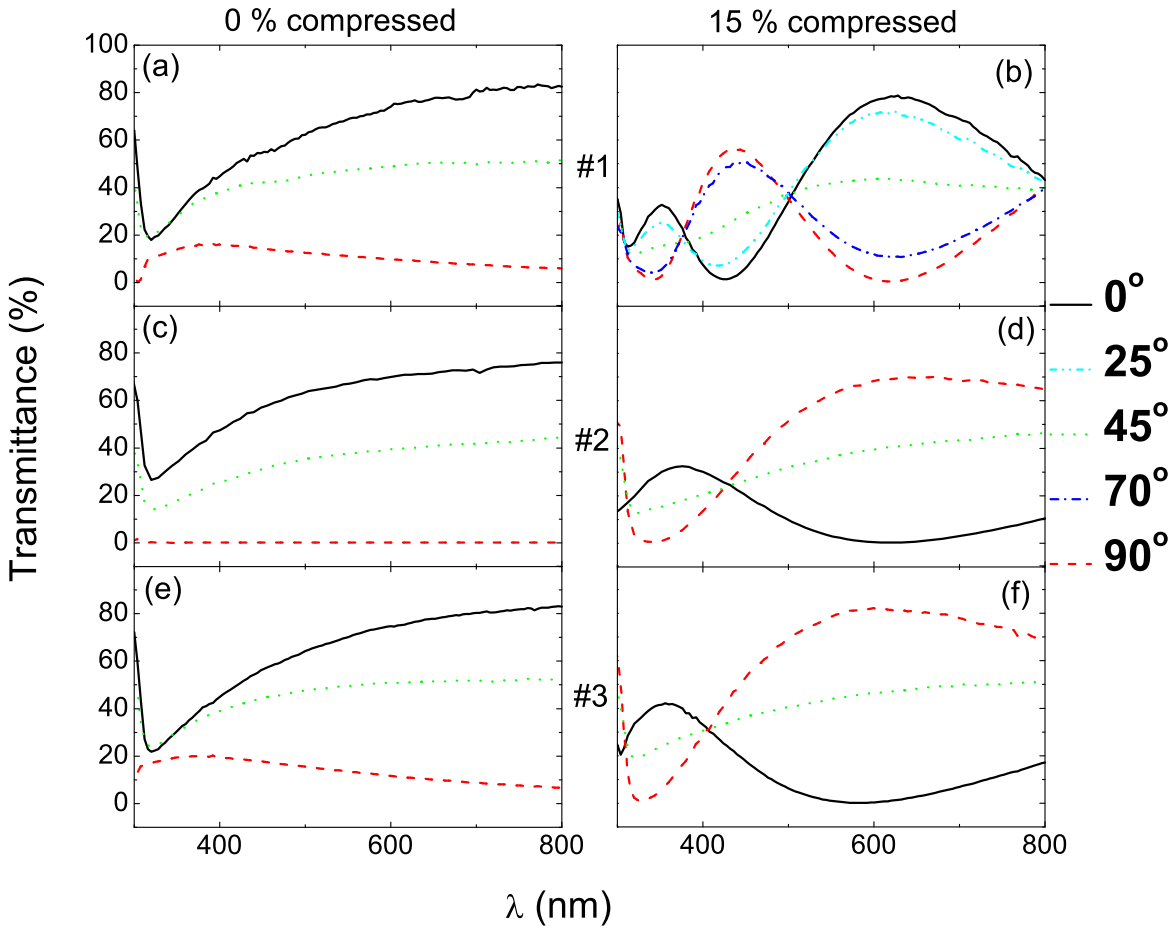

Figure 4-8. Transmittance vs. wavelength of samples 1, 2 and 3 for 0% compression (panels (a), (c), (d)) and for 15% compression (panels (b), (d), (f)).

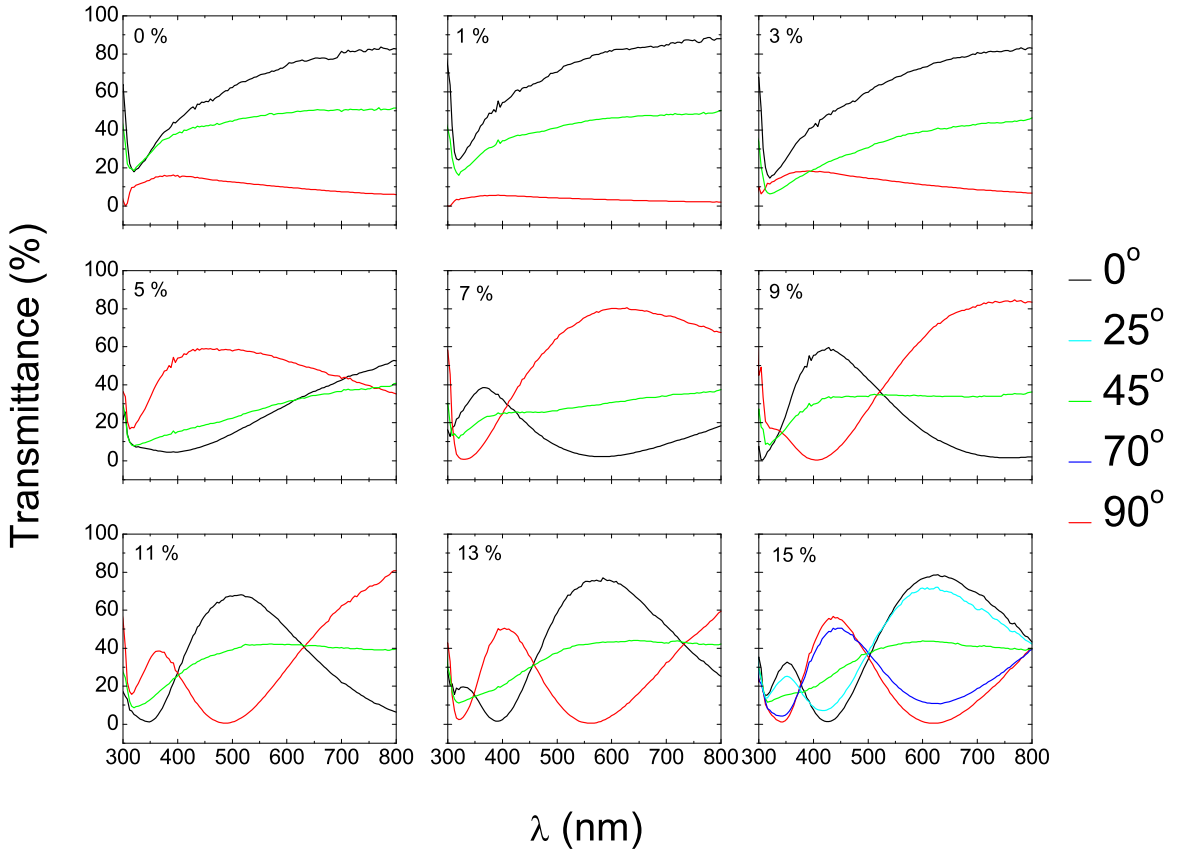

Figure 4-9. Transmittance vs. wavelength of samples 1 with progressively increasing compression shown on the panels going form left to right, at different angles of the analyzer (see legend on the right).

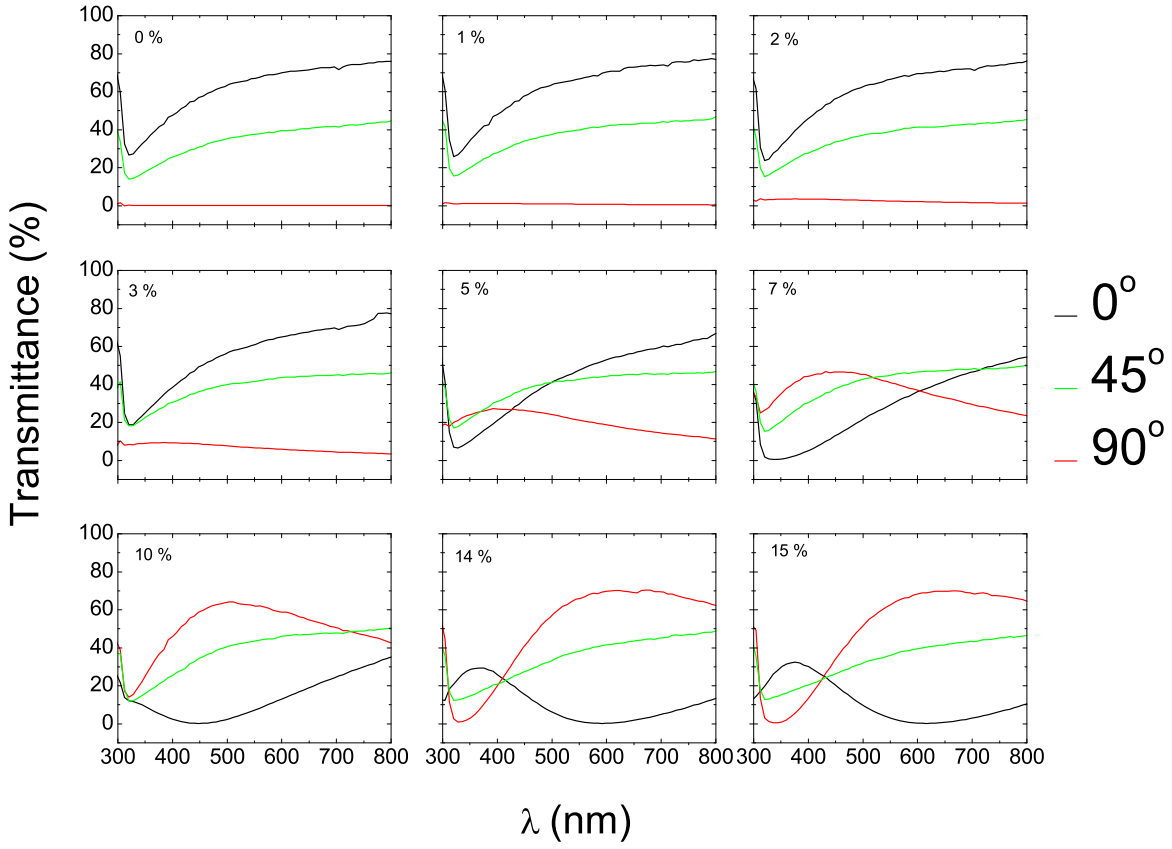

Figure 4-10. Transmittance vs. wavelength of samples 2 with progressively increasing compression shown in the panels going form left to right (0 to 15%) at different angles of the analyzer.

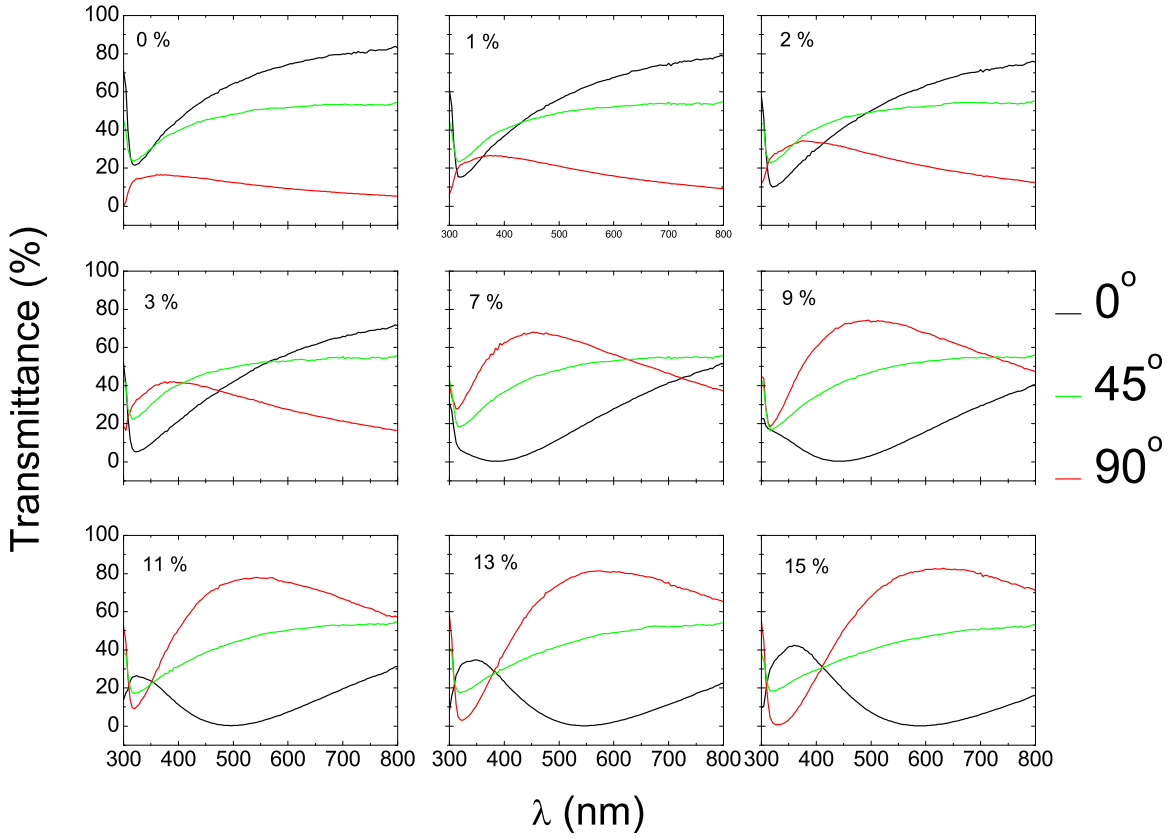

Figure 4-11. Transmittance vs. wavelength of samples 3 with increasing compression shown in the panels going form left to right (0 to 15%). The legend on the right shows the different angles of the analyzer.

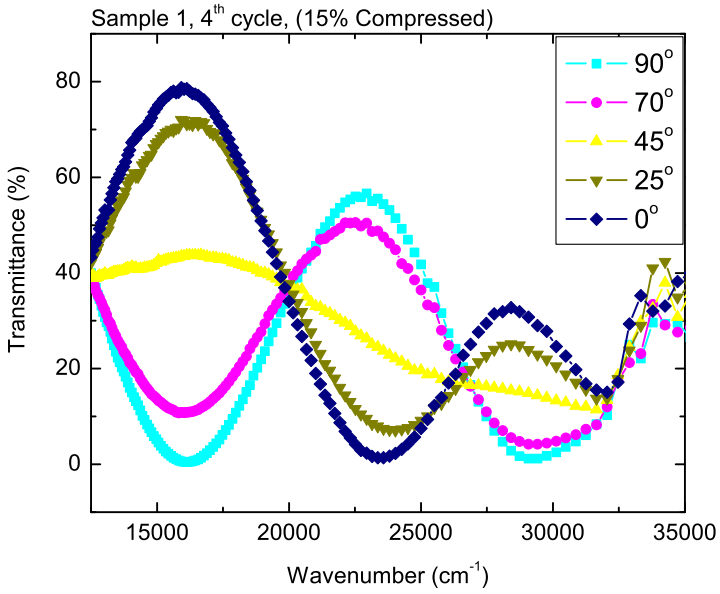

Figure 4-12. Transmittance vs. wavenumber of sample 1 at 15% compression.

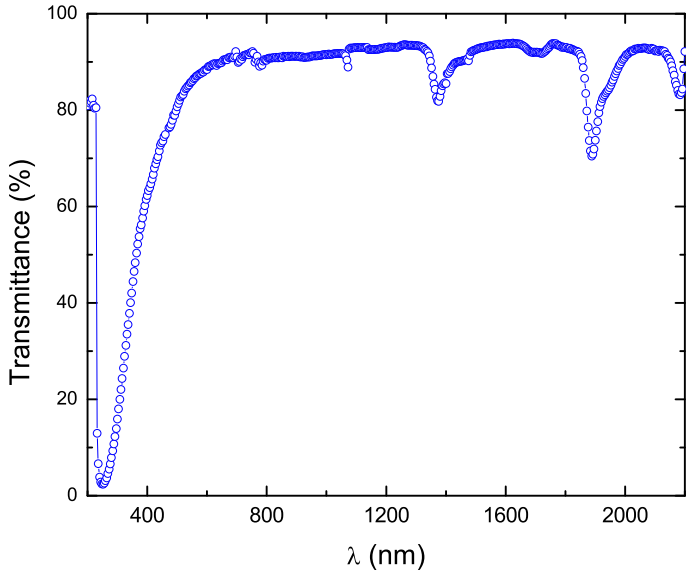

Figure 4-13. Transmittance in the UV-visible-NIR regions for an uncompressed aerogel sample 1 taken in unpolarized light. The peaks above 1200 nm are due to adsorbed water as seen before in Ref. [68].

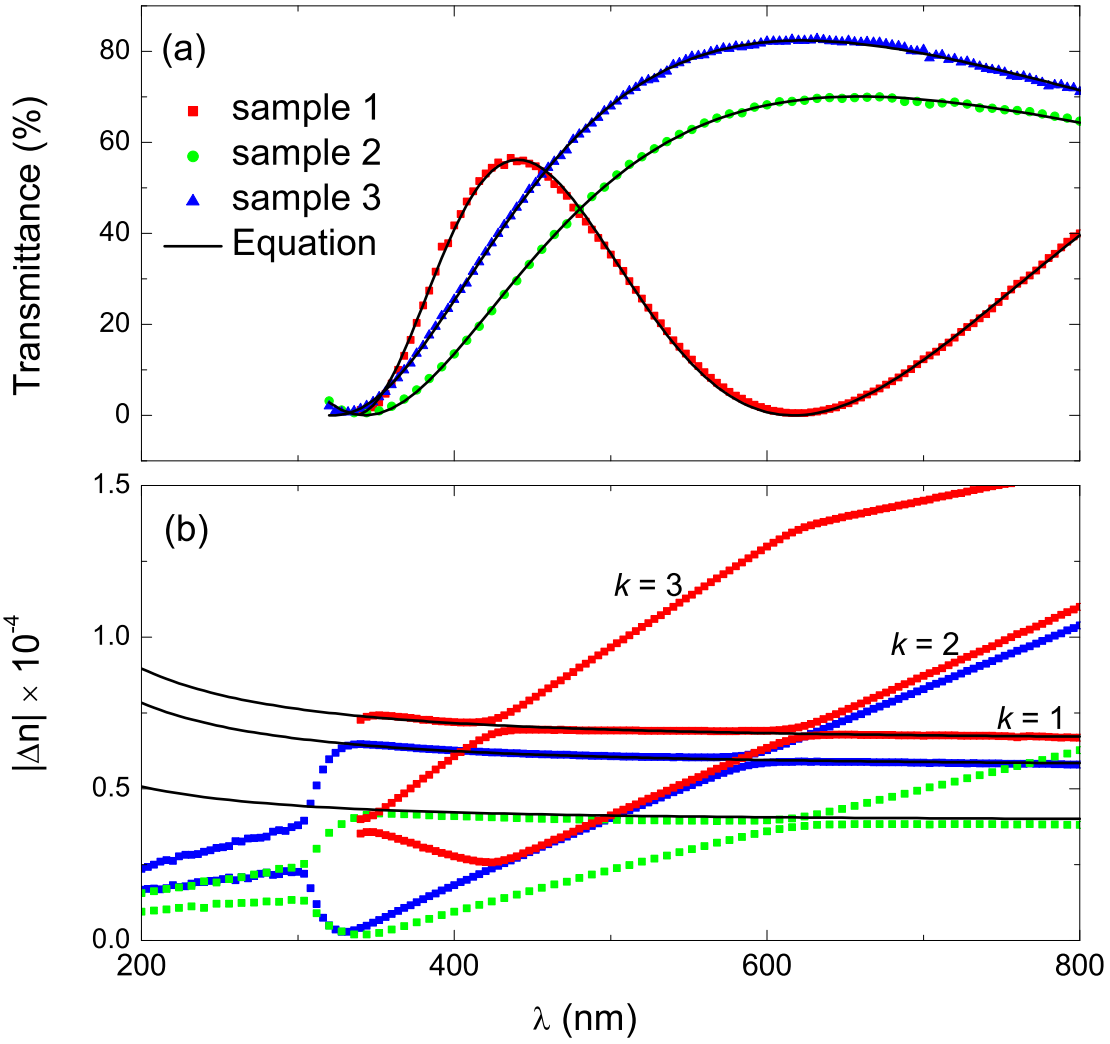

Figure 4-14. (a) Transmittance in the cross polarized configuration for samples 1, 2 and 3 (top panel). (b) The birefringence dispersion $\Delta n(\lambda)$. The black lines are fits using Equations 4–5 and 4–6. $\Delta n(\lambda)$ (symbols in panel (b)) determined for the different order of relative retardation, $k = 1, 2, 3$ are indicated.

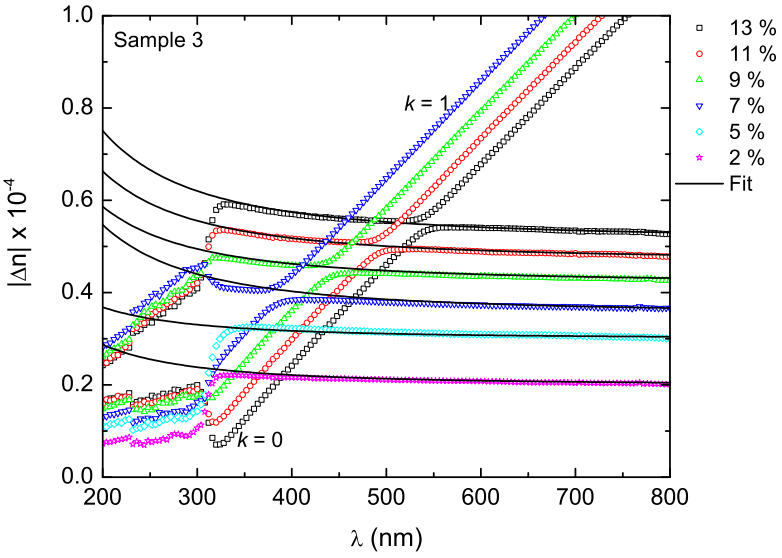

Figure 4-15. Birefringence dispersion in aerogel sample 3 for various strains (see legend) 2% to 13%. Measured Δn using Equation 4–1 is shown in symbols. The black lines are the calculated Δn by fitting the wavelength dependant transmittance data using Equations 4–5 and 4–6.

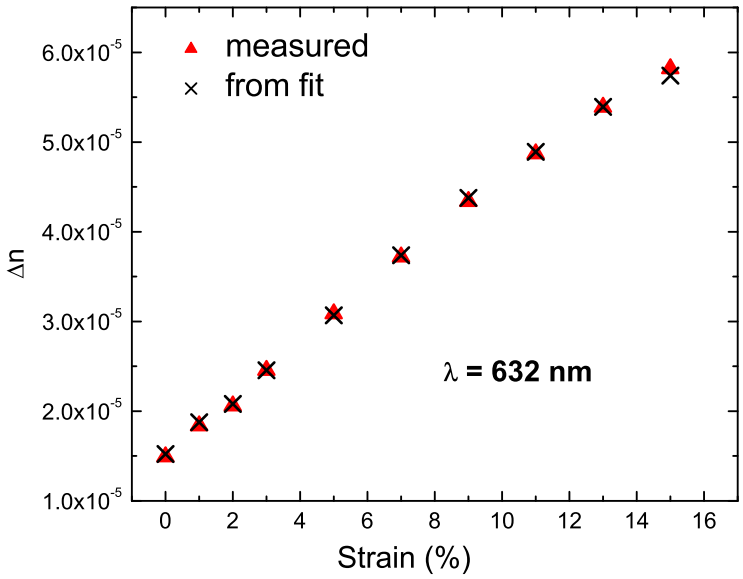

Figure 4-16. (a) Measured Δn vs. strain for sample 3 at a wavelength of 632 nm (red triangles). The black crosses are the calculated Δn by fitting the wavelength dependant transmittance data to Equation 4–5.

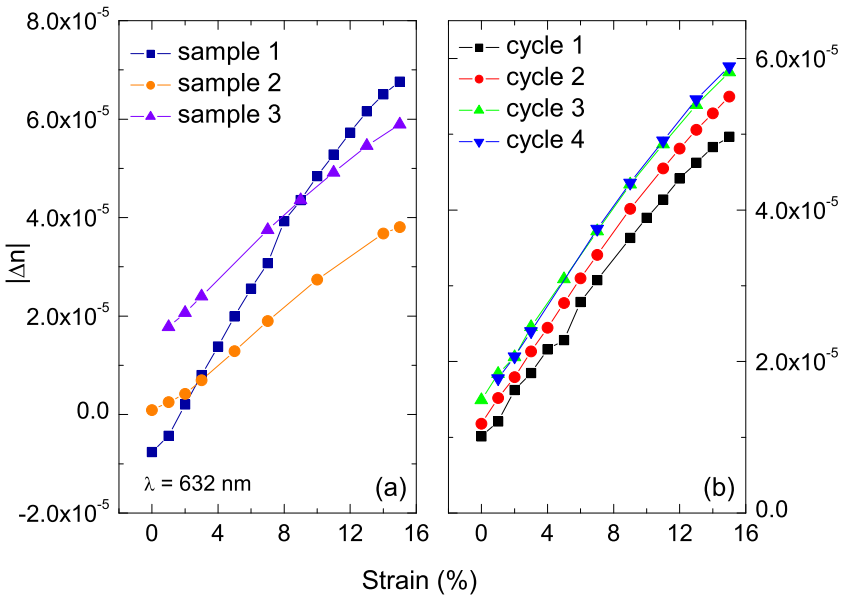

Figure 4-17. (a) Δn as function of applied strain for all samples at a wavelength of 632 nm. (b) Sample 3 for different cycles of compression.

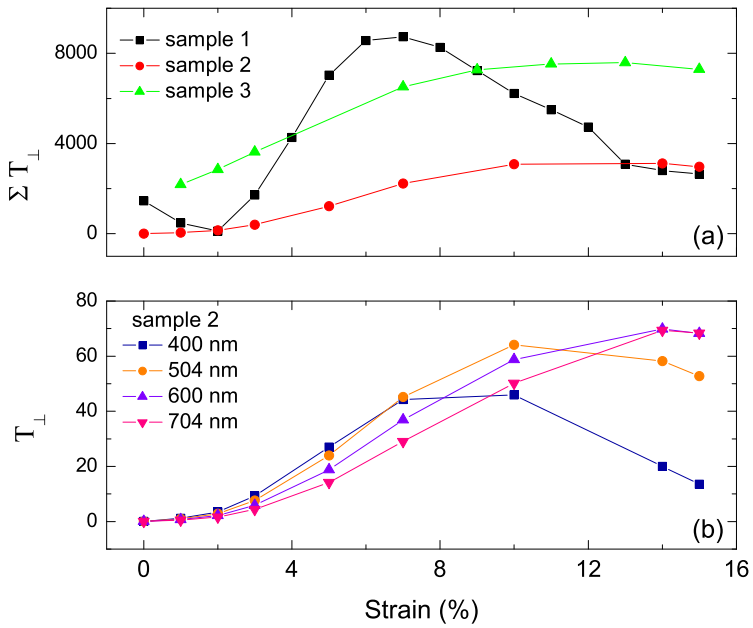

Figure 4-18. (a) Transmission integrated over all wavelengths (320 - 800 nm) in the cross polarized set-up as a function of strain and (b) at different fixed wavelengths for sample 2.

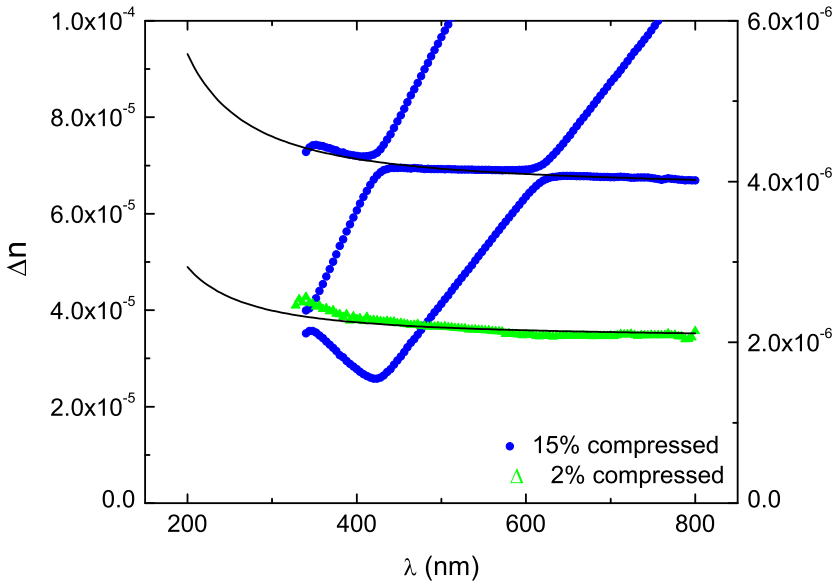

Figure 4-19. Birefringence of sample 1 at 15% compression (left axis) and 2% compression (right axis) in blue and green symbols, respectively. The solid lines are the Δn calculated from the MGT Equation 4–8.

CHAPTER 5
TRANSVERSE ACOUSTIC MEASUREMENTS IN COMPRESSED AEROGELS

Although it is now evident that the B-like phase in aerogel [78] is in fact the Balian-Werthamer phase, the exact nature of the A-like phase in aerogel is not yet known. A number of experiments using acoustic impedance as well as NMR techniques have found that the A-like phase is metastable [31, 35] and is an equal spin pairing (ESP) state [20, 37, 79]. In most of the experiments [31, 34, 35, 80] the A-like phase has been found to nucleate within a narrow temperature band less than 100 μK right below the superfluid transition in 98% aerogel in the absence of magnetic fields. Despite the clear recognition of the spin structure in the A-like phase, the orbital part of the order parameter has not been identified yet. There are different classes of ESP states proposed as candidates for this phase: a superfluid glass or Larkin-Imry-Ma state proposed by Volovik [42], and the robust phase proposed by Fomin [29]. Thuneberg *et al.* [23] have pointed out that the anisotropic scattering from aerogel strands may influence the relative stability of the A and the B phases. In this context, we provided an interpretation that can account for the significant influence of aerogel on the A-B transition, considering the coupling between the *anisotropic* order parameter and *anisotropic disorder*. We also proposed an experiment that can elucidate the role of anisotropic disorder in uniaxially deformed aerogels where the global anisotropy could be induced and could therefore produce a similar effect as a magnetic field [35]. Our claim is supported by theoretical calculations by Aoyama and Ikeda [45]. They predicted a widened A-like phase in uniaxially compressed aerogels, and more interestingly, the appearance of the polar phase in uniaxially stretched aerogel.

5.1 Experiments in Compressed Aerogels

The first transverse acoustic impedance measurements in anisotropic aerogel (98% porosity) were reported in 2006 by the Northwestern group [81] where the anisotropy was induced by preferential shrinkage (and not by compression) in the *radial* direction during chemical synthesis of the aerogel. Later that year, our group performed acoustic

measurements in 5% uniaxially compressed aerogel. These results reported at the QFS 2006 conference are discussed in this chapter.

In the initial experiments on the aerogel with 10% preferential radial shrinkage, Davis *et al.* [81] found a stable region of the superfluid phase although the nature of the phase has not been established. In their recent experiments [82] 98% aerogel was compressed by 17%. They observed no difference in the degree of supercooling of the A-B transition when compared to the uncompressed aerogel measurements, except at low pressure (< 25 bar) where a longer degree of supercooling was observed, indicating that the mechanism for the nucleation of the B-like phase is suppressed at lower pressures in compressed aerogel. In their tracking experiments, the coexistence region of the A-like and the B-like phases was found to be essentially the same as in uncompressed aerogels. They conclude that with 17% uniaxially compressed aerogel there is no evidence for the stabilization of the A-like phase, which is in contradiction to the theoretical predictions and our experimental results presented in this chapter. Although, as pointed out by them [83], it is possible that the aerogel at the surface of their transducer might not be as anisotropic as the bulk of aerogel observed in the optical measurements. This is important since the transverse acoustic response is mainly sensitive to the area near the interface of the transducer within the shear penetration depth.

Unlike the transverse acoustic measurements, NMR technique is sensitive to the entire volume of the sample. There are recent NMR experiments which investigated the superfluid phases in deformed aerogel [84–87]. Kunimatsu *et al.* [84] and Dmitriev *et al.* [85] have given first experimental evidence that uniaxial compression on aerogel orients the orbital angular momentum vector $\hat{l}$ along the anisotropy (compression) axis and parallel to the applied magnetic field in both the A-like and B-like phases. Another interesting phenomenon not possible in the bulk ^{3}He-A phase but observed in the A-like phase in uniaxially deformed aerogel is the coherent precession of magnetization [86]. In the bulk A phase, minimization of the dipole-dipole energy requires the $\hat{l}$ vector to

be oriented perpendicular to the magnetic field **H**. However it is found that by uniaxial deformation along **H**, the $\hat{l}$ vector oriented along **H** allows for the observation of the coherent precession of magnetization. Here, we present our measurements in compressed aerogels using transverse acoustic impedance technique to identify the A-like to B-like transition.

5.2 Experimental Technique

It has been demonstrated that the shear acoustic response from a piezoelectric transducer immersed in liquid ^{3}He is sensitive to the phase transitions occurring in the bulk liquid [8]. This has been found to be true even in the presence of aerogel [31, 33, 35]. The acoustic impedance [8] is defined by $Z = \Pi/\dot{u}_x$, where Π is the stress induced in the medium due to the vibrating transducer and $\dot{u}_x$ is the velocity of the interface between the piezoelectric transducer and the medium. The acoustic impedance is a measure of the energy transferred from the transducer to the medium. In our experiments, we do not directly measure the characteristic impedance, an intrinsic property of the liquid, but the change in electrical impedance generated by the change in the acoustic impedance of the surrounding superfluid is measured. We used AC-cut quartz transducers that generate shear waves with a fundamental frequency of 3 MHz. These transducers are excited continuously at 8.6 MHz (3^{rd} harmonics) and the change in their electrical impedance is measured as a function of temperature. The coaxes used for these measurements are all high frequency coaxes described in section 3.4.1 and not the homemade Cu-Ni capillary coaxes. The high resolution electrical impedance measurement is accomplished by using a bridge type continuous wave (cw) spectrometer [36]. Two spectrometers of similar design were used in our experiment. They were built by Hyunchang Choi, a former graduate student and Jose Cancino, a former undergraduate student. A block diagram of the electrical impedance bridge is shown in Figure 5-3. An Agilent Technologies 8648A signal generator provides the RF output that is typically set at 11 dBm. The applied signal is frequency modulated (FM) at 400 Hz with a FM width between 1-3 kHz. The FM

signal is split into 3 ways by a power splitter. Two of the three ports of the splitter are connected to the two arms of a quadrature hybrid (QHB, SMC DQK-3-32S) through variable attenuators and a phase shifter. The third arm of the QHB is connected to the transducer at low temperature in the cryostat. Some part of the signal applied to the transducer through the quadrature hybrid is reflected back due to impedance mismatch at the transducer. The imbalance signal generated at the output of the QHB (numbered 4 in Figure 5-3) is nulled by using the attenuators and the phase shifter on arms 1 and 2. This nulling is performed right at the transducer resonance frequency shown in Figure 5-4. The reflected signal from the transducer appearing in arm 4 of the QHB is amplified through a preamplifier (MITEQ, AU-1519) and mixed with the carrier signal from the power splitter. The high frequency signal is down converted at the lock-in (PARC 124A) to the low frequency signal at the modulation frequency of 400 Hz. When the frequency is swept from the oscillator, the resulting output from the impedance bridge implementing the FM technique is not the transducer resonance spectrum, but its derivative as shown in Figure 5-4. To maximize the sensitivity, the resonance shape and amplitude are optimized by adjusting the attenuators and the phase shifter. The nulling procedure is usually performed in the normal liquid right above T_c.

5.3 Acoustic Cell

The measurements were performed on 98% porosity aerogels at two different compressions: 5% and 10%. The acoustic cell consists of a Macor structure that supports two AC-cut quartz transducers. Figure 5-1 shows a picture of the acoustic cell with the aerogel samples inside the Macor container. The Macor structure houses two 98% porosity aerogels: one compressed at the top and the other uncompressed at the bottom of the structure. The compression along the symmetry axis is achieved by the top cap and the spacer. Different compression can be achieved by varying the thickness of the spacer between the Macor cap and the aerogel. The compressed aerogel was placed against a transducer from the top whereas the uncompressed aerogel was pushed up against another

transducer by a Kapton spring. The two transducers were separated by a gap of 0.254 cm. In this configuration, (see Figure 5-1) each transducer is in contact with the aerogel on one side and the bulk liquid on the other side, allowing us to simultaneously observe the transition signatures from the pure and dirty ^{3}He. The first set of measurements were performed in commercially available aerogel from MarkeTech International Inc. under 5% compression. The aerogel blocks as received from the company were cut using a high speed diamond cutter to fit our experimental cell. We have found that the contact between the aerogel surface and the transducer is crucial in detecting a clear phase transition signature. A 0.001" thick Kapton polyamide tape turned into a small tube and glued to the base of the cell on its side provided a spring-like force to the aerogel placed on top of it and pushed it against the transducer. As it turns out, this plan did not work out well and we were unable to observe any transition features except the bulk from this transducer. This could be either due to the rough surface of the aerogel in contact with the transducer or the Kapton spring not providing enough force. The difficulty is in applying enough pressure on the aerogel without causing significant compression. Later, we used aerogel sample provided by Norbert Mulders for measurements on 10% compressed aerogel. They were carefully grown with flat parallel surfaces. We used the same Macor structure for these measurements. Because we glued the bottom of the Macor structure to the plastic cell base, we could only replace the compressed aerogel side of the transducer.

The aerogel acoustic cell was assembled into a polycarbonate container and epoxied to a phosphor bronze body. The method of attachment to the nuclear demagnetization stage via a heat exchanger for cooling the liquid ^{3}He is described in chapter 3 (see Figure 3-15). Experiments in 5% compressed aerogel have been performed using the design shown in Figure 5-2(1). With this scheme, we had a significant thermal gradient ($\approx 300\mu$K) between the melting curve thermometer (MCT) attached to the nuclear stage and the liquid ^{3}He in the cell. We believe that this gradient is caused by inefficient thermal contact in our radial clamping design (see Figures 5-2(1) and 3-15b). In our later experiments with 10%

compressed aerogel, this has been eliminated by adopting a different heat exchanger as shown in Figure 5-2(2) and Figure 3-15a. The design details of these two heat exchangers are discussed in chapter 3. In the new design, the MCT is attached directly to the cell heat exchanger. No heating effects were observed in the cell. The RF excitation level on the transducers is always kept below 3 mV peak to peak. After initial cool down, we observe large time dependent heat leak probably from the rather massive plastic body of the cell. This time dependent heat leak has not been measured. Finally, it is important to note that damage to the high porosity aerogel structure can occur during filling and emptying of the cell with ^{3}He due to surface tension between the liquid-vapor interface and the aerogel [65]. Therefore, in all our measurements, liquid ^{3}He was filled or emptied into the aerogel cell hypercritically (above the liquid-vapor critical point of ^{3}He: 3.3 K, 1 bar) thereby avoiding the formation of a liquid-vapor interface inside the cell.

5.4 Results

Figures from 5-5 to 5-14 show the acoustic response from the transducer with 5% compressed aerogel in a ^{3}He pressure of 32 bar and at magnetic fields from 0 to 2 kG applied parallel to the aerogel compression axis. All plots show the acoustic response from the transducers and temperature from the MCT as a function of time. We observed hysteresis between warming and cooling due to a thermal gradient between the MCT and the sample cell. Our typical warming and cooling rate is ≈ 0.066 mK/h. As marked clearly in the plots, we observe the bulk superfluid (T_c) and the A-B transition (T_{AB}) as sudden jumps in the acoustic response (except for an instance of zero field warming data near the A-B transition due to some unwanted noise from the lock-in amplifiers). The black circles in the zero field plots show the bulk transition features occurring simultaneously on the uncompressed aerogel transducer. As mentioned in the previous section 5.3, no transition features in the uncompressed aerogel are seen due to a bad contact of the transducer with uncompressed aerogel. Henceforth, we do not show this trace in the rest of the plots. The superfluid transition in compressed aerogel (T_{ac}) is

identified by the distinct slope change. The aerogel A-like to B-like transition (T_{aAB}) is identified as a sharp step in the trace right after the bulk A-B transition on cooling and right before the bulk A-B transition on warming. The insets of Figures 5-9 and 5-10 show the close-up of these features. In order to confirm the supercooled nature of the A-like to B-like transition, we performed tracking experiments in a field of 1.5 kG as shown in Figures 5-11 and 5-12. In Figure 5-11, in the red trace two clear supercooled A-B transition steps are shown. The cell is then slowly warmed from the aerogel B-like phase up to a point right before the B-like to A-like feature occurs but higher than the supercooled bulk A-B and aerogel A-B temperatures, stayed for a while and then cooled slowly to watch the acoustic trace for the signature of the supercooled A-like to B-like transition. As evident from the Figure 5-11, we do not see any supercooled feature confirming that we are still following the B-phase in the bulk and aerogel. In Figure 5-12 two supercooled and two warming A-B transition features are marked. On turning around in temperature while cooling, right after the supercooled bulk A-B transition but before going into the aerogel A-like to B-like transition, we should not see any feature from the aerogel when we warm up from this point. That is, if the supercooled feature is indeed the A-like to B-like transition, there should be a signature on warming only after cooling through this feature. This is in fact the case as seen on warming back without going into the A-like to B-like feature, only the bulk A-B feature is seen. Similar supercooled features, in addition to the bulk A-B transition, are observed in a field of 2 kG. These traces are shown in Figures 5-13 and 5-14.

Since the temperature given by the MCT was not in equilibrium with the cell temperature, we cannot determine the correct values of the transition temperatures in the cell from the MCT. However, we can extract the actual temperature from the acoustic trace in the cell. Using the known bulk superfluid transition temperature and the bulk A-B transition on warming as the fixed points, we extrapolate the temperature of the aerogel A-like to B-like transition feature assuming a linear warming or cooling rate.

This scheme provides reliable temperature for the aerogel A-like to B-like transitions because they occur very close to the bulk A-B transitions. The A-like to B-like transition temperature on warming in 5% compressed aerogel is plotted in Figure 5-15 (red circles) along with the data from Gervais *et al.* [31] at a slightly different pressure of 33.4 bar. The triangles denote the aerogel superfluid transition temperatures, T_{ac} and circles are the warming A-like to B-like transitions in aerogel, T_{aAB} determined by Gervais *et al.* [31] using transverse acoustic impedance measurements in uncompressed aerogel. The blue bar shows our superfluid transition in aerogel around 2.2 mK which is slightly higher than that of Gervais *et al.* T_{ac}'s have been previously reported to be somewhat different for different aerogel samples even with same porosity [17]. From this plot, we observe a quadratic suppression of the warming A-like to B-like transition in compressed aerogel up to 2 kG as observed in uncompressed aerogel [31, 36]. More importantly, an extrapolation to zero field yields $T_{aAB} \approx 1.95$ mK. This indicates that the width of the A-like phase is indeed widened by $\approx 300\mu$K.

The next set of experiments were performed on 10% compressed aerogel at two different pressures of 29.2 bar and 31.8 bar. Temperature sweeps were performed in magnetic fields of 0, 1, 2 and 3 kG. The acoustic impedance traces on cooling and warming are shown in Figures 5-16 and 5-17 for pressures of 29.2 and 31.8 bar respectively. Each panel in the plots depicts four traces for the four different magnetic fields. At 29 bar, on cooling, the sharp drop at 2.43 mK signifies the bulk superfluid transition. Around 2.1 mK, the smooth transition marks the aerogel superfluid phase followed by the bulk A-B transitions. Similar traces can be seen at 32 bar pressure (Figure 5-17). On cooling, the bulk A-B transition occurs at progressively lower temperatures with increasing magnetic fields as expected, but there is no signature of a supercooled A-like to B-like transition in aerogel as seen in the uncompressed aerogel or the 5% compressed aerogel. On warming, only the bulk A-B transition features appear at the temperatures expected for a given magnetic field. This observation suggests that the width of the A-like

phase in 10% compressed aerogel is significantly widened and persists down to the lowest temperatures shown. We have made attempts to trigger the A-B like transition by lightly banging the dewar at the lowest temperature ($\approx 300\mu$K) but no features were observed. We need to remark here that there is a possibility of a transition into 2D-like planar phase occurring instead of the A-like phase. Unlike the A-B transition, the planar to B-like phase is second order transition which could be giving rise a subtle feature, difficult to observe using transverse acoustic impedance measurement.

An important observation made after warming up and opening the acoustic cell at room temperature was that the aerogel was significantly shrunk along its length casting doubts on the aerogel not being in contact with the transducer. We do not know exactly when the aerogel was shrunk. But, we do know from our experiments at room temperature on several samples of aerogel that the aerogel shrinks in length after a cycle of compression and decompression as discussed in chapter 4. Furthermore, we recently performed measurements on a 7% compressed aerogel sample observing similar acoustic traces at low temperatures as the 10% compressed aerogel. However, this sample did not show any observable shrinkage in length after inspection at room temperature. We want to emphasize from our observations that one should keep in view the possibility of shrinkage that can occur in aerogels when performing experiments with compressed aerogels using transverse acoustic impedance technique.

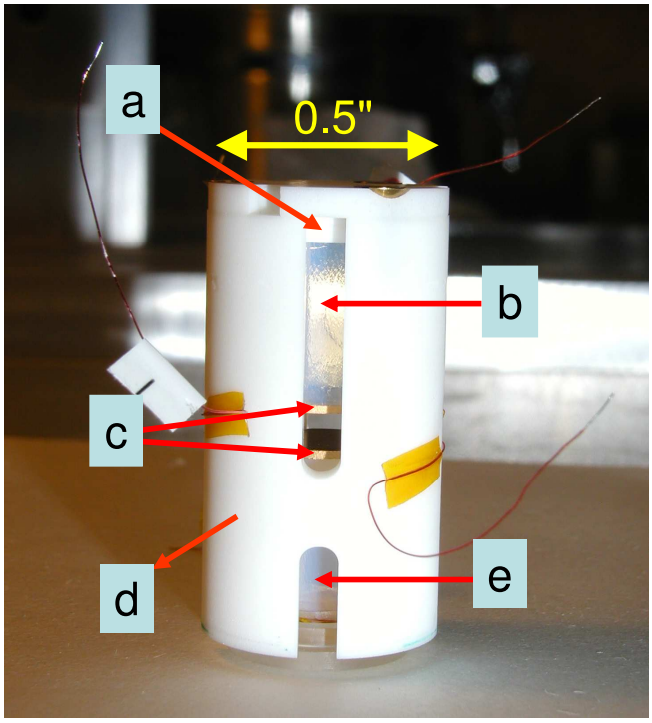

Figure 5-1. Picture of Macor experimental cell with aerogel. a) macor spacer b) compressed aerogel c) transducers d) outer macor body e) uncompressed aerogel.

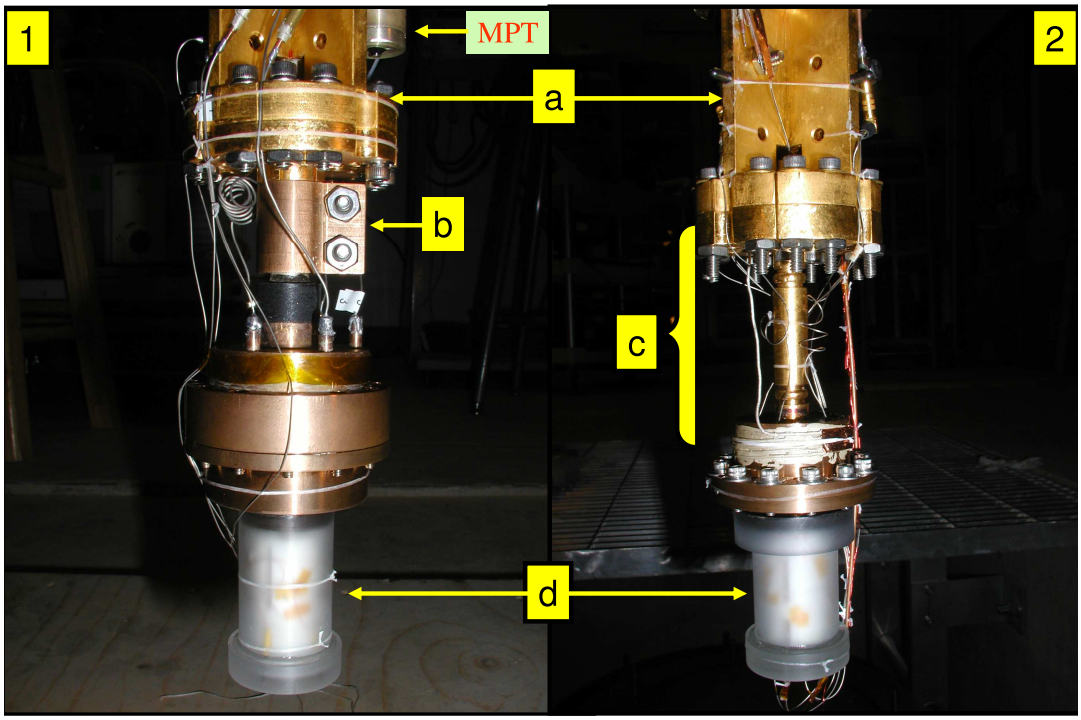

Figure 5-2. Picture of different experimental cell set-up: (1) Older cell with the phosphor bronze clamp (b) (see chapter 3 for details) with the heat exchanger and plastic cell (d) attached to the CDS (a). (2) New set-up with the heat exchanger (c) attached directly to the CDS.

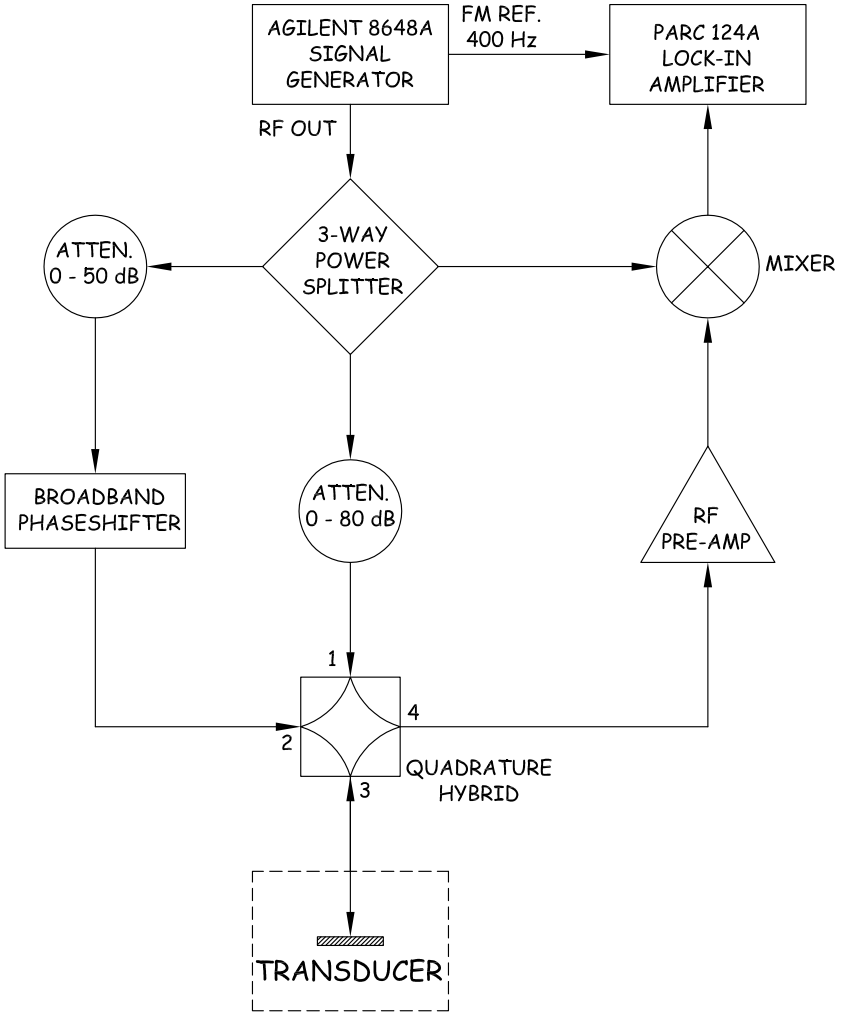

Figure 5-3. Schematic diagram of the CW spectrometer used in this work. The dashed box indicates the transducer inside the Cryostat. The arrows indicate the direction of RF signal flow.

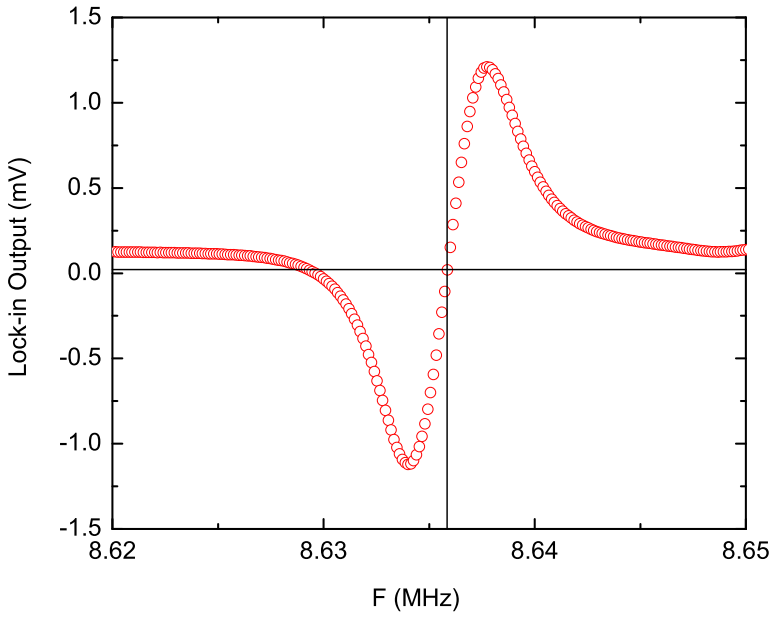

Figure 5-4. Spectrometer output showing the resonance spectrum from a frequency sweep of the transducer. The marked cross-hair indicates the frequency at which the transducer is tuned for maximum sensitivity.

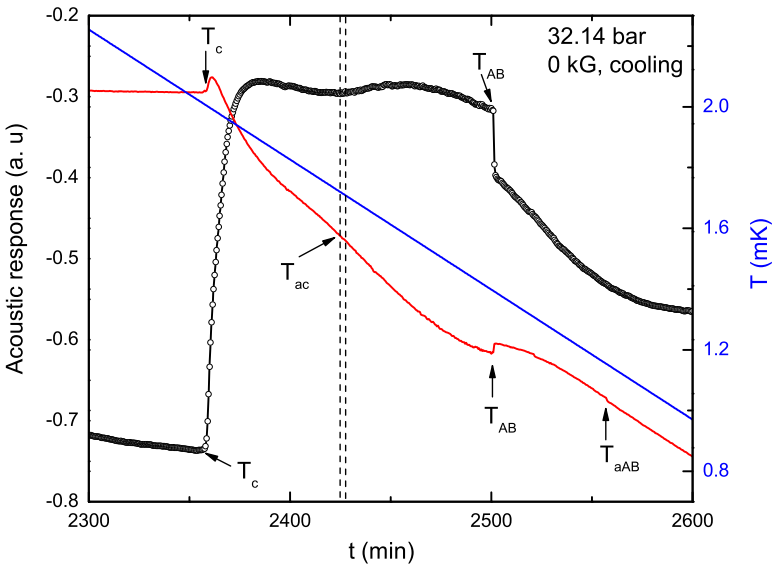

Figure 5-5. Acoustic response on cooling in zero field at 32 bar from the uncompressed aerogel (in black circles) and from the 5 % compressed aerogel (in red line). The blue line indicates the temperature of MCT.

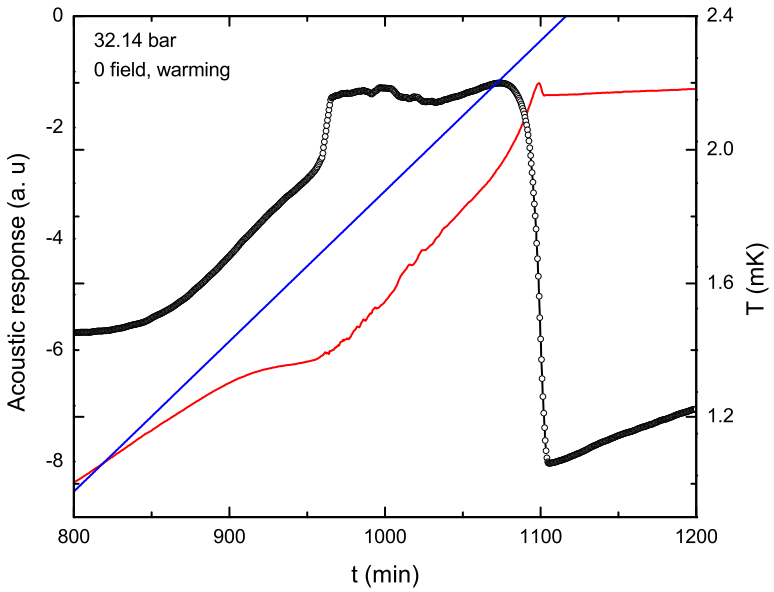

Figure 5-6. Acoustic response on warming in zero field and 32 bar pressure from the uncompressed aerogel (in black circles) and 5 % compressed aerogel (blue line).

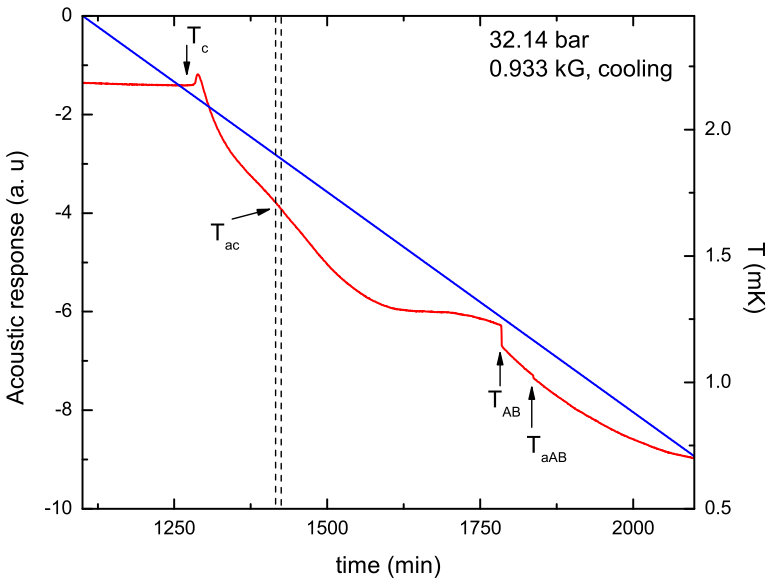

Figure 5-7. Acoustic response on cooling in 0.933 kG and 32 bar pressure. Temperature axis is on right hand side and is shown in blue.

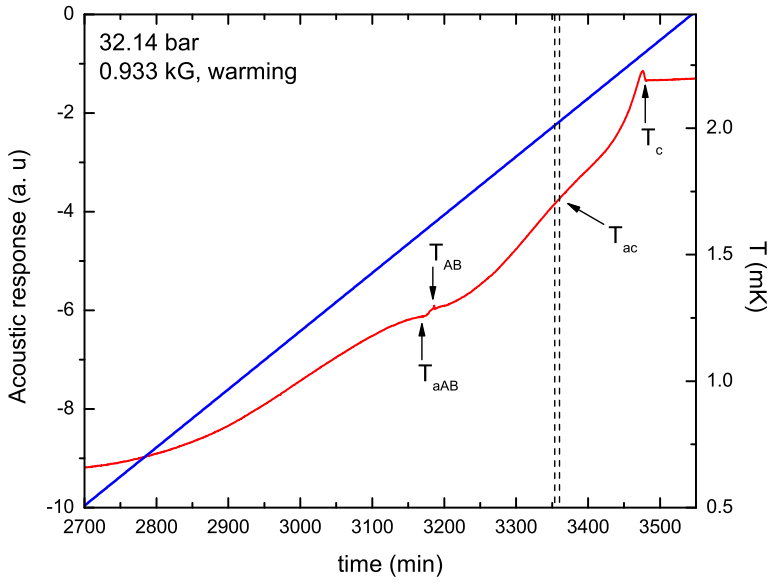

Figure 5-8. Acoustic response on warming in 0.933 kG and 32 bar pressure. Temperature axis is on right hand side and is shown in blue.

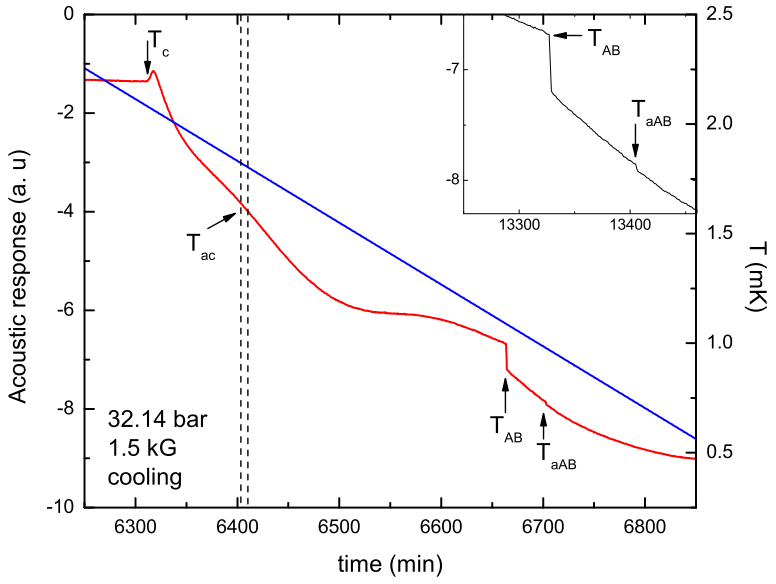

Figure 5-9. Acoustic response on cooling in 1.5 kG and 32 bar pressure. Temperature axis is on right hand side and is shown in blue. Inset shows a close-up of the steps in the acoustic trace.

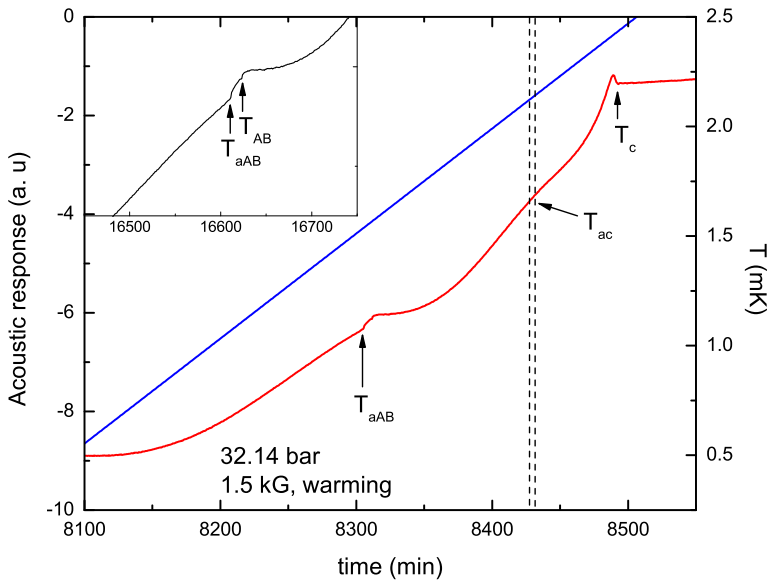

Figure 5-10. Acoustic response on warming in 1.5 kG and 32 bar pressure in c 5% compressed aerogel. Inset show a close-up of the double jump feature in the acoustic trace indicating bulk and aerogel transition.

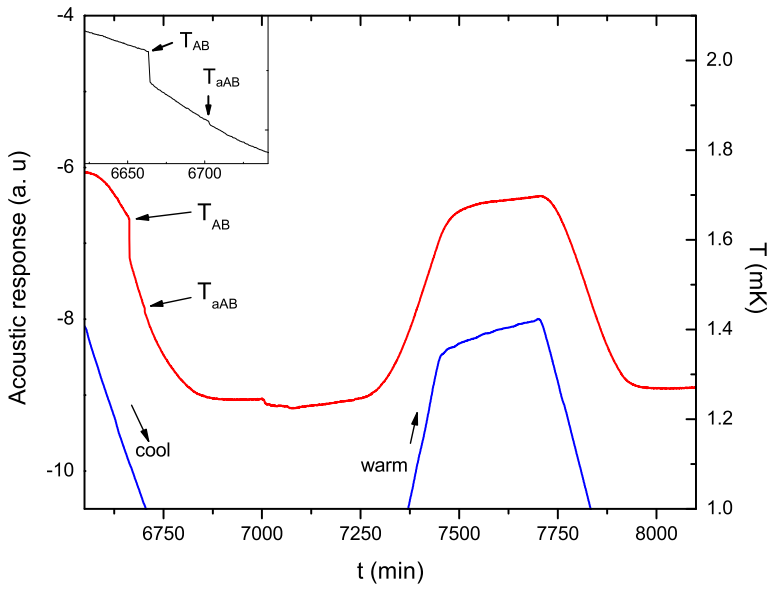

Figure 5-11. Tracking of aerogel A-B like transition in 5% compressed aerogel at 1.5 kG field and 32 bar pressure. Supercooled bulk A-B and aerogel A-B transitions are marked with arrows. On slow warming beyond the supercooled A-B transition temperatures, and then cooling down no supercooled features are seen.

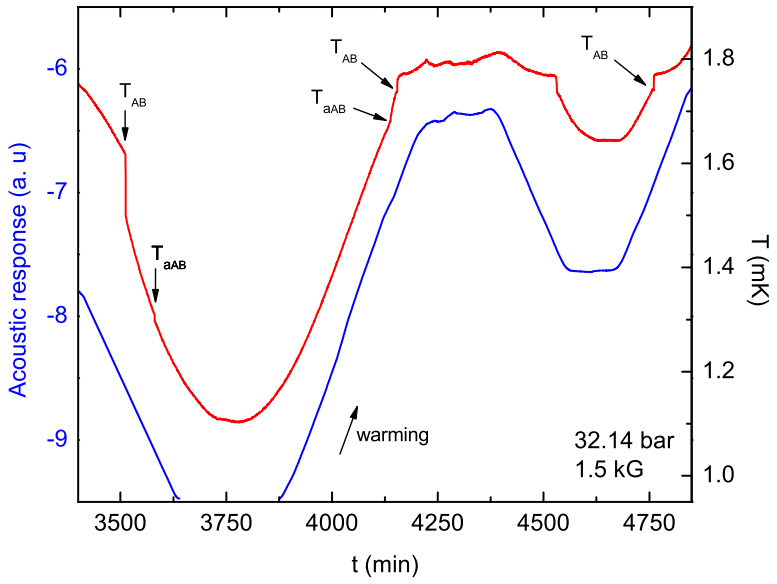

Figure 5-12. Tracking of aerogel A-B like transition at 1.5 kG field and 32 bar pressure. Both supercooled and warming A-B transition in the bulk and aerogel are shown with arrows. While cooling, turning around in temperature right after the supercooled bulk A-B but before the aerogel A-like to B-like feature, only the bulk feature is seen on warming.

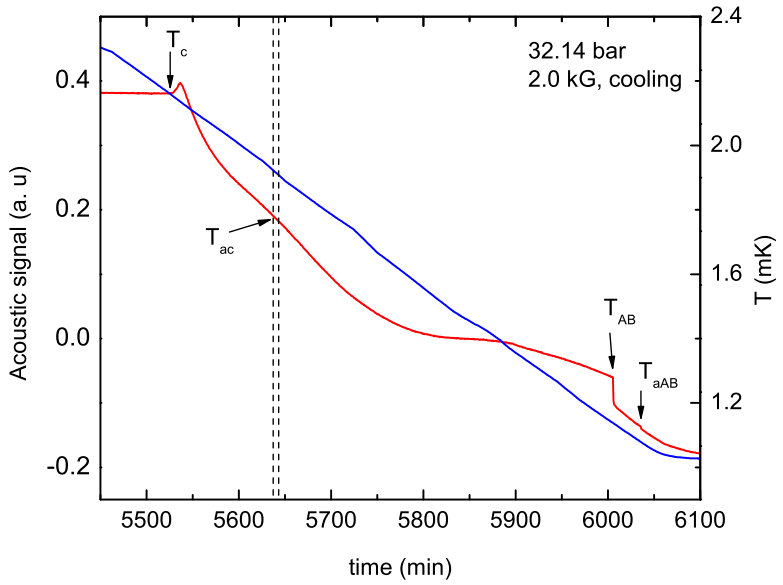

Figure 5-13. Acoustic response from ^{3}He in 5% compressed aerogel on cooling at 32 bar pressure in a field of 2 kG.

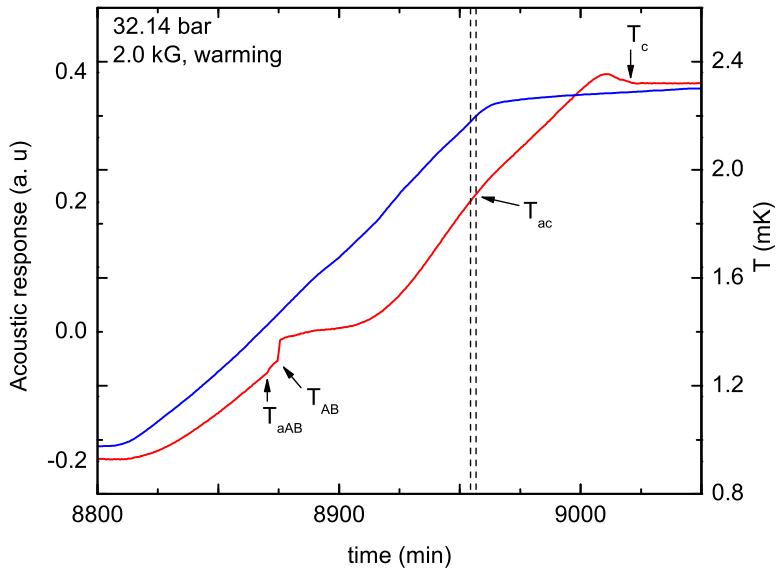

Figure 5-14. Acoustic response from ^{3}He in 5% compressed aerogel on warming at 32 bar pressure in a field of 2 kG.

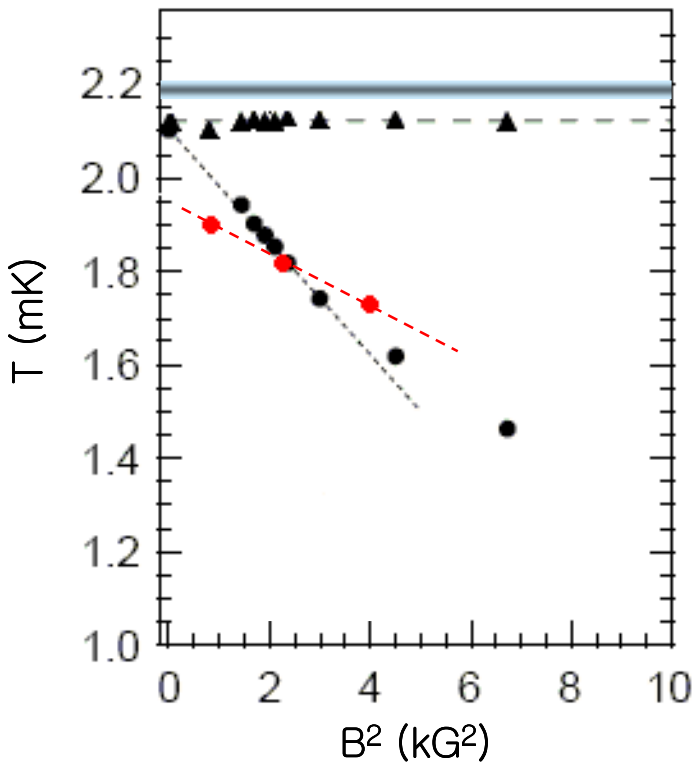

Figure 5-15. Plot showing the quadratic suppression of the A-B transition in low magnetic fields. Data in black circles and triangles are respectively, A-like to B-like transition and superfluid transition in uncompressed aerogel from Gervais [31]. The A-like to B-like transition in 5 % compressed aerogel is shown in red circles. Hazy blue line is our observed superfluid transition temperature in aerogel.

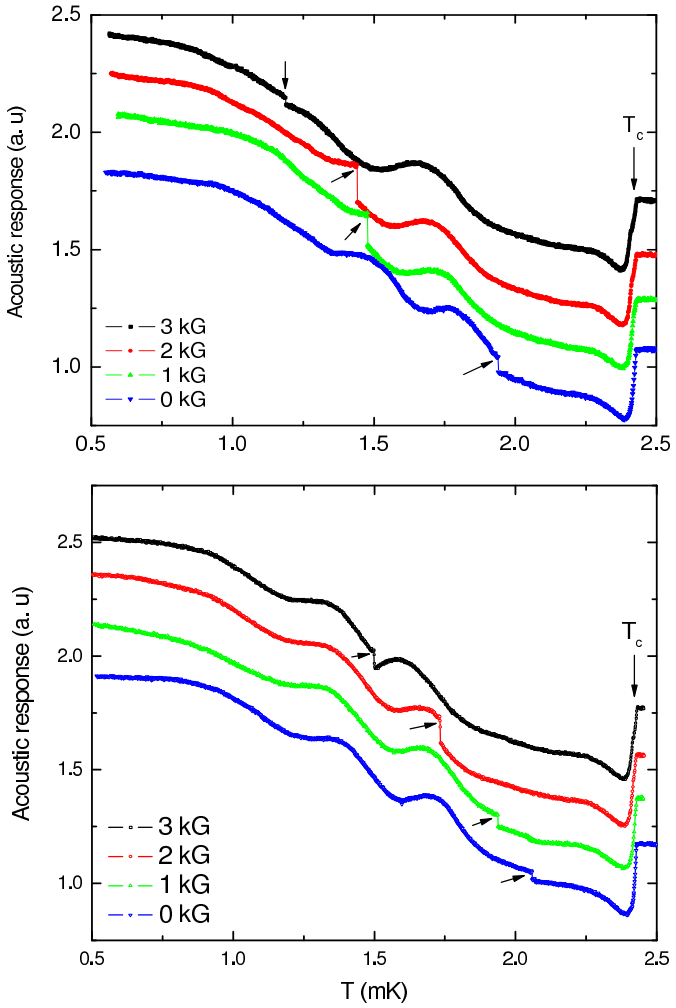

Figure 5-16. Acoustic response from ^{3}He in 10% compressed aerogel on cooling (top plot) and warming (lower plot) at 29 bar pressure in magnetic fields from 0 to 3 kG.

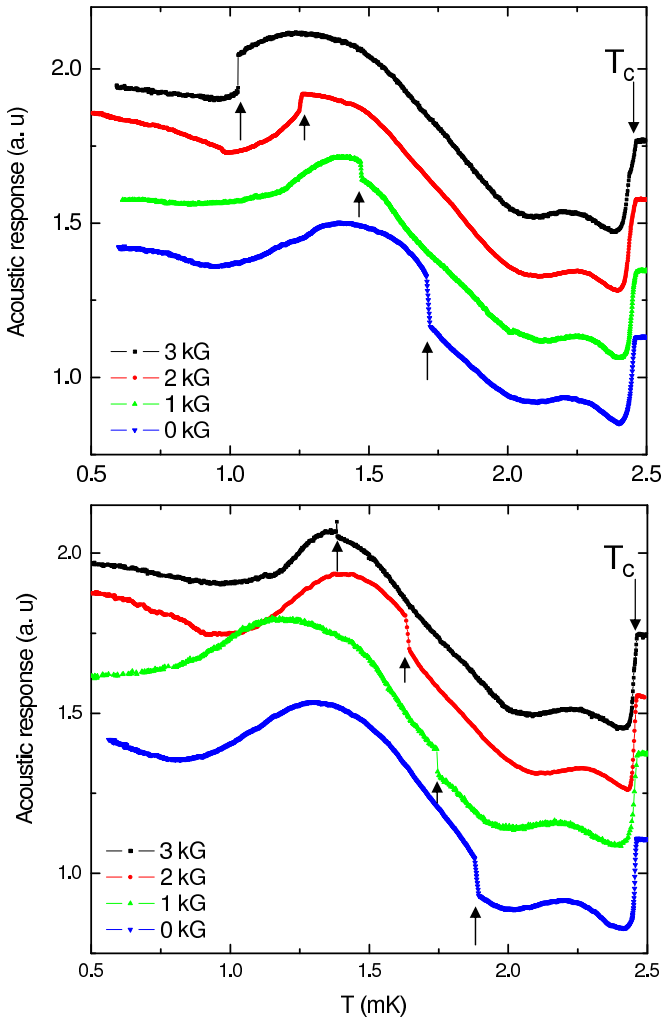

Figure 5-17. Acoustic response from ^{3}He in 10% compressed aerogel on cooling (top panel) and warming (lower panel) at 32 bar pressure in fields from 0 to 3 kG.

CHAPTER 6
CONCLUSION

An ultra low temperature cryostat is designed and implemented in this work to perform experiments at sub-millikelvin temperatures specifically aimed for measurements in superfluid ^{3}He. The cryostat is a combination of a dilution refrigerator (Oxford Kelvinox) with a base temperature of 5.2 mK and a 48 mole copper block as the adiabatic nuclear demagnetization stage with a lowest temperature of ≈ 200 μK.

To understand the effect of anisotropic scattering on the superfluid phases of ^{3}He in 98% porosity aerogel, we performed high frequency shear acoustic impedance measurements in superfluid ^{3}He in compressed aerogels. The experiments were done with aerogel cylinders immersed in liquid ^{3}He at pressures of 29 bar and 32 bar in magnetic fields up to 3 kG. The aerogel cylinder was compressed along the symmetry axis to generate global anisotropy. With 5% compression, we observe a supercooled A-like to B-like phase transition in aerogel in a wider temperature width than the width of the pure superfluid ^{3}He-A phase, while at 10% axial compression, the A-like to B-like transition is absent on cooling down to ≈ 300 μK in the absence of magnetic field and in magnetic fields up to 3 kG. This behavior is in contrast to that in ^{3}He in uncompressed aerogels, in which the supercooled A-like to B-like transitions have been identified by various experimental techniques. Our result is consistent with the theoretical predictions but requires further confirmation with measurements at different pressures. Since we found that the contact between the aerogel surface and the transducer in the transverse acoustic impedance measurements is important and the 10% compressed aerogel sample was found to be shrunk after warm up, future experiments should be done either with aerogels grown directly onto the transducer or the compression could be provided *in-situ*.

We obtained detailed quantitative results from the characterization of anisotropy in compressed aerogels using optical techniques at room temperature. Specifically, optical birefringence was measured in 98% porosity silica aerogel samples subjected to various

degrees of uniaxial compression up to 15% strain over a wide range of wavelength, 200 to 800 nm. Global anisotropy introduced by uniaxial strain on the aerogel produced birefringence (Δn) in the material. We observed a quasi-linear strain dependence in $\Delta n = n_e - n_o$ in compressed aerogels, where $n_{e(o)}$ is the index of refraction for the extraordinary (ordinary) ray of light which has its polarization parallel (perpendicular) to the compression axis. We demonstrated waveplate behavior of uniaxially compressed aerogels and proposed that this effect has potential applications for aerogels as tunable waveplates operating in a broad spectral range.

An important finding during the course of the experiments in 98% porosity aerogels was that they do not recover completely to their original length after decompression. A strain beyond 5% on the aerogels produced hysteresis in the transmittance spectra from aerogels on compression and decompression. This was accounted for by the observed shrinkage in their lengths. This significant amount of non-recovery of aerogels after decompression has to be borne in mind by experimenters studying the effects of global anisotropy in superfluid ^{3}He.

APPENDIX A
TRANSPORT MEASUREMENTS IN BILAYER MANGANITE FILMS

A.1 Introduction

Hole-doped manganites with the general formula, $RE_{1-x}AE_xMnO_3$ (RE = trivalent rare-earth cation such as La and AE = divalent alkaline-earth cation such as Ca), are well known for their colossal magnetoresistive property (CMR) and an insulator-to-metal transition [88, 89]. Extensive research is being conducted, not only to understand these materials at the fundamental level but also for their potential device applications [90]. Substrate induced strain interactions and quenched disorder introduced by direct chemical substitution have been found to drastically change the phase diagram [91]. Especially, manganites with cationic size disorder are known to phase separate into insulating and metallic ferromagnetic domains at low temperatures [92]. Recent transport measurements [93] on thin films of $(La_{1-x}Pr_x)_{0.67}Ca_{0.33}MnO_3$ revealed two mixed phase states, namely, the fluid phase separated (FPS) and the static phase separated (SPS) states, the SPS state appearing only above a Pr concentration of $x \geq 0.6$. These measurements were all done in the direction parallel to the plane of the thin film. In order to gain more complete understanding of the dynamics of these phase separated states, especially the effect of electric field on the SPS state which can be enhanced at lower temperatures, we conducted out-of-plane transport measurements down to ≈ 50 mK using a device fabricated out of a manganite bilayer film. This work is motivated by the measurements performed by Sung Hee Yun [94] in Prof. Biswas group.

The structure is composed of two thin films, a 26 nm-thick $(La_{0.4}Pr_{0.6})_{0.67}Ca_{0.33}MnO_3$ (LPCMO) layer deposited on top of a 60 nm-thick $La_{0.67}Ca_{0.33}MnO_3$ (LCMO) layer grown on an (110) $NdGaO_3$ (NGO) substrate. The resistance of this structure is measured from two gold electrodes deposited on top of the LPCMO film with the exposed LPCMO layer etched out by ion plasma etching technique. We observed an upturn in the resistance

below 30 K for various current excitations ranging from 0.2 to 100 μA. We report electric field dependence of the resistance of this structure.

A.2 Device Fabrication and Measurement Technique

The samples were grown epitaxially on an $NdGaO_3$ (NGO) (110) substrate, using pulsed laser deposition (PLD) technique [94]. An excimer laser of 248 nm wavelength provides an energy density of $\sim$1 J/cm^2 on the target surface. The thickness of the samples was controlled by the deposition time and the laser firing frequency of 5 Hz, corresponding to a sample growth rate of 0.06 nm/s. The film was deposited at 820°C in an oxygen atmosphere of 440 mtorr to prevent the loss of oxygen from the substrate and to provide ambient oxygen pressure during deposition. After completion of the thin film growth, oxygen was controlled in a post deposition annealing process until the temperature decreased to approximately 25°C with a cooling rate of 20°C/min. These growing conditions are selected to produce a sharp insulator-to-metal transition at a temperature close to the transition in bulk samples with the same composition. First, a 60 nm-thick $La_{0.67}Ca_{0.33}MnO_3$ (LCMO) film was grown directly on the NGO substrate. And then a 26.5 nm-thick $(La_{0.4}Pr_{0.6})_{0.67}Ca_{0.33}MnO_3$ (LPCMO) film was grown on top of the LCMO film. Deposited on the LPCMO film were two micrometer-thick gold contact pads (approximately 1 x 2 mm^2) which served as electrical contacts for measurements and also as a mask during the etching process (see inset (a) of Figure A-1). The LPCMO film exposed (not covered by the gold pads) was then removed by Ar ion plasma etching technique using the Unaxis Shuttlelock RIE/ICP (Reactive Ion Etcher with Inductively Coupled Plasma Module). During the process, the Ar pressure was kept at 5 mtorr and the flow rate at 20 sccm.

The resistance of the sample was measured by a standard 4-wire method using a constant current source ranging from 0.2 to 500 μA. This configuration is expected to measure the out-of-plane resistance of the LPCMO film. The measurements were conducted in two different set-ups. From 300 K to 10 K samples were vapor cooled using

a variable temperature insert. Below 1 K the measurement was done using a dilution refrigerator down to 50 mK. The sample was thermally attached to the gold-plated Cu cold-finger extended from the mixing chamber of a dilution refrigerator. All the measurement wires were also thermally anchored to the cold finger. Temperature was determined by a calibrated RuO_2 thermometer in this range.

A.3 Results

Figure A-1 shows the resistance versus temperature curves on cooling and warming for the as-grown sample (inset (a)) and the etched sample (inset (b)). The R vs. T curves show two distinct insulator-metal transitions corresponding to LCMO around 250 K and LPCMO with its characteristic hysteresis on warming and cooling around 110 K. The resistance curve of the etched sample still shows the two distinct insulator-metal transitions corresponding to LCMO and the hysteretic feature from the LPCMO film. However, the resistance is higher due to the reduction in the cross sectional area for current path. Figure A-2 shows the current dependence of the R vs. T curve for this etched double compound layer of LPCMO on LCMO. We observe two interesting regions in the current dependence of the resistance. Firstly, around the temperature region where hysteresis is seen in the R vs. T curves, an insulator-metal transition induced by the current (or electric field) is observed and is shown in detail in the bottom inset of Figure A-2. As the current is increased from 100 to 500 μA the temperature dependence of the resistance for the cooling curves changes from insulator-like to metal-like, or in other words, the insulator-metal transition is shifted to higher temperatures due to the metallic domains percolating along the out-of-plane direction in the LPCMO layer. This electric field induced percolation was also observed in the transport measurements in the parallel direction of the LPCMO thin film [93]. Secondly, in the low temperature region below 30 K, as shown in the top inset of the Figure A-2, we observe an upturn in the resistance as temperature was lowered. This upturn is more pronounced for smaller applied current.

To further investigate the electric field dependence of the upturn in resistance and its effect on the SPS state we measured the resistance down to lowest temperature of 50 mK. This measurement would also eliminate the possibility of any heating effect as the origin of the current dependent resistance upturn. The R vs. T in the low temperature region is shown in Figure A-3 for various applied currents ranging from 0.2 to 100 μA. The upturn in resistance was observed for all applied currents although it is not visible for 10 μA and 100 μA in this scale. We can distinguish the heating effect from these curves, which show a plateau in the resistance below 100 mK, which is clearly different from the reduction of the upturn. The origin of this upturn is probably related to the presence of disorder in the LPCMO film since we observe this kind of upturn in single layer thin films of LPCMO as shown in Figure A-5 but not in LCMO films. We measured magneto-resistance of the bilayer structure. This is shown in Figure A-4. The normalized resistance as a function of magnetic field varying from -1 tesla to 1 tesla is plotted, which indicates a negative magneto-resistance in the upturn region.

A.4 Summary

We studied transport properties in the out-of-plane direction of the LPCMO thin film using a double compound layered manganite structure. We observed an upturn in the resistance of this structure at low temperatures and found that the upturn and its electric field dependance persist down to 50 mK. This behavior arises from either disorder in the LPCMO film or the interface between the LPCMO and LCMO films. The structure is also found to exhibit negative magneto-resistance. Further investigations are necessary to understand the underlying mechanism.

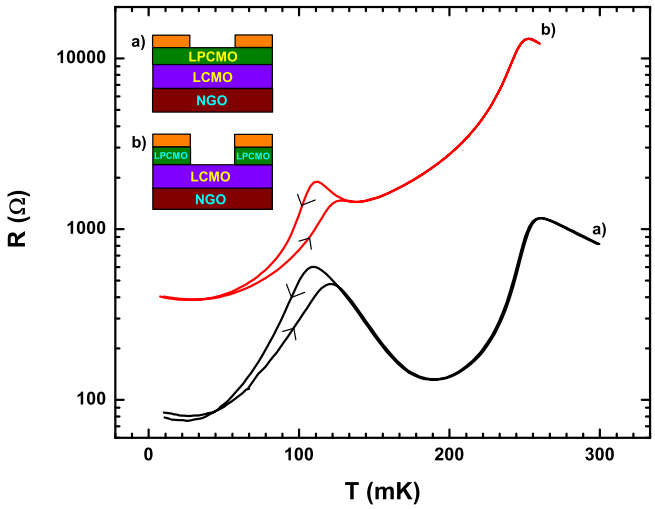

Figure A-1. Resistance vs. temperature for the bilayer structure (black/bottom trace) and etched bilayer structure (red/top trace). Arrows mark the cooling and the warming traces. The schematic structures of the bilayer (a) and the etched bilayer (b) samples are shown in inset.

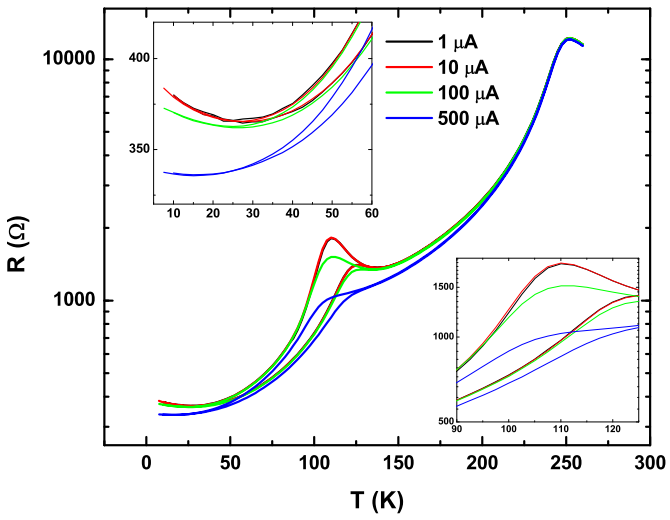

Figure A-2. R vs. T for the etched double layered structure for applied currents from 1 μA to 500 μA. Top inset shows the close-up of the low temperature upturn in resistance and bottom inset shows the close-up near the current-induced insulator metal transition.

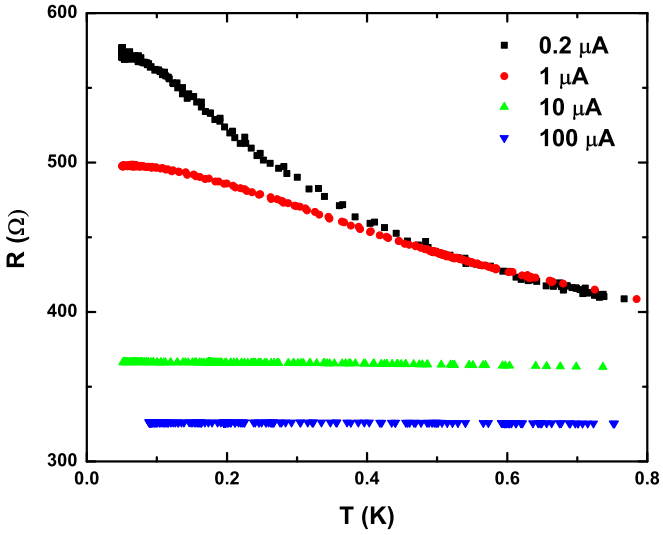

Figure A-3. Low temperature current dependance of the upturn in resistance of the double layered structure. Upturn in resistance is not visible for 10 μA and 100 μA applied currents in this scale.

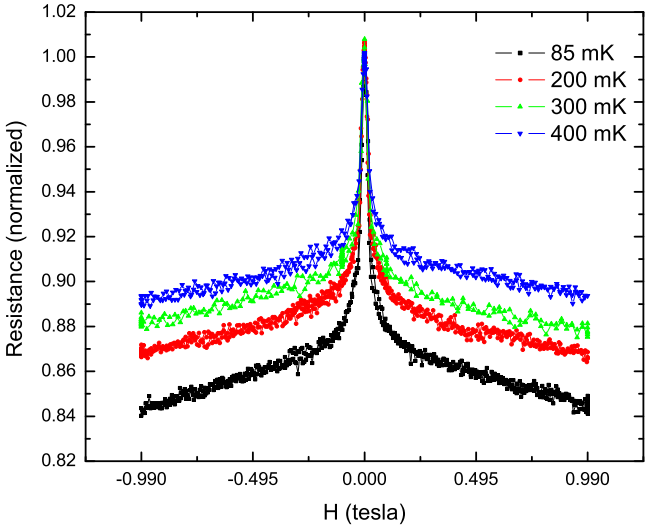

Figure A-4. Low temperature magneto-resistance of the double layered structure.

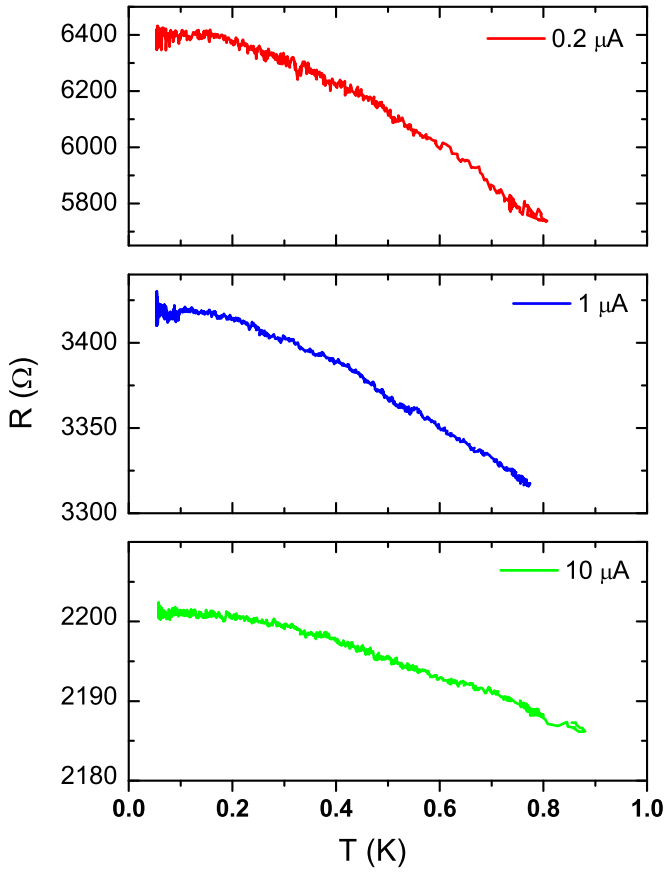

Figure A-5. Low temperature R vs. T upturns in the thin film of LPCMO manganite at different current excitations. No upturn is observed for LCMO film within the temperature range shown here.

APPENDIX B
OPERATION OF THE CRYOSTAT

The following pages describe the protocol for the operation of the cryostat. For a general overview of the Kelvinox 400 dilution refrigerator system the user should refer to the Oxford's handbook while the physics of dilution and nuclear refrigeration techniques are thoroughly described in various excellent texts [46, 48, 95].

B.1 Assembling

After the experimental cell is attached to the nuclear stage and before closing the cryostat, a complete electrical check should be performed on all electrical connections. Check the resistance of the 1K pot, sorb, still and mixing chamber resistors and heaters from the Fisher connector on top of the cryostat. Refer to Table B-1 for the resistance values at room temperature. Check for any shorts to ground.

Mounting the shield and IVC: Mount the radiation shield at the Still plate using 5.5 mm wrench to tighten the screws. There are four Vespel (SP22) spacers screwed at the bottom of the CDS at the four corners to ensure that there are no touches between the CDS and the shield. However, the bottom cap of the shield can be removed and a visual inspection can be made using a flashlight. The cap has a Teflon spacer attched to it that prevents the inside of the IVC from touching the shield. Next, clean the indium seal area on top of the inner vacuum can (IVC) and below the 4K flange on the insert with Q-tips or Kimwipes and methanol. Do not use tweezers or any sharp metal objects that can cause permanent scratches. Indium wires with 1/16" or 1/32" diameter have worked well for this IVC seal. Apply vacuum grease to the indium wire and wrap it around the lip of the IVC so that the ends overlap. Carefully raise the IVC up while watching out for any obstructions especially from the 1K pot pick-up line and the condenser line. If you are doing this for the first time, using a lab jack and a stool underneath the IVC will help to raise the IVC slowly when the IVC nears the 4K flange. Tighten the screws uniformly around the 4K flange using 5/32 ball head hex wrench and start pumping the IVC using

the Turbo pump. After pumping for about an hour, the screws can be re-tightened. The can is typically pumped overnight after which the pressure drops down to about 5 mtorr and it is then leak checked from the outside by spraying Helium gas around the various vacuum ports on the top plate and the IVC indium seal. One can now fill liquid nitrogen (LN2) into the LN2 trap and start circulating the ^{3}He/^{4}He mixture (mix) that is present at the back of the ^{3}He pump (there is no need to open the dump tank) while looking at the IVC for the background leak rate in either ^{3}He or ^{4}He mode. In order to do so, turn on the ^{3}He pump and open valves 6, 13A, 12A, 1 on the IGH, the gate valve on the still line (see Figure 3-6) and the manual valve on the condenser line after the LHe cold trap. The mix can be left circulating for a day or two until the start of the leak checking procedure.

Installing the magnet: First, attach the two aluminum collars (magnet arms) in positions labeled 'A' and 'B' on the magnet support ring for raising the magnet (the screws go from the bottom). Then attach the pulley cables at the two ends of the magnet arms and the counter weights at the other ends of the pulley cable (1.5 lead bricks on each side with each brick weighing about 20 lb). Let down the weights slowly into the pit. This will counter balance the magnet which can then be easily raised up by pulling on the two sides of the cables simultaneously. Raise the magnet and tighten the nuts at the three threaded brass studs emerging from the magnet support rings and the G10 support rods on the insert. Use a 11 mm wrench for the nuts on side 'A' and a 7/16 socket wrench for the nut on 'B' side of the collar. When sliding the magnet up around the IVC, the 1K pot pickup and condenser lines have to be pushed in a little to make way for the magnet.

One may need to guide the threaded screws into the holes of the magnet support ring supported form the G10 rods. Now, connect the pin connectors for the bath resistors, heater, and the magnet (Fischer) connector. Attach the LHe level monitor stick by sliding the ring-nut clamp around the level meter stick and tighten at the marked position on top of the magnet support ring. This ensures the bottom of the stick does not hit the

bottom of the dewar but lies about an inch from it. Connect LHe pin connector to the connector that is present on top of the last baffle. Use aluminum or scotch tape to affix the level meter stick at various places along the length of the magnet. This is a good time to lower the LHe cold trap, the LHe transfer line and the 8 tesla and 2 tesla vapor cooled magnet leads from above the top plate of the cryostat. The LHe cold trap should pass smoothly all the way down through the various brass guiding cones glued on the baffles, the G10 tube and the magnet support ring. The stainless steel LHe transfer tube stops at the magnet ring where it can be screwed into the threaded brass cone attached to the magnet ring. The bottom of the transfer tube is about 2" above the bottom of the dewar. A rubber hose about 2.5" long is snugly fit around the bottom of the tube and twisted with a copper wire at an angle so that when the dewar is raised up, the rubber hose can graze the bottom of the dewar. Once the magnet is securely fixed along with the various electrical connectors mentioned above, check all the wiring for continuity and shorts to ground through the intermediate measurement box (IMB). The magnet voltage tap resistance values for 8 tesla (8T) and 2 tesla (2T) magnets should be about 25 Ω between pins 11-12 from the cinch connector on the IMB (see Table 3-3) and the persistent switch heater pins 9-10 should have a resistances of 71 Ω and 76 Ω for 8T and 2T magnets, respectively. At 4 K, the magnet leads should have a resistance below 0.5 Ω between them. The 8T magnet has been safely operated even with a possible 4-5 MΩ short to the ground from each lead. Once all the connections have been checked, the counter weights hanging inside the pit can be removed and the magnet arms detached.

Finally, one has to lie down under the cryostat and check for the centering of the IVC and the Magnet. Usually, the IVC is slightly off-centered if one looks from below the magnet. By slightly adjusting the screws at the magnet support ring, one can adjust the center of the Magnet to align with the center of the IVC. Less than 1/4 turn on all the screws is enough to perform this adjustment.

Raising the dewar: Clean the o-ring surfaces on the dewar and the underside of the top plate with Kimwipes and methanol and apply vacuum grease to the rubber o-ring. Change the counter weights to 6 blocks ($\approx$ 120 lb on each side) on the pulley cables and lower the weights slowly into the pit. The dewar can be raised up by pulling on the cables. Before this, the LHe cold trap needs to be pulled up a little since it may hit the bottom of the dewar belly while raising the dewar (since the LHe cold trap stick is not perfectly straight). Once the dewar is all the way up, the cold trap stick can be pushed back in. Tighten the nuts with washers onto the threaded stainless steel studs emerging form the dewar and the top plate using 9/16 wrench or an adjustable wrench. Finally, whenever raising or lowering the dewar (or the shield and IVC), watch out for obstructions. If you feel even a slightest of resistance, stop pulling. Before every cool down, the vacuum jacket of the dewar has to be pumped using the turbo pump for at least a day. To do so, first pump on the pumping line between the turbo pump and the bellows sealed valve on the dewar jacket to high vacuum and then open the valve slowly to pump on the jacket. The dewar bath space and 1K pot can be pumped through the auxiliary pumping panel on the IGH (see Figure 3-6) using the ^{4}He pump (pot pump). The pressure is monitored at the pressure gauge on top of the cryostat and the gauge P2 on IGH. After pumping the dewar bath space overnight, P2 should typically fall below 0.2 mbar.

B.2 Leak Detecting Procedure

^{4}He leak checks are performed on the bath, IVC, dilution and 1K pot while ^{3}He leak checks are performed for the sample cell and melting curve thermometer (MCT). The turbo pump and the leak detector (Spectron 600T, Edwards) are hooked up to the IVC while either ^{3}He or ^{4}He gas is introduced into the various chambers of the cryostat. Before starting to leak check, the mix circulation is stopped by closing valve 13A and opening valves 5 and 9. The mix is returned to the dump tank by opening the manual dump valve and the pressure at G2 is checked against the previous recorded value. The dump pressure can vary with the changes in the room temperature and should be between 816-830 mbar.

Once all the mix is back to the dump, start with all the valves on the IGH closed and clean the LN2 trap by opening valves 11A, 2 and 7, monitoring pressure at G1. G1 should be showing zero pressure with the trap still in the liquid and if all the mix was returned to the dump tank. If not re-circulate and collect the gas back to the dump. The trap is taken out of the LN2 and heated with a heat gun until it is hot to the touch. The dirty gas is pumped out using the utility pump that is connected to the vent at the back side of the IGH. Now the 1K pot can be pressurized to 1 bar of ^{4}He gas using the utility gas panel while watching the leak detector on the IVC. If there is no leak, the pot needle valve is opened to see if the ^{4}He bleeds into the bath (since the bath is at vacuum). After checking to see if the needle valve opens, one can now fill the bath with ^{4}He gas close to 1 bar. There should not be any leak into IVC. The bath is then flushed with nitrogen gas and kept pumping overnight. Do not leave any ^{4}He gas in the bath for too long as it can diffuse into the fiberglass inner wall of the dewar. Once the IVC is leak tight from the bath space and the 1K pot, the mixing chamber is leak checked by introducing ^{4}He gas through the vent behind the IGH and opening valves 7, 2, 1 on the IGH and the cross-over valve located behind the IGH (see Figure 3-6). It can be pressurized close to 1 bar on G1. The gas thus introduced can be pumped out by the ^{4}He pump by opening valves 5A and 2A. This completes the ^{4}He leak checks.

Dilution and 1K pot throughput tests: The dilution and 1K pot leak checks can be performed together with the throughput tests described in the section 4.2.3 of the Oxford manual. During the dilution unit throughput test, the pressure on G1 should rise at a rate of $\approx$ 20-30 mbar/min at room temperature and by about 80 mbar/min at LN2 temperature. Similarly, the 1K pot throughput test can also be performed by filling the bath to 1 bar ^{4}He and opening the needle vale to 50%. The pressure on G3 should rise by about 25 mbar in 15 s once the needle valve is completely open by 50% at room temperature. Since it has been found that the 1K pot needle valve leaks, the pressure rise could actually be a little faster. So, at LN2 temperature, the pot should always be

pressurized with ^{4}He, since we do not want any nitrogen gas from the LN2 transfer to get into the pot. In this case, after pressurizing the pot to 1 bar and opening the needle valve to 50%, the pressure drops by about 100 mbar in 35-40 s.

The leak detector is switched to ^{3}He mode to leak check the experimental cell and the MCT. ^{4}He or ^{3}He modes can be chosen by opening the back panel of the leak checker and pressing on the standby mode button on the circuit board inside and switching to either ^{4}He or ^{3}He option on the front panel. Actually, the experimental cell and the MCT can be leak checked at room temperature even before raising the magnet and the dewar. In case a leak is found, one can save some time and effort spent in lowering the dewar, the IVC and the shield to fix the leak. If the experimental cell is made out of polycarbonate material, as was the case with all the experiments performed so far, the cell need only be pressurized to about 30-40 psi of ^{3}He slowly, after which we can observe diffusion signal from the plastic (see the chart recorder traces from the leak detector available in the lab note book). The leak rate decreases slowly after pumping out the cell. It takes a long pumping time ($\approx$ a day) to get the ^{3}He background signal in the IVC down to the 10^{-8} level after leak checking the polycarbonate cell. So, it is recommended that the MCT be leak checked before leak checking the cell. At room temperature, the MCT is typically pressurized up to 300 psi through the LN2 cold trap and the charcoal dipstick on the ^{3}He gas handling system.

In all leak checking and transferring procedures involving ^{4}He we use the two utility gas handling panels labeled GHP1 and GHP2 whereas for ^{3}He, we use the ^{3}He gas handling system described in chapter 3. GHP1 has high pressure cylinders of nitrogen and helium gases connected to it. These gases can be routed to GHP2. GHP2 is used for leak checking during cool down and also for back filling the pot with ^{4}He gas during helium transfer. It is also used to pressurize the bath, IVC, or the 1K pot with the appropriate type of gas. This panel has a connection to a low purity ^{3}He gas tank that is used as exchange gas for nitrogen and helium transfers. GHP1 has copper tubing extending all

the way up to the ceiling and connected to a spiral plastic tubing that can be used to pressurize the helium dewar while transferring. It also has separate connections from the nitrogen gas cylinder to pressurize the TMC gimbal piston isolators for floating the cryostat. A small utility pump is connected between the two panels for evacuating the panels during various cycles of operation. This pump is also used for cleaning the LN2 and LHe traps.

B.3 Cooling Down

Liquid nitrogen transfer: We are ready to transfer LN2 into the dewar bath space, once all the room temperature electrical and leak detecting procedures are done. At this stage, the IVC and the bath should be in vacuum and the mix should be circulating in the dilution. Typically IVC pressure is below 5 mtorr and the bath space should be below 0.2 mbar (P2). An important step to be remembered here is to flush the 1K pot with ^{4}He gas and leave it pressurized to 1 bar (G3). The needle valve is not perfectly leak tight even when its completely closed, so some gas will bleed into the bath space which is ok. But, we do not want any nitrogen gas or air to enter the 1K pot during LN2 transfer which can later freeze the needle valve during LHe transfer. So, the pot is always kept pressurized with ^{4}He gas (from GHP2) until we start transferring LHe. Now, start by closing the valve between the turbo pump and the IVC (stop pumping). Introduce ^{3}He exchange (about 2 shots) from the low purity ^{3}He tank on GHP2. Bring the exchange gas pressure between 750-800 mtorr in the IVC. Next flush and fill the bath with nitrogen gas and start transferring LN2 form the dewar through the LN2 blow out tube. Remember to disconnect the ^{4}He recovery line and leave it open as a vent for the nitrogen vapor. Monitor the bath resistors at IMB while transferring LN2 and stop transfer when the level is near the middle of the dewar belly. You can stop transfer when the resistors show the values, R1 = 750 Ω (not in liquid), R2 = 1010 Ω (in liquid), and R3 = 1095 Ω (in liquid). This should take about 80 liters of LN2. After finishing transfer, put a check valve on the venting port or simply cover it with a loose tape. Precool overnight or at least for about

7 hours. The sorb thermometer should go down to about 92 K overnight while the IVC pressure saturates around 250 mtorr. At LN2 temperatures, check the various electrical connections.

Leak testing after liquid nitrogen transfer: Before blowing out the LN2 form the bath, the MCT and the cell have to be leak checked. Start by pumping on the IVC exchange gas. It takes about an hour to get the ^{3}He background in the IVC within the 10^{-8} cc/s range. The MCT has to be leak tight up to 500 psi. When the cell is cold there is no diffusion signal observed and so it has to be leak tight at high pressures too ($\approx$ 450 psi). Once they are leak tight, blow out the LN2 by pressurizing the bath ($\approx$ 4 psi) with ^{4}He gas from GHP2. Collect the LN2 that is oozing out from the transfer tube through the rubber hose into a smaller dewar. Once all the liquid is out, the bath resistor (R3) at the bottom of the dewar should be showing a resistance value below 1095 Ω. Also, when pumping on the bath, if the pressure gauge for the bath on the top plate does not go below 20-25 inches, it means we have LN2 left in the dewar. Once all the LN2 is out, pump on the bath and flush it with ^{4}He gas couple of times. During this time, there should not be any leak signal from the IVC. Flush the pot with ^{4}He gas and check if the needle valve opens. It has been found to get stuck when it is cold. One has to remove the cover on the needle valve on top of the insert and slightly twist the brass base in the anti-clock wise direction. This should set the needle valve back in motion. Once the leak detecting procedures and the throughput tests on 1K pot and the dilution are finished, the bath is ready for LHe transfer. Start recirculation of the mix in the dilution. Remember, use only the mix that is present in the pumping line in the back of the pump. Do not open the dump tank yet.

Liquid helium transfer: Add ^{3}He exchange gas (about 3 shots) to the IVC to a pressure of $\approx$ 500-550 mtorr. Reconnect the ^{4}He recovery line. Remove the LN2 blow out tube and insert the LHe transfer stick in its place. The LHe transfer stick has a thinner lower section that has to be screwed into a thicker L-shaped section with a vacuum jacket.

If it is straight and not bent, it should fall straight onto the cone socket on the magnet support ring. Before transfer, put a small weight on top of the bath relief valve and open the recovery line completely. Transfer relatively slow for the first transfer maintaining the pressure on the transfer dewar at 20 inches. Check to see if the needle valve opens and the 1 K pot fills durig the transfer, but do not run the pot yet. Pump on the IVC when the liquid level is about 25% or when the IVC pressure is around 100 mtorr. Simultaneously, heat the sorb by applying a power of about 200 mW from the IGH (for about 15 min). The complete transfer takes about 120-130 liters of LHe. It is best to leave the full transfer stick in the bath during the first transfer until the bath is full. Afterwards, the thinner lower section of the stick can be removed to avoid any Taconic vibrations.

Condensing sample gas: Once the temperature of the mixing chamber stabilizes around 4.2 K, pressurize the experimental cell with ^{3}He hypercritically if the cell contains aerogel. The high purity ^{3}He storage tanks have a total pressure of 35 psi. One of the ^{3}He tanks pressure can be released into the experimental cell and MCT together slowly at 4.2 K and left open to the tank during cool down to 1 K. This will maintain a pressure that is always higher than the critical point of ^{3}He avoiding the formation of a liquid-vapor interface which can damage the aerogel inside the cell. With the sample cell constantly pressurized form the tank, fill the 1K pot by opening the needle valve completely and slowly closing it down to 10-15% and while pumping on it through the pot pump with the valve 4A open. Remember to change the pot pump exhaust to the helium recovery line. At this stage, we are still circulating only the small amount of mix that is present at the back of the ^{3}He pump. Once the pot cools down to around 1.5 K, the mixing chamber temperature also falls and should stabilize around 1 K. Now, its time to calibrate the MCT as described in chapter 3. A typical pressure vs. ratio curve of the MCT (a) (see Figure 3-18) at 1 K is shown in Figure B-1. Allowing sufficient time ($\approx$ 5min) for the MCT to equilibrate at each pressure, about 35-40 data points are taken within the pressure range 400-500 psi. Once the calibration curve is obtained, the pressure

in the MCT is fixed at a high pressure of 500 psi and the valve to the MCT on the top plate of the cryostat is sealed. We then proceed to pressurize the experimental cell to the required amount. While doing this, we can simultaneously condense more mix from the dump.

Running the dilution to base temperature: Let the mix out of the dump by slowly cracking open the manual dump valve 9. Watch out for the pot while condensing the mix. In takes about 2.5 hours in order to condense all the mix from the dump. The heat switch is then closed applying a current of 730 mA through the low noise magnet power supply. The still power can also be raised slowly from 0 to 4 mW and the roots blower pump is turned on. It takes almost one full day to reach the base temperature of 5.2 mK. Typical pressures at the base temperature are G1 = 120 mbar, G2 = 150 mbar and P1 = 0.2 mbar.

Precooling: Once the base temperature is reached, the 8 tesla demagnetization magnet is charged to a high field of 7-8 tesla at a rate of $\approx$ 1-5 mA/s. At high field, the magnet is put into persistent mode and the leads can be lifted to reduce boil-off. Typical precooling curves are described in Figure 3-20. I would like to mention two points in using the AMI magnet power supply programmer and the power supply. *First, never turn on the power supply without the programmer turned on first. Secondly, if you want change to the 2 tesla magnet, the appropriate cable behind the IMB has to be changed too without which you would surely quench the magnet.*

Demagnetization: After precool, demagnetization (demag) is first done at a faster rate of a about 2 mA/s down to about 3 mK and then at a slower rate of 0.2 mA/s. The fast demag is performed for about 2 hours with the heat switch closed. It is usually opened around 8 mK or so. After which the demag is stopped around a temperature of $\approx$ 3 mK for couple of hours to allow for thermal equilibrium to be reached between the various parts of the nuclear stage. See chapter 3 for the performance characteristics of the nuclear stage.

B.4 Warming Up

First of all, zero the magnetic field in the 8 tesla and 2 tesla magnets. This would slowly warm the nuclear stage to around 3 mK. Close the heat switch and start pumping the mix to the dump by first closing valve 13A (stop circulation) and opening valve 9 on the dump. Slowly release the pressure in the cell and the MCT to the storage tanks and leave them open to the tanks all the way up to 4 K. Remember that one has to unload the aerogel cell hypercritically. So, do not use dipstick on the cell until the temperature is around 4 K. Heat the mixing chamber and the still until most of the mix is recovered to the dump. Stop pumping the pot and open the helium recovery line all the way. One can use the bath heater to expedite the helium boil off. At 4 K suck out all the ^{3}He gas from the cell and MCT using the dipstick. During cool down, the LHe trap needs cleaning about every 2 weeks at which time one can simultaneously clean the LN2 trap as well. Also, after warming up the fridge, clean the LN2 and LHe cold traps once again.

Note on cleaning the LHe trap: If the LHe trap has to be cleaned when the fridge is cold and the magnet is charged, certain precautions have to be taken especially while pushing the trap back into the insert. First stop circulation by closing valve 13A on IGH and collect the mix that is present in the LN2 and LHe traps by closing the return line manual valve after the LHe trap on top of the cryostat. Pump on the traps for about 5-10 min and and close valve 5 and valve 12A (valve on LN2 trap). Now G1 should be showing zero pressure. First clean the LHe trap by slowly raising it up from the insert. G1 should start showing some pressure as you raise the LHe stick outside the cryostat. You can stop raising the trap further when you see the red demarcation line marked on the trap. Warm the stick to room temperature while pumping on it using the utility pump through valve 2, 7 and the vent valve behind the IGH. Pump on it until the pressure is below 300 mtorr as seen from the gauge on GHP1. You can also clean the LN2 trap by closing valve 1, taking the LN2 trap out and pumping through valve 11A, 2 and 7. Once the traps are clean, first open the helium recovery (by-pass) line by about 50% and start

pushing the LHe trap in slowly. One can see the recovery pressure going up (from the flow meter) since we are boiling the helium in the bath with the warm LHe trap. Once the stick is all the way in, close the by-pass recovery line and restart circulation. Refer to the Oxford manual for further details.

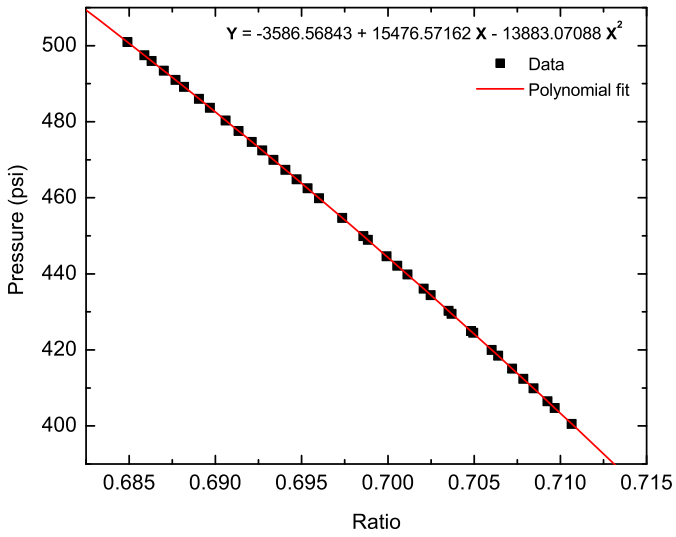

Figure B-1. Typical calibration curve of the MCT at 1K.

Table B-1. Fischer pin connector assignment on top of the cryostat. The resistance values are all two wire measurements at room temperature.

Pins	Resistance (Ω)	Sensor
3-18	2443	1K pot I+, IGH common I-
4-17	2443	1K pot V+, IGH common V-
1-18	529.7	Sorb I+, IGH common I-
2-17	529.7	Sorb V+, IGH common V-
5-16	2480	Still I+, I-
6-15	2480	Still V+, V-
7-10	2514	Cold plate I+, I-
8-9	2514	Cold plate V+, V-
11-12	366.7	Femtopower I+, I-
13-14	366.7	Femtopower V+, V-
19-20	77.8	Sorb heater
21-22	552	Still heater
23-24	627	Mixing chamber heater

REFERENCES

[1] A. J. Leggett, Rev. Mod. Phys. **47**, 331 (1975).

[2] D. Vollhardt and P. Wolfle, *The Superfluid Phases of Helium 3* (Taylor and Francis, London, 1990).

[3] G. E. Volovik, *The Universe in a Helium Droplet* (Clarendon Press, Oxford, 2003).

[4] L. D. Landau, Sov. Phys. JETP **3**, 920 (1957).

[5] L. D. Landau, Sov. Phys. JETP **5**, 101 (1957).

[6] W. R. Abel, A. C. Anderson, and J. C. Wheatley, Phys. Rev. Lett. **17**, 74 (1966).

[7] P. R. Roach and J. B. Ketterson, Phys. Rev. Lett. **36**, 736 (1976).

[8] W. P. Halperin and E. Varoquaux, *Helium Three* (Elsevier, Amsterdam, 1990).

[9] S. Kalbfeld, D. M. Kucera, and J. B. Ketterson, Phys. Rev. Lett. **71**, 2264 (1993).

[10] Y. Lee, T. M. Haard, J. A. Sauls, and W. P. Halperin, Nature **400**, 431 (1999).

[11] R. Balian and N. R. Werthamer, Phys. Rev. **131**, 1553 (1963).

[12] P. W. Anderson and P. Morel, Phys. Rev. **123**, 1911 (1961).

[13] P. W. Anderson and W. F. Brinkman, Phys. Rev. Lett. **30**, 1108 (1973).

[14] A. Yamaguchi, S. Kobayashi, H. Ishimoto, and H. Kojima, Nature **444**, 909 (2006).

[15] G. Volovik, ^{3}He phase diagram from http://ltl.tkk.fi/research/theory/he3.html (Retrieved March 1, 2009).

[16] T. M. Haard, *NMR Study of the Magnetization of Superfluid ^{3}He-B and NMR of Superfluid ^{3}He in Aerogel* (PhD thesis, Northwestern University, 2001).

[17] J. V. Porto and J. M. Parpia, Phys. Rev. B **59**, 14583 (1998).

[18] J. Pollanen, K. R. Shirer, S. Blinstein, J. P. Davis, H. Choi, T. M. Lippman, W. P. Halperin, and L. B. Lurio, J. Non-Crys. Solids **354**, 4668 (2008).

[19] J. V. Porto and J. M. Parpia, Phys. Rev. Lett. **74**, 4667 (1995).

[20] D. T. Sprague, T. M. Haard, J. B. Kycia, M. R. Rand, Y. Lee, P. J. Hamot, and W. P. Halperin, Phys. Rev. Lett. **75**, 661 (1995).

[21] J. A. Sauls and P. Sharma, Phys. Rev. B **68**, 224502 (2003).

[22] K. Matsumoto, J. V. Porto, L. Pollack, E. N. Smith, T. L. Ho, and J. M. Parpia, Phys. Rev. Lett. **79**, 253 (1997).

[23] E. V. Thuneberg, S. K. Yip, M. Fogelstrom, and J. A. Sauls, Phys. Rev. Lett. **80**, 2861 (1998).

[24] N. D. Mermin and C. Stare, Phys. Rev. Lett. **30**, 1135 (1973).

[25] A. A. Abrikosov and L. P. Gorkov, Sov. Phys. JETP **12**, 1243 (1961).

[26] A. I. Larkin, JETP Lett. **2**, 130 (1965).

[27] D. T. Sprague, T. M. Haard, J. B. Kycia, M. R. Rand, Y. Lee, P. J. Hamot, and W. P. Halperin, Phys. Rev. Lett. **77**, 4568 (1996).

[28] J. A. Sauls, E. V. Thuneberg, and S. K. Yip (unpublished).

[29] I. Fomin, J. Low Temp. Phys. **134**, 769 (2004).

[30] D. Rainer and M. Vuorio, J. Phys. C **10**, 3093 (1977).

[31] G. Gervais, K. Yawata, N. Mulders, and W. P. Halperin, Phys. Rev. B **66**, 054528 (2002).

[32] P. Brussaard, S. N. Fisher, A. M. Guenault, A. J. Hale, N. Mulders, and G. R. Pickett, Phys. Rev. Lett. **86**, 4580 (2001).

[33] H. C. Choi, A. J. Gray, C. L. Vicente, J. S. Xia, G. Gervais, W. P. Halperin, N. Mulders, and Y. Lee, Phys. Rev. Lett. **93**, 145302 (2004).

[34] J. E. Baumgardner, Y. Lee, D. D. Osheroff, L. W. Hrubesh, and J. F. Poco, Phys. Rev. Lett. **93**, 055301 (2004).

[35] C. L. Vicente, H. C. Choi, J. S. Xia, W. P. Halperin, N. Mulders, and Y. Lee, Phys. Rev. B **72**, 094519 (2005).

[36] H. Choi, *Study on Disordered Liquid ^{3}He in High Pororsity Silica Aerogel* (PhD thesis, University of Florida, 2007).

[37] B. I. Barker, Y. Lee, L. Polukhina, D. D. Osheroff, L. W. Hrubesh, and J. F. Poco, Phys. Rev. Lett. **85**, 2148 (2000).

[38] Y. H. Tang, I. Hahn, H. M. Bozler, and C. M. Gould, Phys. Rev. Lett. **67**, 1775 (1991).

[39] I. Hahn, *Thermodynamic Study of the A-B Phase Transition in Superfluid ^{3}He: Phase Diagram and Consequences* (PhD thesis, University of Southern California, 1993).

[40] S. B. Kim, J. Ma, and M. H. W. Chan, Phys. Rev. Lett. **71**, 2268 (1993).

[41] Y. Imry and S. Ma, Phys. Rev. Lett. **35**, 1399 (1975).

[42] G. E. Volovik, JETP Lett. **63**, 301 (1996).

[43] G. E. Volovik, J. Low Temp. Phys. **150**, 453 (2008).

[44] I. Fomin, Sov. Phys. JETP Lett. **77**, 240 (2003).

[45] K. Aoyama and R. Ikeda, Phys. Rev. B **73**, 060504(R) (2006).

[46] R. C. Richardson and E. N. Smith, *Experimental Techniques in Condensed Matter Physics at Low Temperatures* (Addison-Wesley, 1998).

[47] W. P. Kirk and M. Twerdochlib, Rev. Sci. Instrum. **49**, 765 (1978).

[48] F. Pobell, *Matter and Methods at Low Temperatures* (Springer, 2006).

[49] K. A. Muething, D. O. Edwards, J. D. Feder, W. J. Gully, and H. N. Scholz, Rev. Sci. Instrum. **53**, 485 (1982).

[50] D. D. Osheroff and R. C. Richardson, Phys. Rev. Lett. **54**, 1178 (1985).

[51] G. C. Straty and E. D. Adams, Rev. Sci. Instrum **40**, 1393 (1969).

[52] E. D. Adams, Rev. Sci. Instrum **64**, 601 (1993).

[53] D. S. Greywall, Phys. Rev. B **33**, 7520 (1986).

[54] W. Ni, J. S. Xia, E. D. Adams, P. S. Haskins, and J. E. Mckisson, J. Low Temp. Phys. **99**, 167 (1995).

[55] J. H. Colwell, W. E. Fogle, and J. R. J. Soulen, *Temperature, Its Measurement and Control in Science and Industry*, vol. 6 (Amer. Institute of Physics, New York, 1992).

[56] J. Xu, O. Avenel, J. S. Xia, M.-F. Xu, T. Lang, P. L. Moyland, , W. Ni, E. D. Adams, G. G. Ihas, et al., J. Low Temp. Phys. **89**, 719 (1992).

[57] P. Bhupathi, J. Hwang, R. M. Martin, J. Blankstein, L. Jaworski, N. Mulders, D. B. Tanner, and Y. Lee, submitted to PRL (2009).

[58] J. Gross, G. Reichenauer, and J. Fricke, J. Phys. D: Appl. Phys. **21**, 1447 (1988).

[59] M. Born and E. Wolf, *Principles of Optics* (Cambridge, United Kingdom, 1970).

[60] S. T. Wu, U. Efron, and L. D. Hess, Appl. Phys. Lett. **44**, 1033 (1984).

[61] M. J. Escuti, D. R. Cairns, and G. P. Crawford, J. Appl. Phys. **95**, 2386 (2004).

[62] J. Gross, J. Fricke, R. W. Pekala, and L. W. Hrubesh, Phys. Rev. B **45**, 12774 (1992).

[63] G. W. Scherer, D. M. Smith, X. Qiu, and J. M. Anderson, J. Non-Cryst. Solids **186**, 316 (1995).

[64] D. M. Smith, G. W. Scherer, and J. M. Anderson, J. Non-Cryst. Solids **188**, 191 (1995).

[65] T. Herman, J. Day, and J. Beamish, Phys. Rev. B **73**, 094127 (2006).

[66] A. J. Hunt, J. Non-Crys. Solids **225**, 303 (1998).

[67] E. Aschenauer, Nucl. Instrum. Meth. Phys. Res. A **440**, 338 (2000).

[68] A. V. Rao, G. M. Pajonk, D. Haranath, and P. B. Wagh, J. Mat. Syn. and Proc. **6**, 37 (1998).

[69] W. Sellmeier, Annalen der Physik und Chemie **143**, 271 (1871).

[70] I. H. Malitson, J. Opt. Soc. Am. **55**, 1205 (1965).

[71] L. E. Sutton and O. N. Stavroudis, J. Opt. Soc. Am. **51**, 901 (1961).

[72] E. Simanek, Phys. Rev. Lett. **38**, 1161 (1977).

[73] G. L. Carr, S. Pekowitz, and D. B. Tanner, *Infrared and Millimeter Waves* (Academic Press, Inc., 1985).

[74] J. A. Stratton, *Electromagnetic Theory* (McGraw-Hill Book Company, Inc., 1941).

[75] J. A. Osborn, Phys. Rev. Lett. **38**, 1161 (1977).

[76] N. Kunzner, J. Diener, E. Gross, D. Kovalev, V. Y. Timoshenko, and M. Fujii, Phys. Rev. B. **71**, 195304 (2005).

[77] L. A. Golovan, P. K. Kashkarov, and V. Y. Timoshenko, Crystallography Reports **52**, 672 (2007).

[78] V. V. Dmitriev, V. V. Zavjalov, D. E. Zmeev, I. V. Kosarev, and N. Mulders, JETP Lett. **76**, 312 (2002).

[79] V. V. Dmitriev, I. V. Kosarev, N. Mulders, V. V. Zavjalov, and D. E. Zmeev, Physica B **320**, 329 (2003).

[80] E. Nazaretski, N. Mulders, and J. M. Parpia, JETP Lett. **79**, 383 (2004).

[81] J. P. Davis, H. Choi, J. Pollanen, and W. P. Halperin, AIP Conf. Proc. **850**, 239 (2006).

[82] J. P. Davis, J. Pollanen, B. Reddy, K. R. Shirer, H. Choi, and W. P. Halperin, Phy. Rev. B **77**, 140502(R) (2008).

[83] J. P. Davis, *Transverse Sound Spectroscopy of Excited Cooper Pair States in Superfluid ^3He* (PhD thesis, Northwestern University, 2008).

[84] T. Kunimatsu, T. Sato, K. Izumina, A. Matsubara, Y. Sasaki, M. Kubota, O. Ishikawa, T. Mizusaki, and Y. M. Bunkov, JETP Lett. **86**, 216 (2007).

[85] V. V. Dmitriev, D. A. Krasnikhin, N.Mulders, V. V. Zavjalov, and D. E. Zmeev, Pis'ma v ZhETF (JETP Lett.) **86**, 681 (2007).

[86] T. Sato, T. Kunimatsu, K. Izumina, A. Matsubara, M. Kubota, T. Mizusaki, and Y. M. Bunkov, Phys. Rev. Lett. **101**, 055301 (2008).

[87] J. Elbs, Y. M. Bunkov, E. Collin, H. Godfrin, and G. E. Volovik, Phys. Rev. Lett. **100**, 215304 (2008).

[88] E. Dagotto, T. Hatta, and M. Moreo, Phys. Rep. **344**, 1 (2001).

[89] L. Zhang, C. Israel, A. Biswas, R. L. Greene, and A. Lozanne, Science **298**, 805 (2002).

[90] S. Jin, T. H. Tiefel, M. McCormack, R. A. Fastnacht, R. Ramesh, and L. H. Chen, Science **264**, 413 (1994).

[91] A. Biswas, M. Rajeswari, R. C. Srivastava, Y. H. Li, T. Venkatesan, R. L. Greene, and A. J. Millis, Phys. Rev. B **61**, 9665 (2000).

[92] M. Uehara, S. Mori, C. H. Chen, and S. W. Cheong, Nature **399**, 560 (1999).

[93] T. Dhakal, J. Tosado, and A. Biswas, Phys. Rev. B **75**, 092404 (2007).

[94] S. H. Yun, *Effect of Disorder in Cuprates and Manganites* (PhD thesis, University of Florida, 2008).

[95] O. V. Lounasmaa, *Experimental Principles and Methods Below 1K* (Academic Press, 1974).

BIOGRAPHICAL SKETCH

Pradeep Bhupathi was born in Cuddapah district of Andhra Pradesh in South India. He did his schooling in Hyderabad and Calcutta. His college education was in Pondicherry University where he graduated with a Master of Science in Physics in May 2001. He came to the University of Florida in June 2002 and joined the low temperature physics group of Prof. Yoon Lee and received his PhD in the spring of 2009.